University of Alberta

Quantitative Characterization of Microstructure in High Strength
Microalloyed Steels

by

Xiujun Li

A thesis submitted to the Faculty of Graduate Studies and Research
in partial fulfillment of the requirements for the degree of

Master of Science in Materials Engineering

Department of Chemical and Materials Engineering

©Xiujun Li
Fall 2009
Edmonton, Alberta

Examining Committee

Dr. Hani Henein, Department of Chemical and Materials Engineering

Dr. Douglas Ivey, Department of Chemical and Materials Engineering

Dr. Weixing Chen, Department of Chemical and Materials Engineering

Dr. Zihui Xia, Department of Mechanical Engineering

ABSTRACT

X-ray diffraction (XRD) profile fitting (Rietveld method) was used in this study to characterize the microstructure for seven microalloyed steels, which were produced through thermomechanical controlled processing (TMCP). Microstructure characterization was conducted through the strip thickness. The microstructural variables studied include subgrain size, dislocation density, texture index and weight percent of retained austenite. The subgrain size was also analyzed by electron backscatter diffraction (EBSD) and transmission electron microscopy (TEM). The effects of processing parameters, including coiling temperature, cooling rate and alloying elements, on the microstructure were also investigated.

It was found that decreasing the coiling temperature resulted in a finer subgrain size and higher dislocation densities. The texture index was observed to increase with decreasing coiling temperature. The subgrain size decreased and dislocation density increased as the amount of alloying elements (Ni, Mo and Mn) were increased. The amount of retained austenite increased at the strip center with increasing coiling temperature and increasing C and Ni content.

ACKNOWLEDGEMENTS

TABLE OF CONTENTS

LIST OF TABLES

LIST OF FIGURES

LIST OF SYNMBOLS, NOMENCLATURE AND ABBREVIATIONS

α	Ferrite phase
γ	Austenite phase
ε	Microstrain
η	Mixing factor
ρ_{disl}	Dislocation density, cm/cm^3
ρ_D	Dislocation density deduced from the domain size, cm/cm^3
ρ_S	Dislocation density deduced from the microstrain, cm/cm^3
σ_i	The friction stress of iron, MPa
ω	FWHM/2
Φ	Reflection profile function
A	Absorption factor
AF	Acicular ferrite
Al	Aluminum
Ar_3	Austenite-ferrite transformation temperature, ºC
b	Burgers vector, for bcc crystal structure, $|1/2[111]|$
bcc	Body-centered cubic
B	Boron
B_j	Isotropic thermal parameter
BF	Bright field
B-F	Bainitic ferrite
C_i	Concentration of solute i

C_l^{mn}	Spherical harmonics parameter
CCT	Continuous cooling transformation
Co	Cobalt
Cr	Chromium
CR	Normalized cooling rate
CT	Normalized coiling temperature
Cu	Copper
CVN	Charpy V-notch
°C/s	Degree per second
d	Grain diameter
D_s	Domain size, nm
DF	Dark field
EL	Elongation
EBSD	Electron backscatter diffraction
F_K	Structure factor for the K_{th} Bragg reflection
FRT	Normalized finish rolling temperature
FWHM	Full width at half maximum
G	Gaussian function
GoF	Goodness of fit
GSH	General spherical harmonics
H	Caglioti formula
I_0	The peak intensity

ICSD	Inorganic Crystal Structure Database
J	Texture index
k_i	Strengthening coefficient for solute strengthening of solute i
ksi	Thousands of pounds per square inch
k_y	Strengthening coefficient for grain size
κ	Miller indices, h k l, for a Bragg reflection
K	Constant; for bcc crystal structure material, ~14.4
lpA	Lattice parameter, nm
L	Lorentzian function
L_K	Function containing the Lorentz, polarization and multiplicity factors
LaB_6	Lanthanum hexaboride
m	Shape parameter
mm	Millimeter
M	The number to the data point
M_s	Temperature at which martensitic transformation starts
M-A	Martensite-austenite
Mn	Manganese
Mo	Molybdenum
MPa	Million Pascal
N_j	Site-occupancy multiplier for the j_{th} atom in the unit cell
Nb	Niobium
ND	Normal direction

Ni	Nickel
OM	Optical microscope(y)
Occ	Extent of occupancy
P	Number of the parameters
ppm	Part per million
P	Pearson VII function
P_K	Preferred orientation functions
PF	Polygonal ferrite
PV	Pseudo-Voigt function
R_p	R-pattern
R_{wp}	R-weighted pattern
R_{exp}	R-expected
s	Scale factor
sd	Sample displacement
SAD	Selected area diffraction
SEM	Scanning electron microscope(y)
SQRT	Square root
T_s	Reheating temperature
T_{nr}	Non-recrystallization temperature
TEL	Total elongation
TEM	Transmission electron microscope(y)
T_i	Titanium

TMCP	Thermomechanical controlled processing
UTS	Ultimate tensile strength
(U, V, W)	Caglioti function refinable parameters
v_f	Volume fraction of a given precipitate size
V	Vanadium
V_c	Cooling rate
w	Weighting factor
wt%	Mass percentage
WDS	Wavelength dispersive spectroscopy
x	Size of precipitates in microns
(x_j, y_j, z_j)	Position coordinates
X	Pipeline grade
XRD	X-ray diffraction
y_{bi}	Background intensity at ith step
Y_{iobs}	Observed XRD peak intensity at ith step
Y_{ical}	Calculated XRD peak intensity at ith step
YS	Yield strength, MPa

1. INTRODUCTION

1.1 Thesis objective and methodology

With increased use of microalloyed steels in pipe and structural construction, it is essential to understand and develop processing technology, i.e., TMCP, to meet industry requirements. Good mechanical properties, such as high strength and toughness, are needed. Research on the effects of TMCP and composition on the microstructure and corresponding mechanical properties are useful for optimizing processing parameters and steel chemistry. The objectives of this study are to characterize the variation of the microstructure as a function of relative position through the thickness for microalloyed pipeline steels.

XRD (Rietveld method) was used to characterize the microstructures for various microalloyed steels. The Rietveld method is a technique to obtain microstructural features, such as domain size, microstrain, texture index and different phase fraction, by multi-parameter curve fitting. This work is the first attempt at applying the Rietveld method to characterize the microstructure of microalloyed steels, although it has been widely applied to analyze the microstructure of many other metals and alloys. Examples include grain size and texture studies of copper,[1] rolled zirconium alloys[2] and titanium alloys.[3] XRD (Rietveld method) is employed in this study to characterize the subgrain size, average microstrain within the subgrains, texture of microalloyed steels and retained austenite phase fraction. Dislocation density can also be calculated using the values of microstrain and subgrain size.[4]

Other characterization techniques were used to ascertain the microstructural features of steels and compare them to the results from the Rietveld method applied to XRD analysis. Optical microscopy (OM) and scanning electron microscopy (SEM) were used for overall microstructural characterization and substructure and dislocation distribution were examined by TEM and EBSD.

1.2 Outline of the thesis

The thesis is divided into seven chapters. A literature survey is given in Chapter 2. It covers the development of microalloyed steels, the effects of different parameters during TMCP on the microstructural features, the effects of alloying elements on the microstructure and a comprehensive introduction to the Rietveld method. In Chapter 3, experimental details for OM, XRD, SEM, TEM, EBSD and wavelength dispersive X-ray spectroscopy (WDS) are presented. The results of the experimental work outlined in Chapter 3 are presented in Chapter 4. In Chapter 5, a discussion of the effect of processing parameters and chemistry on the microstructure for the seven steels studied is presented. The last part of the discussion is the relationship between the microstructural features and mechanical properties. Conclusions for the work are presented in Chapter 6 and recommendations for future work are made in Chapter 7.

2. LITERATURE REVIEW

The literature review begins with an introduction and the development of microalloyed steels, a review of different processing techniques including a detailed introduction to TMCP, a study of mechanical properties and microstructure evolution during TMCP, i.e., the effects of processing parameters on the microstructural features, and the effect of chemistry on the microstructure. The last part of this chapter is a review of the Rietveld method followed by its application.

2.1 Introduction and development of microalloyed steels

Microalloyed steels get their name from the simple fact that they only contain small amounts of alloying elements. They generally contain about 1.65 wt% manganese (Mn). Note, wt% is used everywhere in this thesis for compositions. They also contain small amounts of aluminum (Al), copper (Cu), nickel (Ni), chromium (Cr), molybdenum (Mo), niobium (Nb), titanium (Ti), vanadium (V) and/or boron (B). The combination of processing and composition greatly enhances the strength of these steels. Microalloying strengthening effects can be achieved by precipitation hardening with very fine precipitate particles and/or by grain refinement.[5] Compared with conventional carbon steels, microalloyed steels have lower carbon contents in order to achieve adequate formability and weldability. In general, microalloyed steels combine many beneficial mechanical properties.

Recently, microalloyed steels have been widely applied in automobiles, bridges, pipelines for oil and gas transportation and other structural components, because of their good combination of mechanical properties. A key factor for any industrial application is material cost. Reduced cost can be achieved by reducing consumption of steel in pipelines and construction, which is realized by increasing the strength of the steel. Cost is not the only factor driving microalloyed steel development; improved energy and resource efficiency and requirements for

higher quality steel for innovative applications all drive the development of microalloyed steels with high strength.[6]

2.2 Processing of microalloyed steels

2.2.1 TMCP

In this section, TMCP is illustrated in detail in terms of several stages. A schematic of TMCP is illustrated in Figure 2-1 with the cooling process superimposed on a continuous cooling transformation (CCT) diagram. T_{nr}, A_{r3}, and M_s represent the no-recrystallization temperature, the austenite-ferrite transformation temperature and the temperature at which the martensitic transformation starts, respectively. TMCP can be divided into five stages: homogenization, rough rolling, finish rolling, accelerated cooling and coiling.[7]
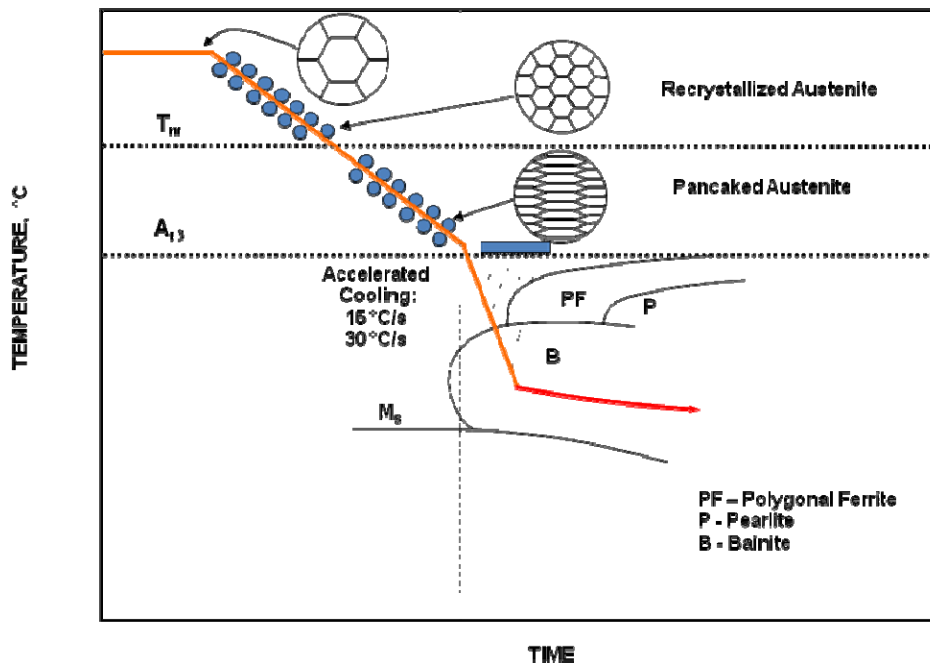
Figure 2-1 - Schematic illustration of TMCP.[7]

A detailed analysis of each stage in TMCP is described in the following paragraphs.[5,6]

I. (Homogenization) The steel is heated to a high temperature of about 1200°C (at least 1050°C but no higher than 1350°C) and soaked at this temperature for a period of time to dissolve the precipitation elements and to obtain a uniform austenite phase.

The steel may have a different chemistry, either the carbon content or microalloying elements, or contain various phases, i.e., ferrite, pearlite, bainitic ferrite and/or martensite. During reheating process, the temperature of the steel is increased to a sufficient value within the austenite range to minimize the heterogeneity in the microstructure. In addition, dissolving the precipitates is necessary, otherwise the undissolved precipitates could be coarsened during the following processing and lose their precipitation strengthening effects. A sufficiently high temperature is needed during homogenization and the reheating temperature is highly dependent on the chemistry, especially the alloying additions and the equilibrium solution temperature for the precipitates.

II. (Rough rolling) The aim is to break down the austenite phase through several recrystallization cycles.

Rough rolling transforms the continuously cast slabs to semi-finished products. Rough rolling begins with coarse grained austenite and complete dissolution of the microalloying elements. Rough rolling begins at a temperature higher than the no-recrystallization temperature of austenite but lower than about 1200°C. Austenite grain refinement occurs through several recrystallization cycles. There are two different types of recrystallization, static recrystallization and dynamic recrystallization.[5]

i. Strain in the form of dislocations, grain and subgrain boundaries. More strain, which results in more stored energy, makes more energy available as a driving force and, consequently, leads to a higher static recrystallization rate.

ii. Temperature. Both nucleation and grain growth are thermally activated processes, which are highly influenced by temperature. Higher temperatures are helpful for both nucleation and grain growth and, therefore, increase the static recrystallization rate.

iii. Temperature compensated strain rate. Recrystallization occurs by deforming the steel, so as to introduce more dislocations and other defects, which create more ferrite nucleation sites.

iv. Prior austenite grain size. Nucleation preferably takes place along the grain boundaries of the prior austenite grains. Refinement of prior austenite grains increases the grain boundary area thus increasing the number of possible nucleation sites and the recrystallization rate.

Rough rolling results in fine recrystalized austenite grains, with a small amount of strain within the grains and is followed by a finish rolling process. At the end of rough rolling stage, the steel temperature is controlled below the no-recrystallization temperature.

III. (Finish rolling) The austenite is further deformed below the no-recrystallization temperature of austenite, but higher than the austenite to ferrite transformation temperature. Microstructure refinement and dislocation generation can be achieved by hot rolling passes. During finish rolling, fine spherical austenite grains are changed to pancaked austenite which are typically grains elongated along the rolling direction. The finish rolling temperature (FRT) is normally controlled to be slightly higher than the austenite to ferrite transformation temperature to avoid coarsening of the ferrite phase. If the FRT is lower than the austenite to ferrite transformation temperature, there would be both deformed austenite and ferrite phases. Recovery and recrystallization within the ferrite grains might occur to further refine the ferrite phase if there is sufficient deformation at lower temperature, especially lower than 750°C.

IV. (Accelerated cooling) Accelerated cooling of the strip occurs at cooling rates between 10°C/s and 30°C/s from the FRT down to a coiling temperature (CT) or interrupted cooling temperature (ICT). By cooling the steel to a selected

target temperature, the desired microstructural transformation can be achieved by adjusting both the CR and CT. In addition, grain refinement can be accomplished by accelerated cooling. The detailed effects of cooling rate (CR) on microstructural evolution, including grain/subgrain refinement, dislocation density and phase transformation, are illustrated in Section 2.3.

During accelerated cooling, when the strip is rapidly cooled by a water spray on the run-out table, the cooling rates at different locations through the thickness vary to some extent. With different cooling rates at different locations, the microstructure including ultimate phase constituents and grain morphology may vary as well.

V. (Coiling) The strip is coiled to increase the dislocation density for strain-induced precipitation and to affect the matrix microstructure. Introducing dislocations can increase the kinetics of precipitation and, thus, the volume fraction of the desired particle size can be achieved. Dislocations also enhance the strength of the steel. As mentioned above, CT is also a key parameter affecting microstructure evolution, including grain/subgrain refinement and dislocation density; details are given in Section, 2.3.

In summary, TMCP, which combines hot deformation and controlled cooling, directly controls microstructure development during production by controlling the different processing parameters during the various stages.

2.2.2 Comparison of TMCP with traditional technology

Compared with traditional technology, TMCP has become the most cost effective process to control microstructure evolution and properties. Figure 2-2 is a schematic showing a comparison of traditional technology and TMCP.[8] As described above, the steps in TMCP include homogenization, rough rolling, finish rolling, accelerated cooling and coiling. Compared with traditional technology, TMCP applies lower reheating temperatures and finish rolling temperatures, and an accelerated cooling process is added after finish rolling, replacing furnace cooling.
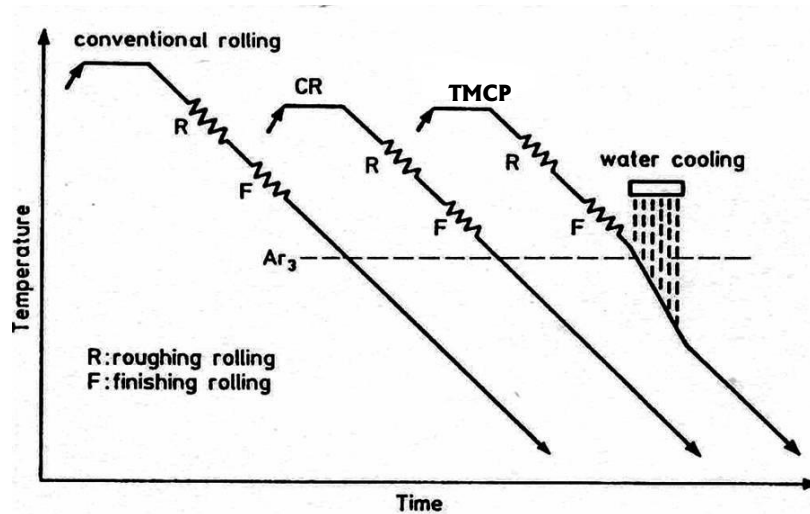
Figure 2-2 – Comparison of TMCP with other techniques.[8]

Figure 2-3 shows the microstructure evolution during the process of traditional technology and TMCP.[8] As TMCP lowers the FRT, which is below austenite recrystallization temperature, a pancaked austenite microstructure is obtained before the phase transformation, which contains multiple deformation bands. Compared with conventional rolling, an accelerated cooling process is added after finish rolling, as shown in Figure 2-3. The number of potential nucleation sites for the ferrite phase increases due to severe deformation after recrystallization and accelerated cooling. Therefore, a finer ferrite phase is achieved in comparison with the ferrite structure obtained by the conventional process.
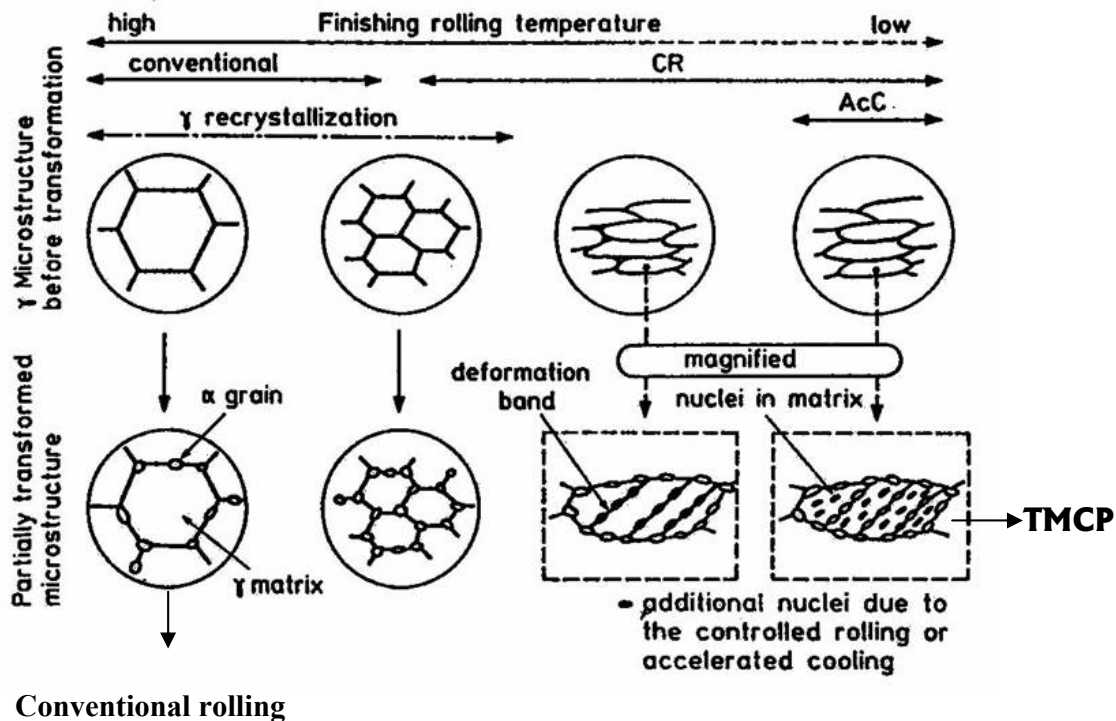
Figure 2-3 – Comparison of metallurgical aspects for conventional rolling and TMCP.[8]

2.3 Mechanical properties and microstructure evolution

The effects of TMCP processing parameters on mechanical properties are illustrated in this section and are followed by a literature review based on microstructural feature variation, such as grain and subgrain size, dislocation density, texture and retained austenite phase fraction, caused by changing processing parameters.

2.3.1 Mechanical properties

Investigations on improving the TMCP process usually entail correlating mechanical property changes with variations in processing parameters. Difference in processing parameters for any of the five stages may result in variations in mechanical properties. A number of experiments have been conducted on the effects of TMCP parameters during each specific stage, such as reheating temperature, fraction of deformation during both rough rolling and finish rolling,

FRT, CR, CT, etc., on the mechanical properties, particularly yield strength and toughness. [9,11,12,14]

The relationship between TMCP parameters and mechanical properties for microalloyed steels has been extensively studied by M.C. Zhao et al.. [8] The author conducted this investigation using a series of microalloyed steel, which have the same chemistry and different processing parameters. Two regression equations, which quantitatively describe the relationship between processing parameters and mechanical properties, were developed based on the study of steels with various TMCP parameters. [9]

$$YS = 0.508T_s - 0.231T_f - 0.334T_c + 1.905V_C + 323.6 \qquad (2\text{-}1)$$

$$EL = -0.002T_s - 0.064T_f - 0.086T_c + 0.325V_c + 121.8 \qquad (2\text{-}2)$$

where YS (MPa), EL (%), T_s (°C), T_f (°C), T_c (°C) and V_c (°C/s) represent the yield strength, elongation, reheat temperature, FRT, CT and CR, respectively. The reheat temperature is in the range of 1050-1112°C, the FRT is 850-907°C, the CT is 487-529°C and the CR is 10-30°C/s.

As shown in equation 2-1, the yield strength increases with increasing reheating temperature and CR; however, it decreases with increasing FRT and CT. A lower reheating temperature, FRT, CT and higher CR all increase elongation, as shown in equation 2-2. Zhao et al. suggest that these relationships could be applied to microalloyed steels.

Another investigation, done by S.J. Zhao et al., verified the effect of reheating temperature shown as equation 2-1 and 2-2. An increase in reheating temperature brought elevated strength at the expense of elongation. [10] Reheat temperature has a strong effect on the formation of carbonitrides. Compared with Ti and V, only the Nb carbonitride formation temperature is close to the reheat temperature. Increasing the reheat temperature allows more Nb to go into the solution. Some of the Nb can precipitate out later and, consequently, increase the yield strength.

With increasing reheating temperature, austenite grain growth occurs and ferrite grains will be coarsened after transformation, which results in a decrease in elongation. As shown by equations 2-1 and 2-2, the reheating temperature does not affect elongation as much as the yield strength. A study, done by Wang et al., also showed the same relationship, i.e., the yield strength decreases with increasing reheating temperature with small changes in elongation.[11]

According to a study done by Li et al., the strength increases with decreasing FRT.[12] A number of studies have been done on the effect of CT on mechanical properties and, in general, it was found that both strength and toughness are improved by decreasing CT (also shown by equations 2-1 and 2-2).[13] A number of studies have been done to verify that increasing CR enhances both yield strength and toughness; also shown by equations 2-1 and 2-2. [14,15]

Figure 2-4 shows the effects of reheating temperature, FRT and CR on yield strength, as well as on the ferrite grain size.[16] The results were obtained by conducting experiments on Nb containing steels. Increasing the reheating temperature and CR and decreasing the FRT result in higher yield strengths and smaller grain sizes.
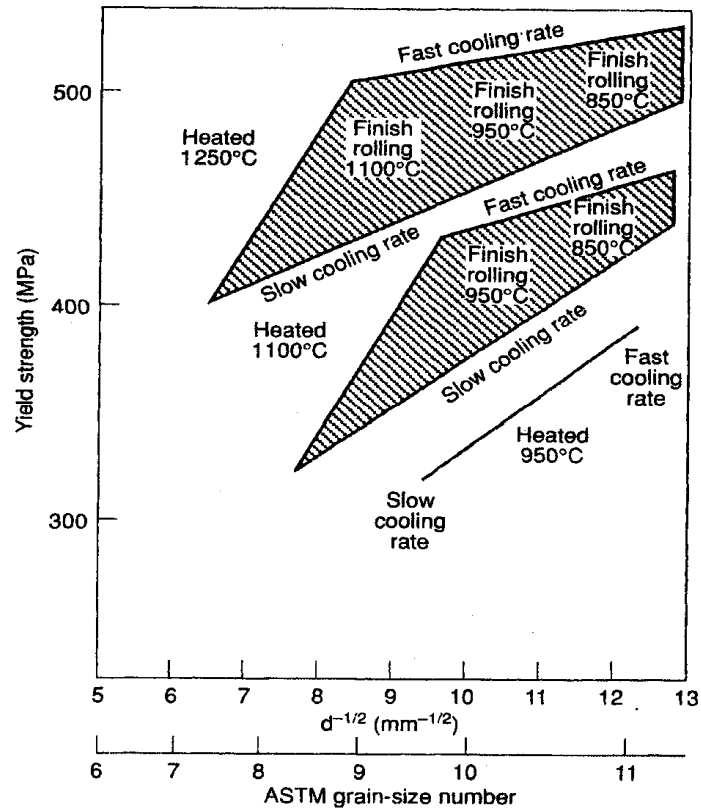
Figure 2-4 – The effects of processing parameters during TMCP on YS and grain size.[16]

2.3.2 Microstructural features

Adjusting different TMCP processing parameters, e.g., reheating temperature, FRT, CT and CR, can change the mechanical properties, i.e., yield strength and elongation, of steel. These changes in mechanical properties are related to differences in microstructure. This section will correlate the effects of TMCP processing parameters on the microstructure.

In general, the final microstructure can be controlled by adjusting the processing parameters, including reheating temperature and time, extent of deformation for each stage (rough rolling or finish rolling), time taken for each rolling pass, FRT, CT, accelerated CR etc,. Differences in any processing parameter may result in a variation in microstructure and ultimately properties. A number of studies have been done about the influence of each processing parameter on the final microstructure. In this section, microstructural feature

changes, including grain and/or subgrain size, dislocation density and texture, with a variation in TMCP parameters are included. Precipitation is another significant feature for high strength microalloyed steels; however, the evolution of precipitates, such as type, size and volume fraction, will not be included in this study.

2.3.2.1 Grain and/or subgrain size

Grain refinement is an essential technique to improve both strength and toughness. Considerable attention has been given to factors that affect ferrite grain size. There are many TMCP parameters which influence ferrite grain size in the microalloyed steels: [5]

- Steel chemical composition;

- Austenite grain size prior to transformation to ferrite;

- Deformation below the recrystallization temperature;

- Degree of recrystallization of austenite during the rough rolling stage;

- Transformation start temperature;

- FRT;

- CR and CT.

The effects from reheating temperature, FRT, CR and CT on grain and/or subgrain size are discussed in this section.

Prior austenite grain size is directly related to the reheating temperature. Coarsened austenite grains transform to ferrite phase with relatively large grain sizes. Studies have been done on the relationship between reheating temperature and ferrite grain size and it was found that the ferrite grain size decreases with decreasing reheating temperature. The reason may be that decreasing reheating temperature can result in refinement of the prior austenite grain size. Consequently, a finer ferrite grain size would be obtained with a lower reheating

temperature, since austenite grain boundaries are nucleation sites for ferrite phase.[10, 11, 17]

Several studies have been done on the effect of FRT on grain size.[16, 18] It was found that lowering the FRT is helpful for the grain refinement within a range, i.e., between approximate 850 °C to 1000 °C; however, the temperature should be higher than the austenite to ferrite transformation temperature. Figure 2-5 shows the effect of FRT on the linear intercept grain size, where K, L, Z, T, S, M represent different steels.[18] Ferrite grain size coarsens with decreasing FRT if the FRT is higher than approximate 870°C; however, if the FRT is lower than 870°C, the ferrite grain size decreases with decreasing FRT. In other words, if the FRT is lower than the austenite to ferrite transformation temperature, some ferrite is formed during rolling, producing deformed ferrite that has a detrimental effect on toughness. This ferrite phase would grow rapidly and lower the yield strength. The effect of FRT on grain size was also verified by another study done by Ginzburg.[16]
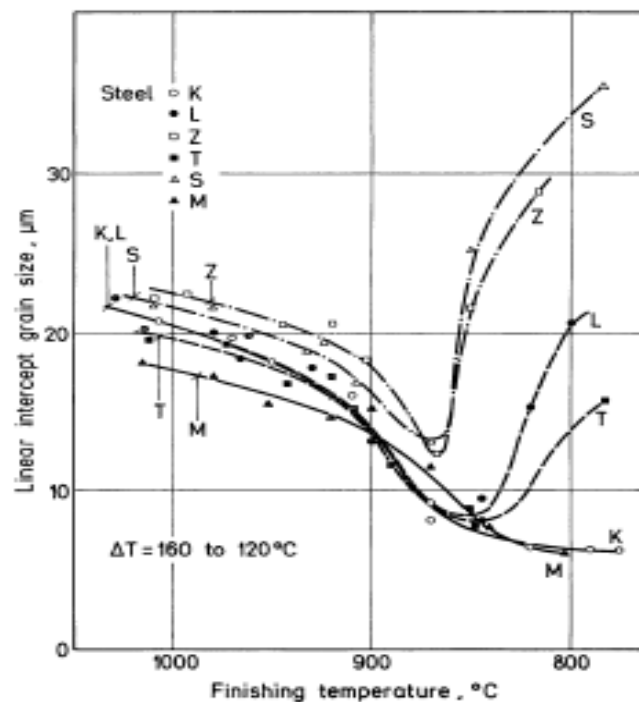
Figure 2-5 – Influence of FRT on grain size of steels. [18]

Studies done on the effect of CR on the microstructure indicated that accelerated cooling can result in a finer structure than furnace cooling or air cooling. [19,20] Accelerated cooling prevents recrystallization of deformed austenite and allows the austenite phase to transform directly after hot rolling, thereby keeping the nucleation sites for ferrite and bainitic ferrite phases, since during finish rolling many dislocations and other defects are introduced. Numerous nucleation sites and rapid cooling combine to form a very fine grain size by increasing the nucleation rate and preventing grain growth. It is also explained that higher cooling rates result in an increase in the extent of undercooling and, consequently, lower the transformation temperature, preventing grain growth. Figure 2-6 shows an example of the effect of CR on ferrite grain size for a steel with Nb and B added as alloying elements.[21] The ferrite sizes are much smaller when the steels are cooled at rates of 30 °C/s and 50 °C/s, compared with those cooled at rates of 1 °C/s and 10 °C/s.
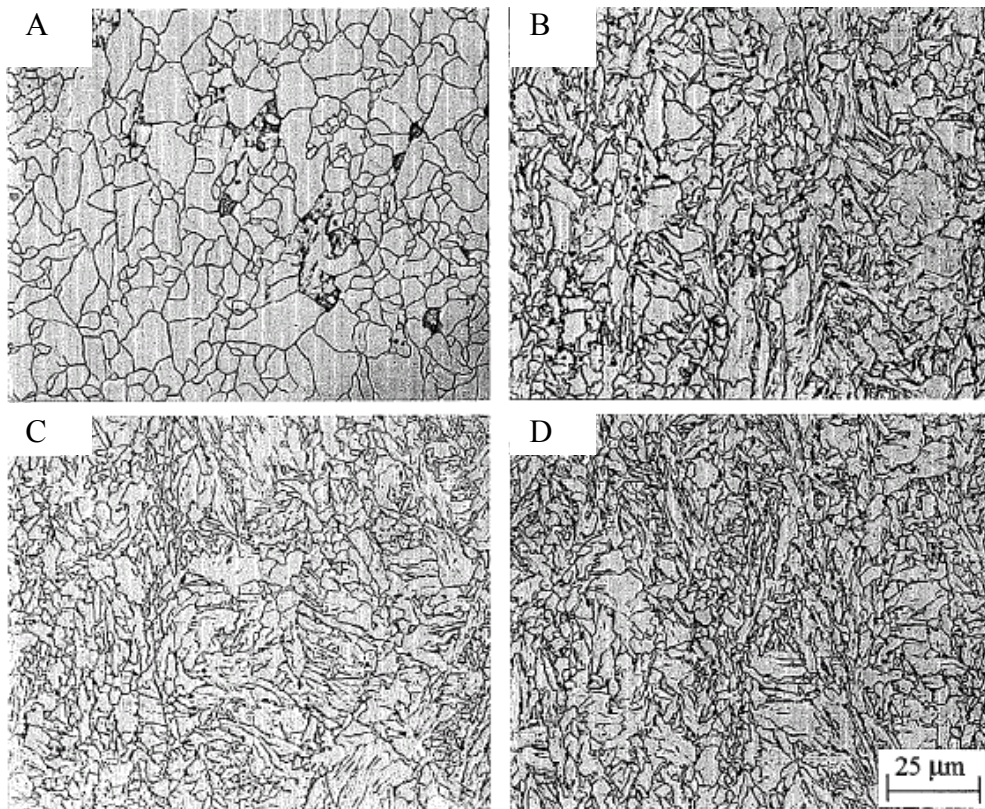
Figure 2-6 - The effect of CR on ferrite grain size. (A), (B), (C) and (D) correspond to CR of 1°C/s, 10°C/s, 30°C/s and 50°C/s.[21]

Figure 2-6 also shows morphology differences for the steels cooled at different rates. More lath-like structures were obtained with higher cooling rates, instead of polygonal ferrite at lower cooling rates. The effect of cooling rate will be discussed in a subsequent section.

CT is the end temperature of the accelerated cooling process. Investigations in adjusting the CT to control the final microstructure have attracted people's attention, since the CT can be cheaply and easily controlled. Experiments in the literature have been done to study the influence of CT on the ferrite grain size of various steels. In a study conducted by Donnay et al., ferrite grain size in low carbon steels increases from 8 µm to around 16 µm with CT increasing from 650°C to 800°C with the same initial CR.[22] Zrnik et al. also observed an increase in ferrite grain size with increasing CT. An average ferrite grain size of 4.57 µm at a CT of 520°C was coarsened to 5.3 µm at a CT of 670°C.[13] The reason for grain growth is believed to be due to the coiling process being performed before the end of the phase transformation. After coiling, the steel stays at a fairly high temperature and then cools to room temperature. Either fresh ferrite grains or transformed ferrite are easily coarsened at such a high temperature.

The important feature of controlled rolling is the formation of substructure. During finish rolling, some of highly deformed austenite structure may transform to ferrite and the resultant ferrite will be subject to rolling as well. In other words, before accelerated cooling, the microstructure consists of a mixture of recrystalized austenite, pancaked austenite and prior transformed ferrite with deformation bands. During cooling, the deformed ferrite may develop subgrains.[5]

Limited studies have been done on the effects of processing on the substructure. Deforming the steels in the austenite-ferrite region is especially crucial for the formation of substructure. Studies in the literature looked at a steel subjected to strong deformation at the 600-650°C range; all the ferrite grains contained substructure, which increased the yield strength.[5,23] As shown in Figure 2-7, the strengthening effect is enhanced when the subgrain size gets smaller for microalloyed steels. The FRT is about 700°C.[24] However, controlling FRT in such low range may easily result in prior transformed ferrite coarsening, as discussed

before, so FRT is normally controlled to be slightly higher than austenite to ferrite transformation temperature.
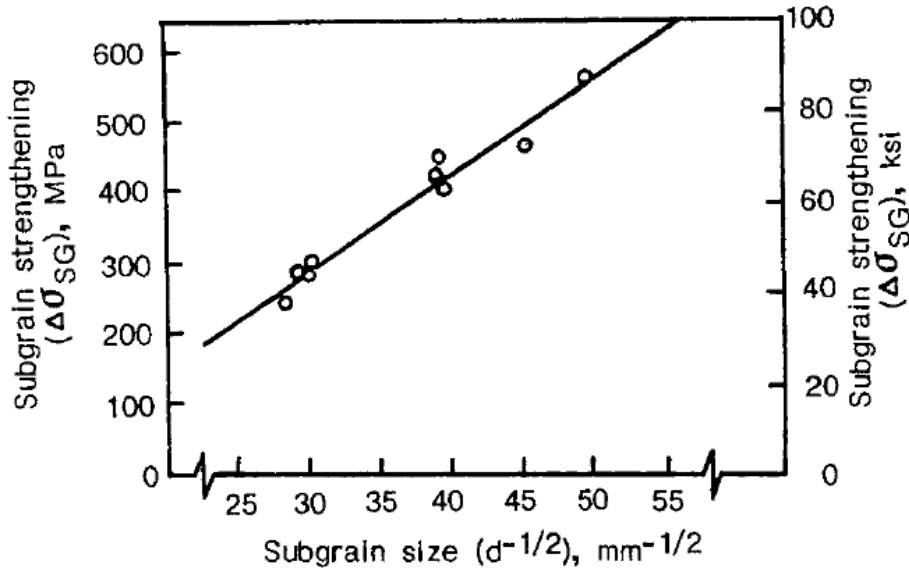
Figure 2-7- The effect of subgrain size on yield strength for microalloyed steels.[24]

The effects of CR and CT on the substructure (size and shape) have not been comprehensively discussed and no specific conclusion has been reached based on the studies in the literature, due to the difficulty in quantitatively characterizing the sub-structure (size and shape).

2.3.2.2 Dislocation density

The dislocation density is a measure of the total length of dislocations present in a given volume of a material. Because a dislocation is a line defect, it is defined as the total length of dislocation per unit volume.

Work from the literature indicates that a decrease in FRT leads to an increase in dislocation density. Dislocation density may increase from 3×10^9 cm/cm^3 to 9×10^9 cm/cm^3 with a FRT reduction from 800°C to 650°C. [25] This may be because the FRT is lower than the transformation temperature and highly elongated ferrite grains with a high dislocation density are formed at low FRT.

Generally increasing the CR is helpful in obtaining a higher dislocation density. The accelerated cooling process starts from FRT and continues to the CT with a certain CR. Different cooling rates result in different phase transformations and also in a variation in microstructural features. Even starting with the same FRT and finish with the same CT, different cooling rates lead to different microstructural features, such as combinations of phases, grain sizes and precipitation features. From the CCT curve shown in Figure 2-8, bainitic ferrite or acicular ferrite can be obtained through faster cooling instead of pearlite which is obtained at lower cooling rates.[26] It is believed that bainitic ferrite has a higher dislocation density compared to polygonal ferrite.[27] Sha et al. confirmed that higher dislocation density result from increased cooling rates.[28]
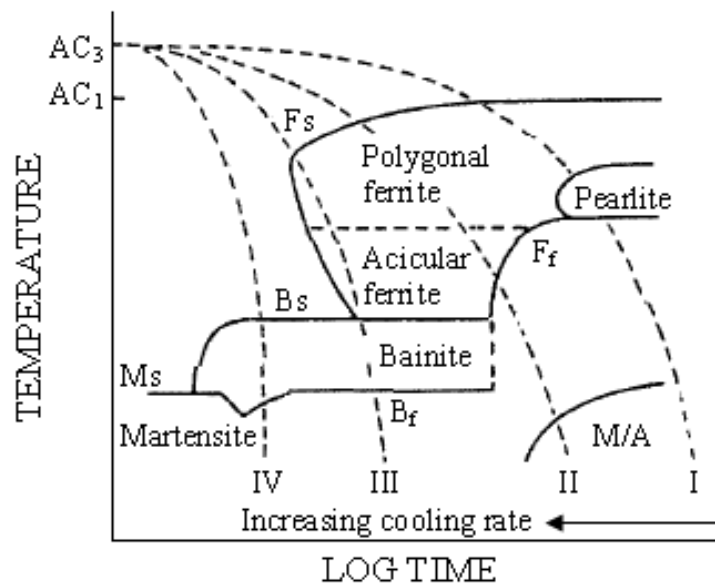
Figure 2-8 - An example of a CCT diagram for a microalloyed steel.[26]

There have been several studies conducted about the effect of CT on dislocation density and it was found that with lower CT the dislocation density was increased.[28, 29] As CT decreases, the accelerated cooling process is extended for the same CR. Decreasing the CT results in lower transformation temperature microstructures with higher dislocation density. Martensite or more bainitic ferrite formation occurs at higher cooling rates. It is known that a bainitic ferrite

microstructure has a higher dislocation density compared to polygonal ferrite. Dislocation density in martensite is even higher than that in bainitic structure. Nastich et al. found that with a lower CT, a high density of dislocations (10^9-10^{10} cm/cm^3) and dislocation pile-ups in the form of low-angle substructure boundaries were observed in the microstructure. A relatively high CT resulted in a decrease in the dislocation density.[29]

2.3.2.3 Texture

Texture refers to the distribution of crystallographic orientation in a sample.[30] If the grains of the material are fully randomly oriented, the material is said to have no texture. However, if there is some preferred orientation for the grains, then the grains may have weak or strong texture. The intensity of the texture depends on the percentage of the grains with preferred orientations. Texture is frequently represented as {hkl} <uvw>, {hkl} represents the planes of the grains that are parallel to the plane of the sheet and their <uvw> direction is parallel to the rolling direction.[31]

Generally there are two different types of texture for microalloyed steels, i.e., transformation texture and deformation texture. During hot rolling, the austenite phase may develop some texture which is inherited by the ferrite phase after transformation, i.e., transformation texture. The transformation texture can be affected by recrystallization and deformation of austenite, which results in different types of texture with different intensity. Rolling of the ferrite phase can also generate some deformation texture in the ferrite, which is generally referred to as deformation texture.[31, 32]

Texture studies are done by electron backscatter diffraction (EBSD), neutron diffraction and XRD with texture goniometry and pole figures obtained. By analyzing the pole figures, texture type and corresponding intensity are found. Work in the literature on texture studies for steels has always been conducted by specifying the types of the texture and then determining its corresponding intensity. Relationships between specific texture and processing parameters are then established. Generally, texture could be achieved by changing processing

parameters, such as increasing deformation during controlled rolling or decreasing the FRT. For the chemistry effect, generally the intensity of texture is increased by adding alloying elements, such as Nb, Ti and V.[31, 32, 33, 34]

Misra et al. conducted a study of texture gradient through thickness for a high strength, hot rolled microalloyed steel. The steel was hot rolled by approximate 95% thickness reduction. XRD pole figures were collected by a scintag diffractometer at different locations through thickness. Different types of texture were observed through thickness. Overall, the most intense texture was observed at the center, which is believed to be due to a variation in temperature across the thickness and changes in strain.[35]

Some investigations in texture inhomogeneity through thickness were conducted for stainless steels by Raabe et al.[36,37, 38,39] The stainless steel sheet was subjected to 95% thickness reduction. The maximum texture was observed at the center thickness location in comparison with the surfaces. It was found that the texture gradients are mainly due to texture inherent from the hot rolling procedure. There are several factors that may result in texture gradients, including friction between the roller and the strip surfaces, and temperature differences through the thickness, which could lead to inhomogeneous strain fields and different texture with various intensities. However, no numerical models have been developed to quantitatively explain the effects of variation of processing parameters through thickness on texture inhomogeneity.

The mechanical properties are closely related to the texture present in the material, which may result in anisotropy in the mechanical behavior.[32, 40] For microalloyed steels, attention is particularly focused on yield strength and toughness. The effects of different textures on the anisotropy of tensile strength have been summarized by Ray.[32] Baczinsky et. al analyzed the influence of texture on the toughness for microalloyed pipeline steels.[41] Positive effects were observed for textures in the vicinity of the normal direction (ND) fiber (<111>/ND) on both strength and toughness.

2.4 The effect of chemistry on microstructure

The desired steel properties are achieved by selection of both optimal TMCP conditions and steel composition, so the influence of alloying elements on microstructure should be considered as well. Alloying elements are added to achieve different effects depending on the property requirements.[42] Common alloying elements in microalloyed steels include Al, B, C, Cr, Cu, Mn, Mo, N, Nb, Ni, Si, Ti and V.

The effects of main alloying elements are briefly discussed below:[5,16,43,44]

- Al is mainly used as a de-oxidant. There is usually some residual Al (0.02-0.05%) content in the steel.

- B is an unique element, which increases the hardenability when added as a small amount. B shifts the CCT diagram to right, promoting the formation of strong phases, i.e., bainitic ferrite and martensite.

- C increases the strength and hardenability, at the expense of ductility and weldability. C affects the mechanical properties by forming carbides. In different types of steel, the C content is controlled in different ranges. Carbon levels should be controlled low for improvement of toughness and weldability.

- Cr increases the hardenability for microalloyed steels. Low Cr contents could promote the formation of low temperature products by stabilizing the austenite phase and inhibiting the austenite to ferrite transformation. Higher Cr contents, e.g., 17 wt% in stainless steel, can improve corrosion resistance as well.

- Cu is added primarily to improve atmospheric corrosion resistance, with concentrations of approximately 0.35%. Cu may also considered provide some precipitation hardening in microalloyed steels.

- Mn generally exists in microalloyed steels at a higher level by controlling the transformation temperature and kinetics as an austenite stabilizer. It is

generally used along with Ni. In addition, Mn promotes the formation of acicular ferrite and bainitic ferrite.

- Mo is an important solid solution strengthener and also plays a significant role in precipitation strengthening. Mo also greatly increases the hardenability by promoting the formation of sufficient bainitic structure to increase the strength as well as maintaining sufficient impact toughness, by shifting the ferrite and pearlite curves of the CCT diagram to the right.

- N is an essential element in microalloyed steels. It improves the mechanical properties in the form of various nitrides. The nitrides can prevent grain growth during rolling and delay recrystallization. The nitrides also increase the strength by precipitation hardening.

- Ni is a ferrite strengthener by forming a substitutional solid solution. Ni also lowers the austenite to ferrite transformation temperature as an austenite stabilizer, inducing ferrite grain refinement. Related to mechanical properties, Ni increases strength and toughness for microalloyed steels.

- Nb is the first microalloying element ever added to steels. Nb is a very strong carbonitride former. Nb carbonitrides may precipitate in austenite, during transformation of austenite to ferrite or in the ferrite after the transformation is complete. The carbonitrides can inhibit grain growth of both austenite and ferrite. Small additions of Nb may dramatically reduce the recrystallization rate of austenite during hot rolling.

- Si is mainly used as a powerful deoxidizer in steelmaking.

- Ti is commonly used in microalloyed steels, because of the stability of TiN at high temperatures. TiN may help control prior austenite grain growth. Ti and Nb carbides are mutually soluble and exist as Ti/Nb carbides.

- V has greater solubility in austenite than Nb and is more likely to stay in solution before the austenite to ferrite transformation. V has great effect

on the microstructure, i.e., V promotes the formation of polygonal ferrite by shifting the ferrite nose to higher temperatures and shorter times. In addition, V suppresses the transformation of austenite to ferrite and pearlite, resulting in retained austenite and/or martensite.

- In general, Al, Cr, Nb, Mo, Si and Ti are ferrite stabilizers while, C, Co, Cu, Mn, Ni and N are austenite stabilizers. Figure 2-9 shows that adding of Mn and Ni lowers the austenite to ferrite transformation temperature, while the other elements result in a transformation temperature increase. A lower austenite to ferrite transformation temperature allows a fine ferrite grain size to be achieved.
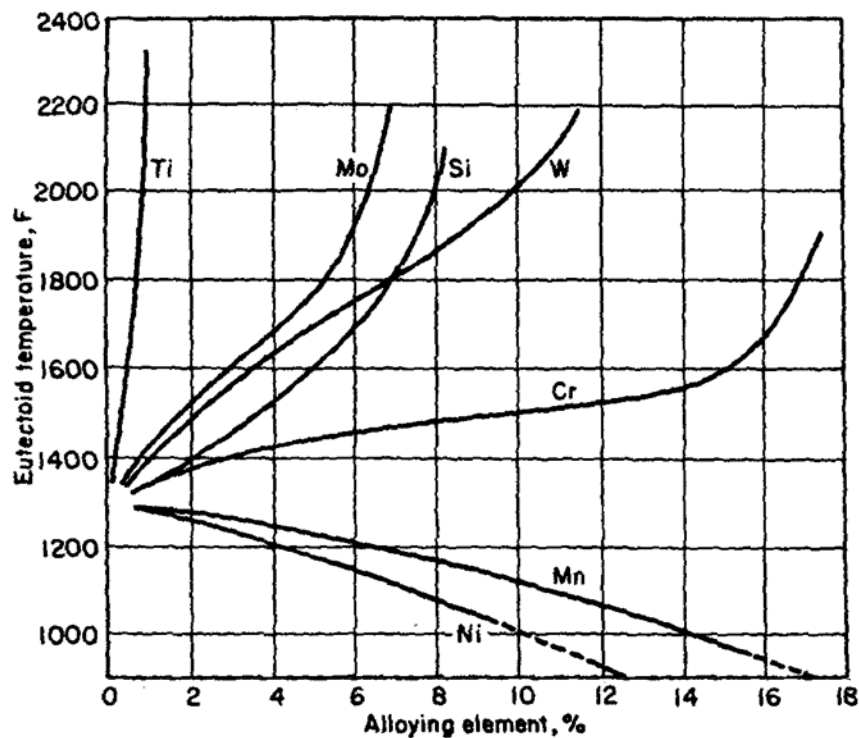
Figure 2-9 - Effect of alloying elements on the austenite to ferrite transformation temperature.[16]

2.5 Rietveld method

2.5.1 Introduction to the Rietveld method

The Rietveld method for profile fitting is a technique widely applied in XRD for structure analysis. It was invented by Hugo Rietveld in 1967. Least-squares refinements are performed until a best fit is achieved between the whole observed diffraction pattern and the calculated pattern and the calculated patter is based on both instrumental parameters and materials microstructure. The minimization is given by the equation below.[45]

$$\text{Least-squares minimization: } S = \sum w_i (Y_{iobs} - Y_{ical})^2 \qquad (2\text{-}3)$$

where Y_{iobs} and Y_{ical} are the intensity observed and the intensity calculated at ith step. w_i is the statistical weight of each observation point, which takes into account the statistical accuracy of the diffraction experiment, and is set to $1/y_i$ in the Topas software.

A number of studies in microstructure characterization of microalloyed steels have been undertaken using various characterization techniques, including OM, SEM, TEM and EBSD. Based on studies in the literature, quantitative XRD (Rietveld method) has not been applied to microalloyed steels. Compared with other techniques, XRD is a powerful non-destructive technique for determining a range of physical and chemical characteristics of materials.[45] It is widely used in all fields of science and technology. By quantifying XRD patterns, materials microstructure parameters, such as the type and quantities of phases, the crystallographic unit cell and crystal structure, crystallographic texture, crystallite size and microstrain can be obtained.[45]

Figure 2-10 presents an example (LaB$_6$ pattern) showing how the microstructure features can be obtained by the Rietveld method. A simulated pattern (red) is calculated based on both instrumental and specimen contributions and compared with the experimental pattern (blue). The difference, i.e., the observed pattern minus the calculated pattern (grey line), is shown as well. The

short vertical bars, shown in lower field, indicate the positions of possible Bragg reflections. By comparison of the experimental pattern and the simulated pattern, the difference is minimized by least-squares minimization until a best fit is achieved and the microstructural features are outputted.
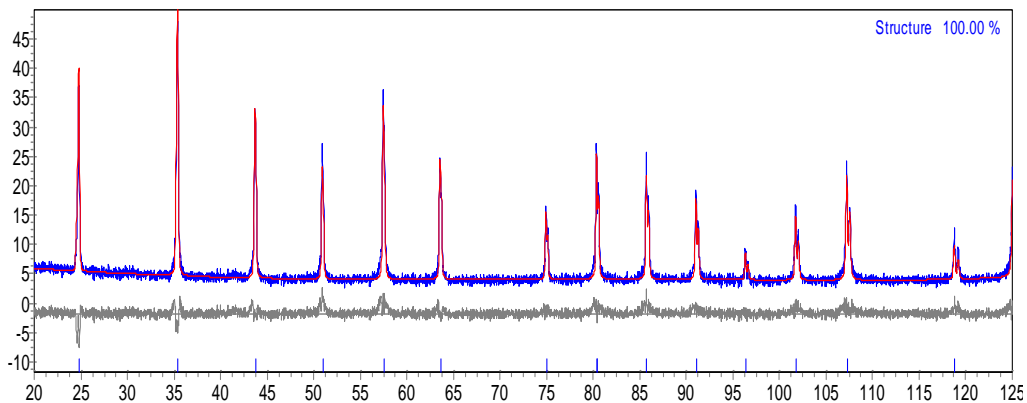
Figure 2-10 – Example of a calculated (red) and experimental (blue) XRD pattern (Rietveld method).

2.5.2 Rietveld method model

The Rietveld refinement model is calculated based on the crystal structure (lattice parameters, atom positions, thermal occupancy parameters and site occupancy parameters), specimen microstructural features (microstrain, domain size and texture) and instrumental contributions. For the crystal structure, there are several databases with known structures, such as the Inorganic Crystal Structure Database (ICSD), Crystallography Open Database, American Mineralogist, etc.[45] Microstructural features may broaden the diffraction peaks, e.g., such as domain size and microstrain, or may systematically redistribute the diffracted intensities, e.g., preferred orientation.

Considering all the factors that contribute to intensity, Y_{cal}, the Rietveld method model is calculated, as shown below. [45]

$$Y_{cal} = s \sum_K L_K \left| F_K \right|^2 \phi \left(2\theta_i - 2\theta_K \right) P_K A + y_{bi} \qquad (2\text{-}4)$$

where s is a scale factor, K represents the Miller indices, h k l, for a Bragg reflection, L_K contains the Lorentz, polarization and multiplicity factors, Φ is a reflection profile function, P_K is a preferred orientation function, A is an absorption factor, F_K is the structure factor for the K_{th} Bragg reflection and y_{bi} is the background intensity at the ith step.

For the background intensity, normally y_{bi} is obtained in several ways: i) linear interpolation between operator selected points in the pattern or ii) a specific background function. The most commonly used background modeling function is a fifth order polynomial.

As shown by the Rietveld method model, the parameters that are refined include not only atom positions and lattice parameters, but also parameters for the background and specimen reflection profile broadening agents, such as microstrain and domain size. Table 2-1 summarizes all the usual parameters that need to be refined.

Table 2-1 – Rietveld refinable parameters[45]

Specimen
x_j, y_j, z_j, B_j, N_j
(x_j, y_j and z_j are position coordinates, B_j is an isotropic thermal parameter and N_j is the site-occupancy multiplier for the j_{th} atom in the unit cell.)
Scale factor
Specimen-profile breadth parameters
Lattice parameters
Overall temperature factor (thermal factor)
Preferred orientation
Domain size and microstrain (through profile parameters)
Instrument
2θ – Zero
Instrumental profile
Background
(Parameters in analytical function, e.g., 5th order polynomial, sum or exponential)
Wavelength
Specimen displacement
Absorption

2.5.3 Reflection of profile function

The reflection function Φ, incorporated in equation 2-4, approximates the effects of both specimen caused broadening (domain size and microstrain) and instrumental broadening. The instrumental contribution function and specimen contribution model are mathematically convoluted and compared with the experimental pattern to obtain the best fit. The microstructural features are outputted.

2.5.3.1 Instrumental broadening contribution

There are various sources of instrumental broadening contributions to X-ray diffraction pattern, as shown in Figure 2-11. It mainly includes wavelength dispersion, flat specimen, specimen transparency, axial divergence, slits and specimen misalignment, and axis offset. [46]
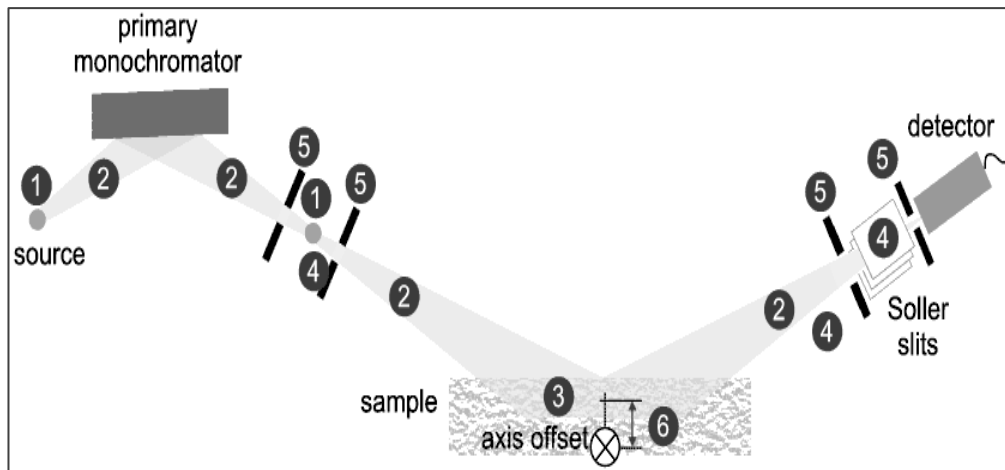
Figure 2-11 – Various factors that result in the instrumental contribution. where 1, 2, 3, 4, 5 and 6 represent wavelength dispersion, a flat specimen, specimen transparency, axial divergence, .[46]

A LaB$_6$ standard, with no broadening effects to XRD pattern, was used as a standard material to quantify instrument broadening. The instrumental broadening representing function has typically been modeled as[45,47]

$$H^2 = U \tan^2 \theta + V \tan \theta + W \qquad (2\text{-}5)$$

where U, V and W are refinable parameters.

2.5.3.2 Specimen broadening contributions

The profile function is mainly used to simulate the specimen features, such as broadening due to domain size and microstrain. Gaussian, Lorentzian, Pseudo-voigt and Pearson VII are examples of analytical functions that are used, as shown below.[45]

Gaussian $$G = I_0 \exp\left\{-\ln 2\left(\frac{2\Theta - 2\Theta_0}{\omega}\right)^2\right\}$$ (2-6)

Lorentzian $$L = I_0\left\{1 + \left(\frac{2\Theta - 2\Theta_0}{\omega}\right)^2\right\}^{-n} \quad n=1;\ 1.5;\ 2.$$ (2-7)

Pseudo-Voigt $$PV = \eta L + (1-\eta)G \qquad 0 \le \eta \le 1$$ (2-8)

Pearson VII $$P = I_0\left\{1 + \left(\frac{2\Theta - 2\Theta_0}{ma^2}\right)^2\right\}^{-m}$$ (2-9)

where 2Θ is the peak position, I_0 is the peak intensity, η is a mixing factor, ω is FWHM/2; FWHM represents the full width at half maximum, and m is shape parameter. Of the profile functions, the Pseudo-Voigt and Pearson VII functions produce better fits between observed and calculated patterns than the other two functions, since they include a mixing factor (η) and a variable shape parameter (m), respectively. In addition to these analytical functions, there are other models for the peak shape, such as peak half width functions.

The Rietveld method outputs microstructural features (domain size and microstrain) by refining the specimen broadening profile function. Domain size represents the average coherently diffracting size and microstrain means the extent of disorder inside the domains. Both domain size and microstrain can contribute to broadening of the XRD peaks. Domain size includes long range defects such as dislocation arrays (small angle boundaries), stacking faults, twins and grain boundaries, all of which can cause domain size broadening. Structural defects such as dislocations, solid solution elements and vacancies cause microstrain broadening.[48]

2.5.4 Evaluation of the goodness of fit

The pattern profile is calculated from equation 2-4 and compared point-by-point with the experimental pattern to refine the structure by achieving the best fit (whole pattern fitting). The parameters are then adjusted using the least-squares method by minimizing the residuals between the experimental and calculated

patterns. The best fit will depend on the competence of the model and on whether a minimum is reached. There are several criteria to judge the fit, as shown in Table 2-2.

Table 2-2 – Criteria for Rietveld refinement fitting[48]

Criterion of fit	Definition
R-pattern, R_p	$$R_p = \sqrt{\dfrac{\sum \left| Y_{obs} - Y_{cal} \right|}{\sum Y_{obs}}}$$
R-weighted pattern, R_{wp}	$$R_{wp} = \sqrt{\dfrac{\sum w(Y_{obs} - Y_{cal})^2}{\sum wY_{obs}^2}}$$
R-expected, R_{exp}	$$R_{exp} = \sqrt{\dfrac{\sum M - P}{\sum wY_{obs}^2}}$$
Goodness of fit, GoF	$$GoF = \dfrac{R_{wp}}{R_{exp}} = \sqrt{\dfrac{\sum w(Y_{obs} - Y_{cal})^2}{M - P}}$$

Y_{obs} and Y_{cal} are the observed and calculated data, respectively. In Table 2-2, M represents the number to the data points, P is the number of the parameters and w is the weighting given to each data point. Among all the criteria, the weighted residual error (R_{wp}) is the most meaningful from a mathematical point of view, since the numerator in the R_{wp} equation is the residual that is minimized in the least squares refinement procedure.

2.5.5 Application of the Rietveld method

The Rietveld method has been widely used to determine microstructural features, including domain size, microstrain, dislocation density, texture and phase weight fraction for a number of materials, although it has only been about 40 years since its development. Compared with other characterization techniques, such as SEM, TEM or EBSD, the Rietveld method can output quantitative microstructure information by analyzing the XRD pattern, which is collected from a relatively large sample size.

2.5.5.1 Grain/subgrain size determination

Among all the applications, domain size determination is the most conventional and domain size is always interpreted to be either grain size or subgrain size. Grain size characterization is always conducted by OM, SEM and EBSD. Traditionally, TEM is adopted to characterize subgrain structure and is capable of analyzing individual subgrains and even individual dislocations. A significant amount of research related sub-structure characterization for steels has been done.[49] More and more studies of grain size or subgrain size determinations have been published in recent years, using X-ray diffraction line profile fitting with the Rietveld method; materials range from metals to powder materials.[50,51,52,53,54] However, the accuracy of the results obtained from the Rietveld method is always questionable. The sensitivity of the Rietveld method to domain size has been discussed in a number of studies, and the results from the Rietveld method have been compared with those from SEM, EBSD, TEM or other techniques. [54,55,56,57] In general, for fine-grained materials with a homogeneous microstructure composed of random high angle grain boundaries, the grain size or domain size obtained from EBSD, TEM and the Rietveld method are in good agreement. However, for materials with higher amounts of deformation, the microstructure values are highly dependent on the technique. In other words, if the material has a substructure of dislocation cells, a coherent domain size rather than a grain size is outputted by the Rietveld method, so the XRD data sometimes shows relatively smaller values than those obtained from TEM and EBSD. The differences result

from different sensitivities to grain or subgrain misorientations for the different techniques. EBSD and TEM have difficulty identifying misorientations smaller than 1º to 3º. For the Rietveld method, the misorientation test limit is still unknown; however, based on the literature, the misorientation limit for the Rietveld method should be smaller than that for EBSD. For example, in one study, the Rietveld method, EBSD and TEM were used to characterize the subgrain size for a Cu material, which had been subjected to equal channel angular extrusion processing with 12 passes. With both EBSD and TEM, the subgrain size obtained was 130 ± 80 nm and 165 ± 90 nm, respectively; however, the Rietveld method gave values of only 62 nm. Hughes et al. propose that EBSD and TEM provide data about the subgrain size and XRD provides information about the cell size.[58] "Cells are described as roughly equiaxed volumes where the dislocation density is well below the average and which are bounded by low angle dislocation boundaries. Subgrains are defined as dislocation free volumes surrounded by medium to high angle boundaries.[58]

2.5.5.2 Dislocation density

Another application for the Rietveld method is to obtain dislocation density in a bulk sample. A number of studies of dislocation density characterization for steel materials have been published using the Rietveld whole X-ray profile fitting technique.[59, 60] Dislocation density is not a direct output parameter of the Rietveld method; however, the domain size and microstrain values can be used to calculate the dislocation density, ρ_{disl}, (i.e., dislocation length present in a unit volume (cm/cm^3)).[61]

$$\rho_{disl} = (\rho_D \times \rho_S)^{\frac{1}{2}}$$

(2-10)

$$\rho_D = \frac{3}{D_S^2}$$

(2-11)

$$\rho_S = \frac{(K \times \varepsilon^2)}{|b|^2}$$

(2-12)

where D_s is domain size, ε is microstrain, ρ_{disl} is the dislocation density, ρ_D is the dislocation density deduced from the domain size, ρ_S is the dislocation density deduced from the microstrain, K is a constant; for a bcc structure K~14.4, and b is the Burgers vector; for a bcc crystal structure, b = |1/2[111]|.

2.5.5.3 Texture index

Texture analysis can also be conducted using the Rietveld method, and has been applied to various metals. Texture arises when crystallites in the material tend to orient more in one way, or in one set of ways. Since texture leads to redistribution of specific peak intensities, the distortion of reflection intensities can be modeled with some functions. There are two models used to correct for preferred orientation in XRD analysis, the March model and general spherical harmonics (GSH). The latter method is used in this work. The texture index J is used to evaluate the magnitude of the texture from equation 2-12, as described elsewhere.[48, 62]

$$J = 1 + \sum_{l=2}^{L} \left(\frac{1}{2l+1} \right) \sum_{m=-l}^{l} \sum_{n=-l}^{l} \left| C_l^{mn} \right|^2$$

(2-13)

where C_l^{mn} is the spherical harmonics parameter obtained in the Rietveld refinement program.

If the material is randomly oriented, J should be equal to 1; otherwise J is larger than 1. J has a larger value for materials with stronger preferred orientation. For a single crystal, J is infinity.

3.   EXPERIMENTAL METHODS

In this section, data for the steels investigated, including composition, processing parameters, mechanical properties and CCT diagrams is presented. This is followed by the methodology for sample preparation categorized according to different techniques, such as XRD, OM, SEM, TEM, EBSD and WDS.

3.1 Steels studied

Seven microalloyed steels were studied, including four X80 pipeline steels and three X100 experimental plate steels with different processing histories. All X80 steels were provided by Evraz Inc. NA from production trials and the X100 steels were laboratory heats produced for Evraz Inc. NA by CANMET. Compositions and processing parameters were provided by these two organizations.

All steels were subjected to a controlled rolling schedule in which approximately 70% reduction was applied between the no-recrystallization temperature and the FRT. Following rolling, the steels were subjected to different accelerated cooling rates to different interrupted cooling temperatures.[63]

3.1.1 X80 steels

Table 3-1 lists the chemistry and processing parameters for the X80 steels. All the X80 steels have the same alloying elements, including C, Mn, Si, Al, N, Cu, Ni, Mo, Nb, Ti, V, with slight differences in actual contents. The processing parameters listed include FRT, CT and CR. They are listed as normalized values. The FRT, CT and CR are normalized relative to the actual values for the X100-2A steel. Symbol "*" represents expected values, instead of actual numbers. Slight differences in FRT and CT exist.

Table 3-1 - Nominal composition and processing parameters for X80 steels

Sample ID	X80	X80	X80	X80
Heat Number	462	A4B	A4F	B4F
Type	pipe	pipe	Pipe	pipe
C	0.030	0.035	0.052	0.052
Mn	1.69	1.70	1.77	1.62
Si	0.270	0.283	0.115	0.128
Al	0.044	0.044	0.016	0.020
N	0.0098	0.0058	0.0055	0.0061
Cu	0.27	0.34	0.15	0.15
Ni	0.13	0.25	0.41	0.41
Cr	0.05	0.07	0.08	0.06
Mo	0.297	0.305	0.404	0.299
Nb, Ti, V	0.106	0.114	0.056	0.089
FRT	0.94	1.05	1.00	1.00
CT	1.47	1.32	1.28	1.42
CR	0.44*	0.44*	0.44*	0.44*

Symbol "*" represents expected values, instead of actual numbers.

Table 3-2 includes the thickness and the mechanical properties for the four X80 steels, including yield strength (YS), ultimate tensile strength (UTS), total elongation (TEL) and toughness values, which are provided by Evraz Inc. NA. All four X80 steels have similar values for both yield strength and ultimate tensile strength. X80-462 and X80-A4B pipes are thinner than the others and have better toughness.

Table 3-2 – Mechanical properties and thickness of X80 steels

Sample ID		X80	X80	X80	X80
Heat Number		462	A4B	A4F	B4F
Thickness (mm)		11.8	12.1	15.6	15.1
0.5% EUL YS (MPa)*		588	568	589	592
UTS (MPa) *		703	694	717	735
TEL (%)*		34	35	39	37
CVN**	Test temperature (°C)	-7	-7	0	0
	Absorbed energy (Joule)	173	211	131	123

CVN represents Charpy V-nortch.
* Specimen for tensile testing: 10.2 mm in diameter, 40.6 mm in gauge length.
** Specimen for Charpy testing: full size (0.01 m × 0.01 m).

Figure 3-1 shows the CCT diagram for a typical X80 steel. The X80 steels in this work had a normalized cooling rate of 0.44 as listed in Table 3-1. At this rate a mixture of polygonal and bainitic ferrite is obtained.[64]
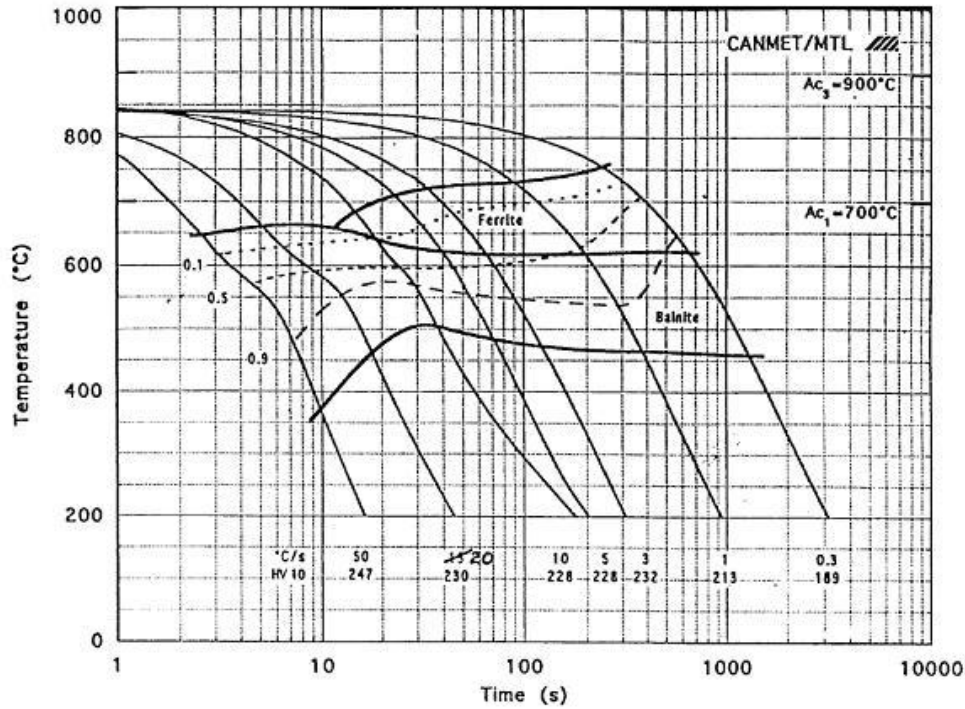
Figure 3-1 – CCT diagram for typical X80 steels.[64]

3.1.2 X100 steels

Table 3-3 lists the chemistry and processing parameters for the X100 steels used in this work. X100-2A has lower C, Si, Al, Nb and V contents than the others (X100-2B and X100-3C) and B has been added to this steel as well. X100-2B has the highest C, Al and V content. X100-3C has similar chemistry to X100-2B, but it has the lowest CR, close to half the CR of X100-2A and X100-2B. Compared to the X80 steels, generally X100 steels have relatively higher C, Mn, Mo and Cr levels. The CR values are generally higher and CT values are lower for X100 steels than X80 steels. The FRT, CT and CR are normalized relative to the actual values for the X100-2A steel. Symbol "*" represents expected values, instead of actual numbers.

Table 3-3 – Nominal composition and processing parameters for X100 steels

Sample ID	X100	X100	X100
Heat Number	2B	2A	3C
Type	plate	Plate	plate
C	0.065	0.039	0.064
Mn	1.87	1.81	1.88
Si	0.220	0.110	0.330
Al	0.032	0.018	0.024
N	59 ppm	50 ppm	63 ppm
Cu	0.16	0.34	0.15
Ni, Cr, Mo	1.01	1.05	0.99
Nb, Ti, V	0.126	0.053	0.058
B	-	11 ppm	-
FRT	1.00*	1.00*	1.00*
CT	0.90	1.00	1.14
CR	0.97	1.00	0.55

Table 3-4 shows the thickness and the mechanical properties for the three X100 steels, including YS, UTS, TEL and toughness values, which are provided by Evraz Inc. NA. Compared to the X80 steels, generally the X100 steels exhibit higher strength and toughness. Among the three X100 steels, X100-2A has a much higher YS, which is believed to be mainly due to the presence of B. Boron shifts the CCT diagram to longer times, promoting the formation of stronger phases. X100-2B has the highest toughness, which is possibly due to the combination of higher CR and lower CT. Bai et al. has extensively studied the relationship between microstructure and mechanical properties of high strength linepipe steels with the same material. It was found that a high volume fraction of M/A and a coarse M/A phase both reduced the toughness. A high CR and low CT resulted in fewer M/A islands.[65]

Table 3-4 – Mechanical properties and thickness for X100 steels

Sample ID		X100	X100	X100
Heat Number		2B	2A	3C
Thickness (mm)		14.0	14.4	14.6
0.5% EUL YS (MPa)		691	810	744
UTS (MPa)*		793	907	846
UEL (%)*		6.2	5.2	5.8
TEL (%)*		20	17	21
CVN**	Test temperature (°C)	-15	-15	-15
	Absorbed energy (Joule)	241	178	175

∗ Specimens for tensile testing: 10.2 mm in diameter, 40.6 mm in gauge length.
∗∗ Specimens for Charpy testing: full size (0.01 m × 0.01 m).

3.2 Sample preparation and instrument parameters

Detailed sample preparation procedures and working conditions corresponding to different techniques are illustrated here, including XRD, OM, SEM, TEM and WDS. In particular, the development of the Rietveld method is included in the XRD section.

3.2.1 X-ray diffraction

Seven steels were included in the XRD analysis, and five locations through the thickness were chosen for each steel. Microstructural features including subgrain size, dislocation density, texture index and phase fraction of retained austenite were obtained by quantifying the XRD pattern using the Rietveld method.

3.2.1.1 Experimental conditions for X-ray diffraction analysis

The experimental conditions for XRD analysis are shown in Table 3-5. X-ray diffraction patterns were collected from a Rigaku Geigerflex Power Diffractometer with a Co target and a wavelength of 0.17889 nm. Scanning angles (2θ) ranged from 40º to 125º for the steel samples and 20º to 125º for the standard material LaB_6. The step size was 0.02º. Table 3-5 lists all the detailed experimental information for XRD analysis.

Table 3-5 – Instrument parameters for XRD

Instrument	Rigaku Geigerflex 2173 Power Diffractometer
Target	Co, Wavelength of 0.17889 nm
Receiving slit	0.6mm
Divergent slit	1°
Counting speed	0.5° (2θ)/minute
Scanning angles (2θ)	40° to 125°
Step size	0.02° (2θ)/step

3.2.1.2 Quantitative software

For the Rietveld refinement, Topas Academic Software Version 3 was adopted in this study to obtain domain size, microstrain and other parameters related to preferred orientation. The instrument contribution profile function to a sample pattern was modeled using a LaB_6 standard material, which was assumed to have no domain size and microstrain broadening effects.

The parameters obtained from the Topas software include domain size D_s, microstrain ε and the general spherical harmonics factor C_l^{mn}. The texture index was analyzed based on the values of spherical harmonics factors. In addition, domain size and microstrain values were used to calculate dislocation density.

3.2.1.3 Sample preparation

Preparation methodology

One difficulty for XRD to characterize the microstructure through the pipe thickness is that X-rays can only penetrate about 200 μm beneath the steel surface. The steel thickness was at least 10 mm, so slicing the bulk steel sample into

several thin pieces was necessary to obtain microstructure information through the pipe thickness. The cutting process may affect the microstructure of material on the sectioned surface, so suitable sample preparation was necessary to eliminate this effect.

A heat treated X80 (X80-462) sample was used to examine the effect of sample preparation on the XRD results. A bulk sample was cut from X80-462 pipe and sized to 1cm × 1cm × thickness of the pipe. The bulk sample was heated to 625°C for 2 hours to relieve any internal stress and then furnace cooled. One slice with a thickness of about 2 mm, was sectioned from each pipe surface. The two thin pieces were parallel to the pipe surfaces, and were mounted using epoxy resin so that the surface could be examined.

The mounted samples were then ground and polished according to the following schedule (standard metallographic preparation procedure):

1) Grinding was done sequentially using 240, 320, 400 and 600 grit SiC papers.

2) Polishing was done using 6 μm followed by 1 μm diamond polishing compounds.

3) Final polishing was done with a 0.05 μm alumina slurry.

X-ray diffraction patterns were then collected from the two pipe surfaces and microstrain values were obtained using the Rietveld method. The microstrain values for both slices were around 2%, so the microstrain through the pipe thickness was assumed to be uniform, at around 2%, after annealing.

Several different sample preparation procedures were tried in this study. Firstly, an annealed bulk sample was cut into several thin slices, which were parallel to the pipe surfaces, and then subjected to the standard metallographic preparation procedure as described above. In order to avoid any welding effects, the bulk sample was cut from an area away from the welding zone, as shown in Figure 3-2. This figure also schematically shows the sample preparation process and the test locations for XRD analysis.

Outer surface

Inner surface

——————— Section

–·–·–·–·– XRD test position
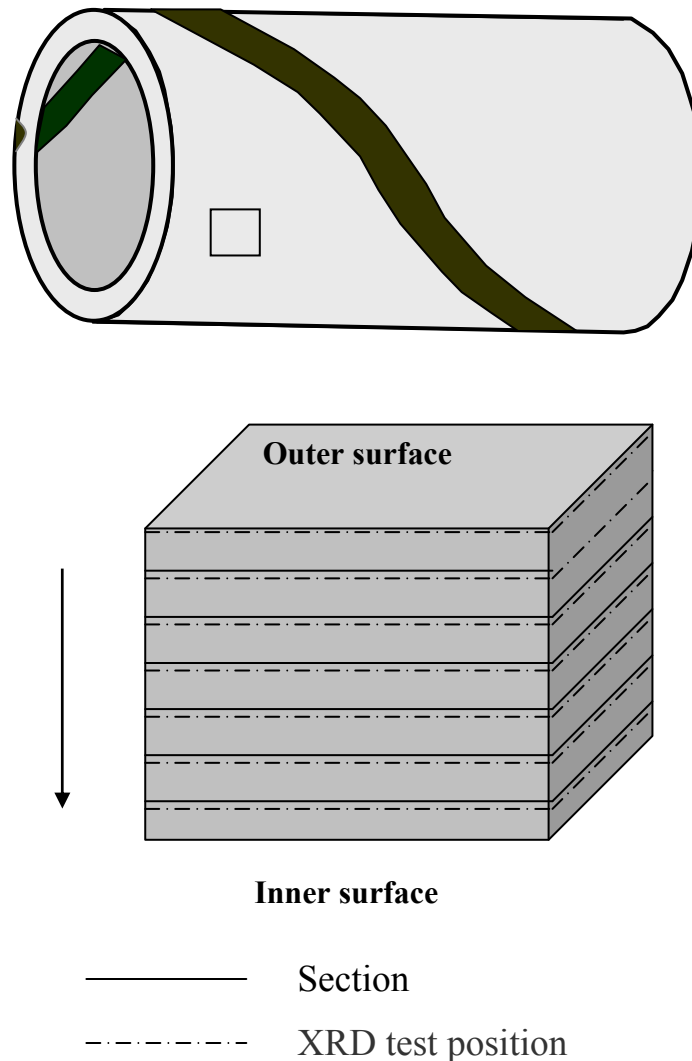
Figure 3-2 – Schematic showing XRD sample preparation from a microalloyed steel pipe.

Microstrain values for each thin slice were obtained using the Rietveld method. Figure 3-3 shows the variation in microstrain at different locations through the thickness. Normalized positions 0 and 1 represent inner and outer pipe surfaces, respectively. The microstrain values vary from 1.7 % to 4.7 % with an increasing trend in microstrain values from 0 to 9/10. This indicates that with sectioning deeper along the thickness direction, there are stronger effects due to the cutting process.
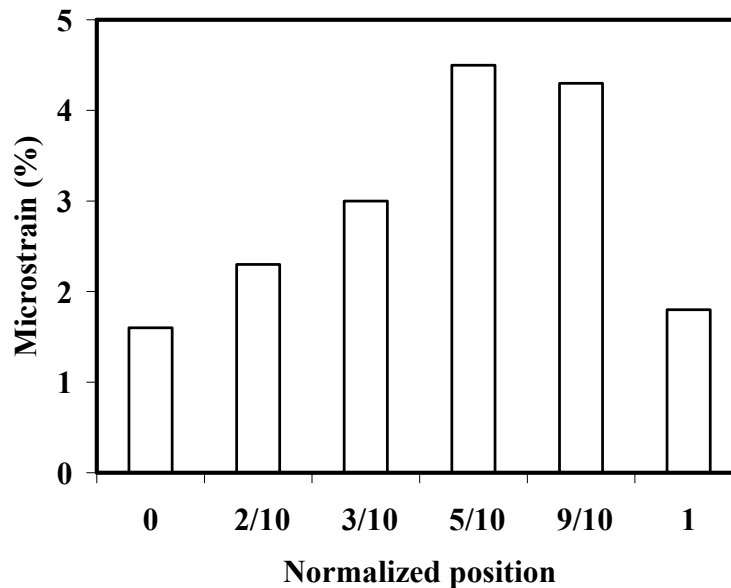
Figure 3-3 – Microstrain value vs. normalized position for annealed X80-462 steel after mechanical polishing. Normalized positions 0 and 1 represent inner and outer pipe surfaces, respectively.

This sample preparation procedure provided an indication that mechanical polishing cannot fully remove the effects introduced by the cutting process, especially when a bulk sample has undergone several cuttings.

Since mechanical polishing did not fully remove the affected layer produced by sectioning, electropolishing was done after the standard metallographic preparation process. The electrolyte used was composed of 1% tetramethylammonium chloride, 10% acetylacetone and methanol. To optimize the electropolishing conditions, several tests were conducted at different electropolishing temperatures (room temperature to 80ºC), currents (2mA to 10mA) and times. A current of 4 mA at room temperature was found to remove most of the surface preparation effects on the sample surfaces. After standard metallographic preparation, the surface layer (about 50 μm thick) removed by electropolishing was established to be effective in removing the damaged layer. The electropolishing time was around 16h to remove 50 μm from each slice.

Table 3-6 shows both microstrain and subgrain size values for five thin slices subjected to this procedure. Charts for variation of microstrain and subgrain size

values with normalized position are shown in Figure 3-4 and Figure 3-5, respectively. Normalized positions 0 and 1 represent inner and outer pipe surfaces respectively. The microstrain values are all close to 2 % and the subgrain size through thickness is relatively uniform. The error bars indicate the error of the Rietveld method technique itself. These are the standard deviations of outputs from the Rietveld method for different XRD patterns, which were obtained from the same sample.

Table 3-6 – Microstrain and subgrain values through pipe thickness for annealed X80-462 after removing 50 μm by electropolishing

Microstrain (%)				Subgrain Size (nm)		
First Run	Second Run	Average	Normalized Position	Average	First Run	Second Run
1.8	2.0	1.9	0	101	101	101
1.2	1.0	1.1	2/10	88	90	86
1.8	1.8	1.8	3/10	103	103	102
1.6	1.8	1.7	5/10	98	98	98
1.7	1.6	1.7	8/10	91	91	91

Normalized positions 0 and 1 represent inner and outer pipe surfaces respectively.
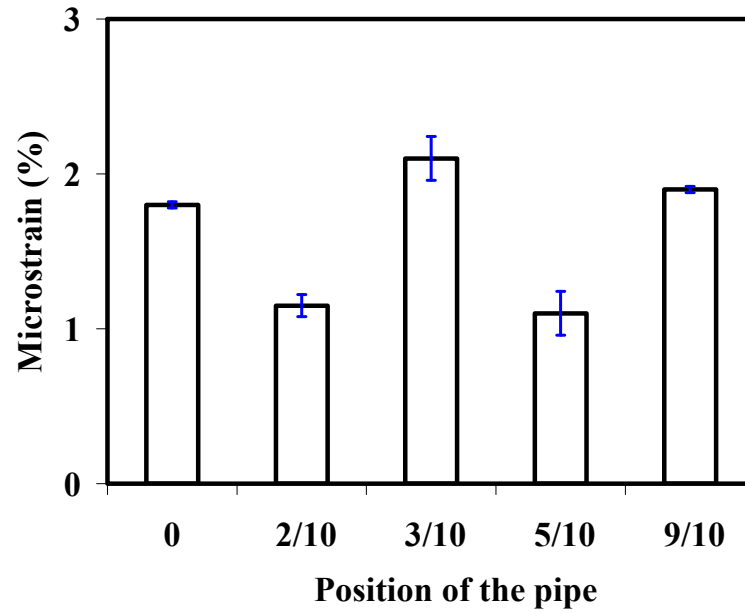
Figure 3-4- Microstrain value vs. normalized position for annealed X80-462 steel after removing 50 μm by electropolishing. Normalized positions 0 and 1 represent inner and outer pipe surfaces, respectively.
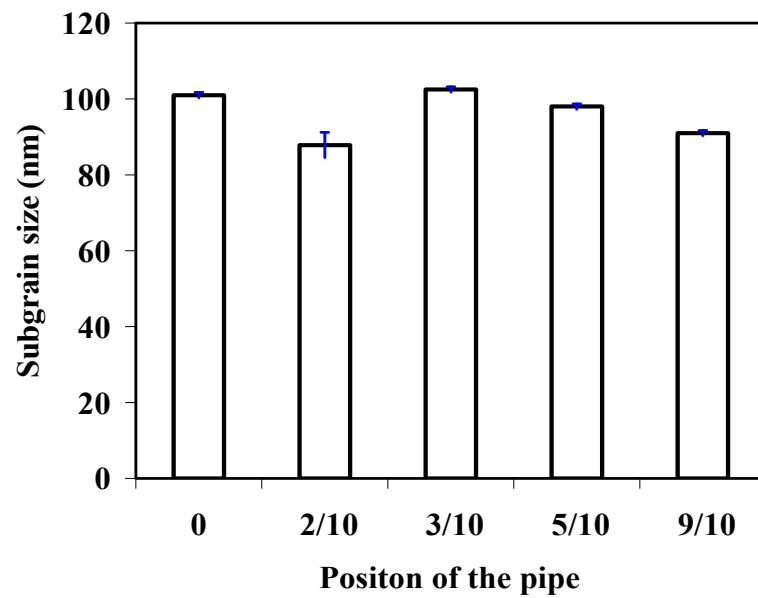
Figure 3-5 – Subgrain size vs. normalized position for annealed X80-462 steel after removing 50 μm by electropolishing. Normalized positions 0 and 1 represent inner and outer pipe surfaces, respectively.

Sample preparation

The bulk samples for all seven studied microalloyed steels were sectioned from the pipe or plate to sizes of approximately 1 cm × 1cm × thickness, using a linear precision saw with an Al_2O_3 blade. All thin slices were subjected to standard metallographic preparation followed by electropolishing to remove 50µm of surface material. The analyzed locations for the seven steels are listed in Table 3-7. Normalized positions 0 and 1 represent inner and outer pipe surfaces respectively.

Table 3-7 – XRD analyzed locations for seven studied steels

Steels	Sectioned locations				
X80-462	0	1/10	5/10	7/10	1
X80-A4B	0	3/10	5/10	8/10	1
X80-A4F	0	3/10	5/10	8/10	1
X80-B4F	0	4/10	5/10	8/10	1
X100-2B	0	3/10	5/10	7/10	1
X100-2A	0	3/10	5/10	7/10	1
X100-3C	0	3/10	5/10	7/10	1

Normalized positions 0 and 1 represent inner and outer pipe surfaces, respectively.

3.2.1.4 X-ray diffraction patterns

Detailed information for a theoretical pattern for iron, including peak indices with corresponding relative intensities and d spacings, is listed in Table 3-8.[66] All these intensities were normalized with respect to the 110 peaks. For an ideal material, all peaks are sharp vertical lines with no broadening.

Microstructural features are analyzed based on peak positions, peak widths and relative intensities. Phases are indexed based on the peak positions and

according to relative intensity values, texture information is extracted. In addition, domain size (grain size or subgrain size) and microstrain values are obtained by analyzing the peak widths.

Table 3-8- Information for an Fe theoretical pattern[66]

Fe, a = 0.28664 nm		
(hkl)	Relative Intensity	d (nm)
(110)	100	0.20268
(200)	20	0.14332
(211)	30	0.11702
(220)	10	0.10134
(310)	12	0.09064
(222)	6	0.08275

Within a scanning range of 40° to 125°, only four peaks for the ferrite phase are obtained for steels, as illustrated in Figure 3-6. Detailed information based on this pattern can be obtained using Jade-7 software, as shown in Table 3-9, which includes the Miller indices (hkl), peak positions, relative intensities and d spacings. All these intensities were normalized with respect to the (110) peaks.
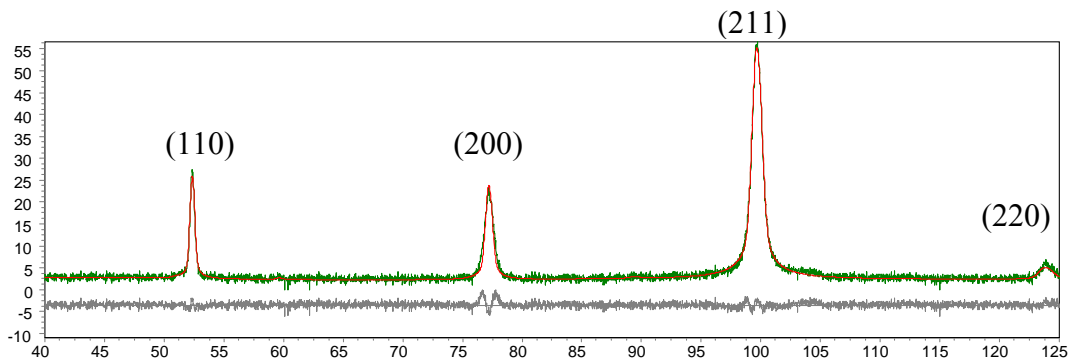
Figure 3-6 – XRD pattern for X100-2B steel at normalized position 5/10.

Table 3-9 - Peak information for XRD pattern in Figure 3-6

(hkl)	Peak position (2θ)/degree	Relative Intensity	d (nm)
(110)	52.2	100.0	0.20268
(200)	77.1	71.3	0.14332
(211)	99.5	417.3	0.11702
(220)	123.7	5.0	0.10134

The theoretical XRD pattern for ferrite indicates that the most intense peak is the (110) peak; however, the (211) peak is the most intense for the actual pattern (Figure 3-6). This is an indication that the sample exhibits some texture. Texture analysis using the Rietveld method will be included in the Results section. Domain size and microstrain values are two other outputs of the Rietveld method, as well as phase fraction for any retained austenite.

3.2.2 OM

Small samples were cut along the S-T surface (Figure 3-7) for the seven steels and mounted using epoxy resin. The exposed surfaces were then subjected to standard metallographic preparation and etched with 2% Nital etchant (i.e., 98% ethyl alcohol and 2% nitric acid) for approximately 1 minute to reveal the microstructural features. Microstructure analysis for each sample was done at two areas, as shown in Figure 3-7; one region is close to the pipe surface and the other is near the center of the pipe.
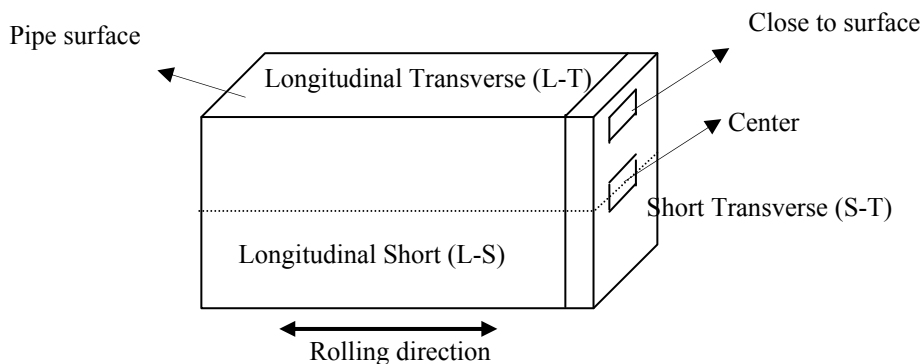
Figure 3-7 - Schematic showing sectioning of samples for OM analysis.

3.2.3 SEM

The SEM was used to analyze grain morphology at higher resolution than was possible with OM. The seven microalloyed steels were examined using SEM, with a sample preparation procedure the same as that described in the OM section. The analyzed areas for each sample are also the same as that analyzed using OM. SEM analysis for was carried out using a Hitachi S-2700 SEM, operated at a voltage of 20 kV and a working distance of 17 mm.

3.2.4 TEM

A 1mm thick slice was cut from the inner surface of both the X80-462 pipe and the X100-V5007 plate and polished to a thickness of approximately 50 μm using standard metallographic preparation. The inner surface corresponds to the normalized position 0 for XRD analysis. 3 mm discs were then punched using a disc punch specifically made for this purpose. These discs were jet-polished using a Tenupol twin jet electropolisher, until a small perforation was achieved. Narrow areas at the edge of the perforation, which are thin enough (<100 nm) to be transparent to electrons in the TEM, were obtained. The solution was composed of 80% (volume) concentrated hydrogen peroxide, 5% hydrofluoric acid and 15% distilled water. The jet polishing was done at room temperature at a voltage of 80 V and a current of 75 mA. The polishing time was approximately 2 minutes for each sample. Once perforated, the samples were immediately extracted from the polisher and cleaned using ethanol to remove residual etchant and prevent oxidation of the surface.

A JEOL 2010 TEM was used to obtain bright field (BF) images, dark field (DF) images and selected area diffraction (SAD) patterns to verify the subgrain shape and size and phase morphology. The TEM used was operated at 200 kV.

3.2.5 EBSD

Subgrain size analysis for microalloyed steel X80-462 was conducted using EBSD. The sample preparation was the same as that described in the XRD section. Three positions through thickness were included in this study, which

correspond to the normalized positions of XRD analysis, 0, 5/10 and 1. The EBSD study was conducted with JEOL 7000F SEM. The step grid size was 25nm. The scanning conditions included a beam voltage of 25 kV, a working distance of 15 mm and a sample tilt of 70º. The pattern was automatically analyzed using the Channel 5 Flamenco software from HKL Technology. Postprocessing of the EBSD data (subgrain size measurement) was undertaken using the VMAP package from J. Humphreys.[67]

3.2.6 WDS

Quantitative chemical analysis for five microalloyed steels (X80-462, X80-A4B, X80-A4F, X80-B4F and X100-2A) was conducted using a JEOL 8900 microprobe, equipped with five wavelength dispersive spectrometers. The sample preparation procedure was the same as that described in the OM section. Fifty positions were analyzed for each sample along the S-T direction. For each position, a small surface (approximately 1 μm^2) was analyzed. The microprobe was operated at an energy of 15 kV, with a beam current of 15 nA.

4.   RESULTS

The results of the experimental work outlined in Chapter 3 will be presented in this chapter. In the first section, a detailed description of how refinement was undertaken will be illustrated with two examples of refinement. In the second section, microstructural features for the seven steels determined by XRD diffraction are presented. In the last section of this chapter, OM, SEM, TEM and WDS results are included.

4.1 Rietveld refinement procedure

A calculated XRD pattern is based on both instrumental parameters and sample microstructure. Therefore, in the Rietveld refinement program, there are two main parts as well, instrument related inputs and microstructure feature based inputs. In this study, the LaB_6 pattern was used to determine the instrumental contribution profile function, followed by the steel sample microstructure refinement.

4.1.1 Instrumental parameters

Table 4-1 lists all the general instrumental parameters needed in the Rietveld method. The left column lists parameters in the Rietveld refinement and the right column includes the corresponding names or symbols used in the Topas software.

Table 4-1 –Instrumental parameters in the Rietveld refinement

Parameter	Topas parameter name
Wavelength	CoKα3 (0.0001)
Lorentz-polarization factor	LP_Factor (31.1)
Zero error (2θ)	Zero_Error (ze, 0.006)
Simple axial model (mm)	Simple_Axial_Model (rsl, 12.8)
Instrumental profile	UVW (0.01011, -0.06567, -0.06992)
Background	bkg

For CoKα3 (0.0001), 0.0001 represents the error in Å corresponding to the wavelength for the incident X-ray. The second parameter is the lorentz-polarization (LP) factor. For unpolarized radiation, LP factor is equal to 0, e.g., x-ray diffractometers without any monochromator. For fully polarized radiation, it's equal to 90, e.g., synchrotron radiation. In this study a Co target was used with an LP factor equal to 31.1. Zero error means the error in the setting of the zero point of the 2θ scale. The simple axial model is a parameter to describe peak asymmetry due to axial divergence, which could be obtained by LaB_6 standard material refinement.

As described in the last chapter, the instrumental profile function (Caglioti formula) is typically been modeled as [47]

$$H^2 = U \tan^2 \theta + V \tan \theta + W \qquad (4\text{-}1)$$

where U, V and W are refinable parameters.

The background function accounts for the contribution from incoherent scattering and air scattering, Higher-order polynomials are always used to model the background function. In this study, a fifth-order polynomial was used and fit quite well.

4.1.2 Sample parameters

Table 4-2 lists all the sample related parameters. The left column lists parameters for Rietveld refinement and the right column includes the corresponding names or symbols used in Topas software. Specimen displacement represents the vertical displacement of the sample in millimeters, x, y and z are the position coordinates and occ represents the extent of site occupancy, with a minimum and maximum of 0 and 1, respectively. Preferred orientation is corrected by a spherical harmonics function in this study. The texture index value is calculated using parameters of the spherical harmonics function, i.e., sh_c00, sh_c41 and sh_c61, using equation 2-13. The LVol_FWHM_CS_G_L (k, Lvol, kf, csgv, cslv) function (Pseudo-Voigt function shown by equation 2-8) is used to correct for the domain size broadening effect, where k is a shape factor and is set to 1. kf is another shape factor whose default value is 0.89, csgv represents the Gaussian component (equation 2-6) and cslv is the Lorentzian component (equation 2-7). Lvol, which represents the domain size, is a direct output. The e0_from_the strain (ε, sgv, slv) function is used to simulate the strain broadening effect, where sgv and slv represent Gaussian (equation 2-6) and Lorentzian components (equation 2-7), respectively, and ε is a direct output as well.

Table 4-2 – Sample parameters in the Rietveld refinement

Sample Parameter	Topas parameter name
Sample displacement	sd
Lattice position	x, y,z
Site occupancy	occ
Lattice parameter (nm)	lpA
Preferred orientation	Sh_c00
	Sh_c41
	Sh_c61
Domain size	LVol
Microstrain	ε /e0

4.1.3 LaB$_6$ refinement

In this study, the instrumental representing profile function, zero error and simple axial model parameter are obtained using a LaB$_6$ standard material. Table 4-3 lists a LaB$_6$ refinement example, including both the instrumental and specimen parameters discussed above. LaB$_6$ is assumed to be a standard material, with no microstrain and domain size broadening effects in the XRD patterns and no preferred orientation, so the sample parameter is limited to the lattice parameter. The lattice parameter from the refinement was 0.41565 nm, which is a small deviation from the theoretical value 0.416007 nm. Parameters, including (UVW) parameters, zero error and a simple axial model, obtained from the LaB$_6$ refinement, will be included in the steel sample refinements.

Table 4-3- Parameters in LaB$_6$ material refinement

Parameter	Value
LP Factor	31.1
Zero error (2θ)	0.00609
Simple Axial Model (mm)	12.80994
UVW	(0.01011, -0.06567, -0.06992)
Background function	(22.9, -21.6, 16.0, -7.1, 3.3, -0.6)
Lattice parameter (nm)	0.41565

4.2 Rietveld refinement examples

Two different refinement examples are given in this section, single phase refinement and two phase refinement (ferrite and retained austenite).

4.2.1 Single phase refinement

Parameters obtained from the LaB$_6$ refinement, (U, V, W), zero error and simple axial mode, are included in the steel sample refinement as the instrumental input and are fixed. This is followed by background fitting and specimen displacement adjustments. A fifth-order polynomial is used to fit the background. Specimen displacement represents vertical displacement of the sample in millimeters and it is always set to be refinable. The last part of the input is the microstructural features of the ferrite phase.

In the single phase refinement, the microstructural features are based on ferrite, including space group, lattice parameter, preferred orientation correction function, domain size and microstrain corrections. Figure 4-1 gives an example of single phase steel refinement (X80-462) and Table 4-4 includes the main parameters in the refinement program. The lattice parameter for ferrite in the

refinement result is 0.286899 nm. R_{wp} is equal to 11.596, showing good fitting which is also shown in Figure 4-1.
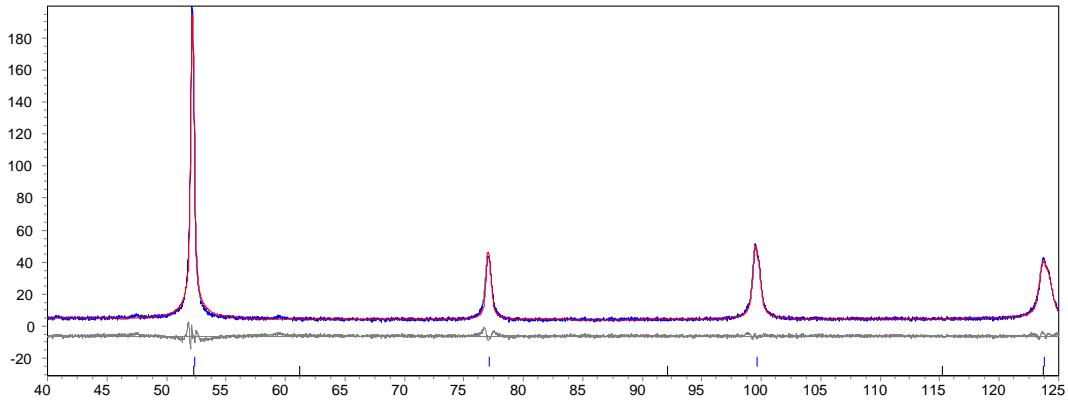
Figure 4-1 – An example of single phase steel refinement for X80-462 steel at normalized position 0.

Table 4-4 – Parameters included in single phase steel sample refinement corresponding to Figure 4-1

Parameter		Value or Content
Instrument parameters		
LP factor		31.1
Zero error (2θ)		0.00609
Simple axial model (mm)		12.80994
(U, V, W)		(0.01011, -0.06567, -0.06992)
Specimen displacement (mm)		0.15756
Sample parameters		
Structure		(I_m_-3_m, AlphaFe)
Lattice parameter (nm)		0.286899
Preferred orientation Correction	Sh_c00	1
	Sh_c41	0.33184
	Sh_c61	-0.74615
Domain size (nm)		303
Microstrain		7.1%
Goodness of fit		
R_{wp}= 11.596		

The domain size and microstrain values were used to calculate the dislocation density, ρ_{disl}, using equations 2-10, 2-11 and 2-12. The dislocation density calculated based on the values in Table 4-4 is 2.49 $\times 10^9$ cm/cm^3. The texture index J can be calculated from equation 2-13. C_l^{mn} is the spherical harmonics parameter obtained from the Topas refinement program. For the example shown in Table 4-4, J is equal to 1.055.

If the material is randomly oriented, J should be equal to 1, otherwise J is larger than 1. J has a larger value for materials with stronger preferred orientation. For a single crystal, J is infinity. However, how large values representing weak and strong texture should be defined. According to the results obtained from the Rietveld method, for steel X80-B4F, at position 0 the texture index value is equal to 1.01, which is close to 1. The XRD pattern (Figure 4-2) represents grains that are essentially randomly oriented. The normalized intensities for the XRD pattern shown in Figure 4-2 are 100, 3.9, 10.4 and 4.1 for peaks (110), (200), (211), and (220) respectively. All these intensities were normalized with respect to the intensity of 110 peaks. As shown in Figure 4-2, normally the first peak is the highest peak among the four peaks of ferrite within the 2θ range of 40° to 125°.

At position 1/2 for the same steel, the texture index is equal to 1.27; the corresponding XRD pattern is shown in Figure 4-3. The normalized intensities for the XRD pattern are 100, 37.9, 296.3 and 5.2 for peaks (110), (200), (211), and (220) respectively. All the intensities were normalized with respect to (110) peak intensity. The (211) peak ferrite is higher than the first peak and the relative intensity for second peak has increased in comparison with that of the randomly oriented XRD pattern. This confirms that texture is occurring and is not negligible. According to the XRD patterns and texture index values obtained from the Rietveld method, a texture index value of 1.27 represents strong texture in a microalloyed steel sample.
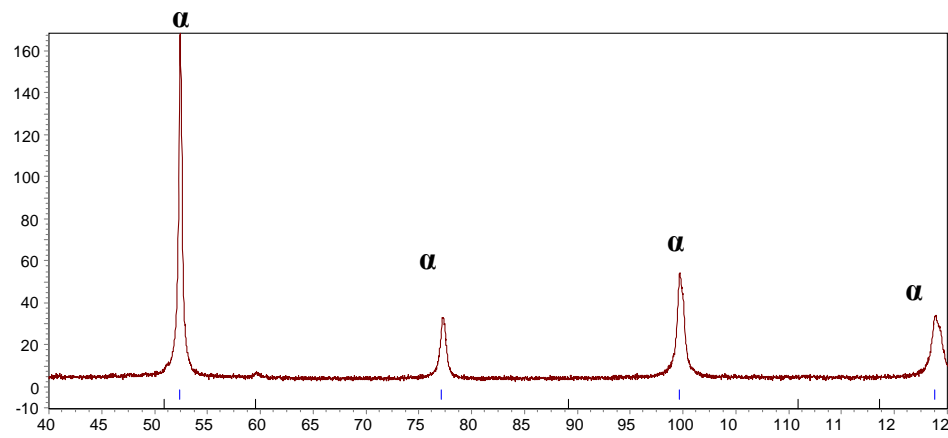
Figure 4-2 – XRD pattern corresponding to X80-B4F steel at normalized position 0.
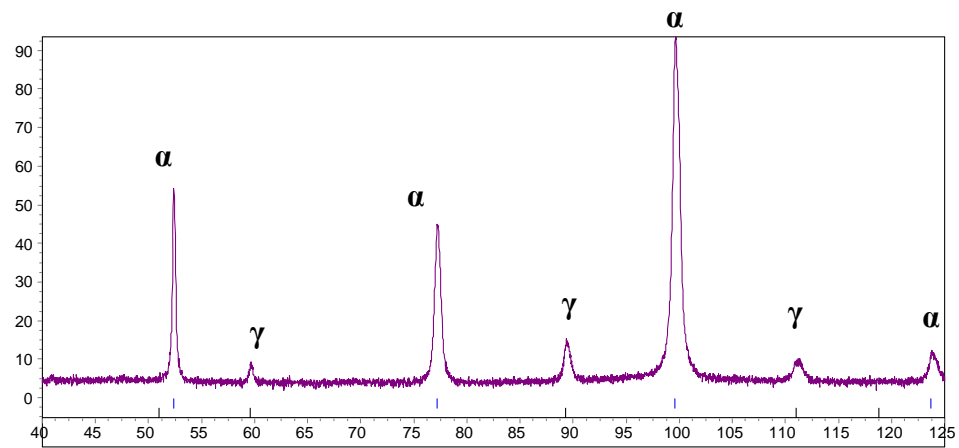
Figure 4-3 - XRD pattern corresponding to X80-B4F steel at normalized position 1/2.

4.2.2 Two phase refinement

The retained austenite contribution should be added to the single phase refinement. The function MVW to correct phase fraction is incorporated for each phase. M, V and W represent the cell mass, cell volume and weight percent respectively.

Figure 4-4 shows an example of the two phase refinement and Table 4-5 lists the corresponding parameters in the refinement program. In addition to the parameters in Table 4-5, other parameters related to the retained austenite phase, such as preferred orientation correction, domain size and microstrain, are also included in the refinement to achieve the best fit

From the refinement results shown in Table 4-5, the lattice parameter for ferrite and retained austenite are 0.286891 nm and 0.360850 nm, respectively. Compared with the theoretical values of 0.287199 nm and 0.35680 nm, there are only small deviations. Good fitting is shown in Figure 4-4 with a low R_{wp} value as well.
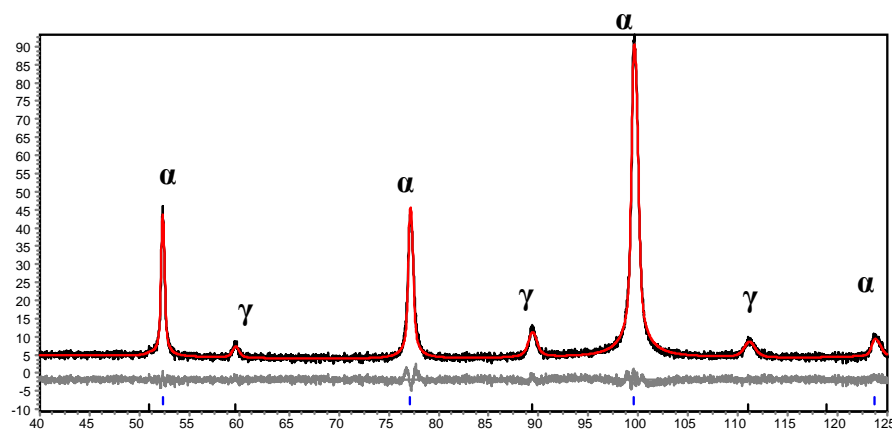
Figure 4-4 - An example showing two phase refinement for steel X80-A4F at normalized position 3/10.

Table 4-5 – Parameters included in two phase steel refinement

Parameter		Value or Content
Ferrite phase microstructural features		
Structure		(I_m_-3_m, AlphaFe)
Lattice parameter (nm)		0.286891
Preferred orientation Correction	Sh_c00	1
	Sh_c41	-1.03274
	Sh_c61	1.252215
Domain size (nm)		59
Microstrain		6.2
Phase weight fraction (wt%)		93.85
Retained austenite phase microstructural features		
Structure		(F_m_-3_m, Austenite)
Lattice parameter (nm)		0.360850
Retained austenite weight percent (wt%)		6.15
R_{wp} = 14.806		

For every refinement, instrumental parameters and background function should first be adjusted and then microstructure information for each phase sequentially added, such as crystallographic information, texture correction and then subgrain size and microstrain. The examples discussed above were applied to seven microalloyed steels and outputs including subgrain size, dislocation density, texture index and austenite phase weight fraction are reported in the next section.

4.3 Microstructural features by Rietveld method

In this section, microstructural features obtained from XRD are presented for seven steels as a function of thickness. Each steel was cut into five pieces and microstructural features include subgrain size, microstrain, dislocation density, texture index and retained austenite phase weight fraction. These are shown in Table 4-6 (X80-462), Table 4-7 (X80-A4B), Table 4-8 (X80-A4F), Table 4-9 (X80-B4F), Table 4-10 (X100-2B), Table 4-11 (X100-2A), and Table 4-12 (X100-3C). 0 and 1 represent inner and outer surfaces. Generally, X100 steels have a finer subgrain size (around 100 nm) and higher dislocation density than X80 steels. A detailed discussion is presented in next chapter.

Table 4-6 – Through thickness microstructural features for X80-462 steel

Normalized position	Subgrain size (nm)	Microstrain (%)	ρ_{disl} ($\times 10^9$) (cm/cm^3)	Texture index	Retained austenite (%)
0	303	7.1	2.5	1.055	-
1/10	404	5.9	1.6	1.033	-
5/10	388	4.9	1.3	1.088	-
7/10	248	6.0	2.6	1.093	-
1	135	5.9	4.7	1.045	-

Table 4-7 – Through thickness microstructural features for X80-A4B steel

Normalized position	Subgrain size (nm)	Microstrain (%)	ρ_{disl} ($\times 10^9$) (cm/cm^3)	Texture index	Retained austenite (%)
0	224	6.9	3.3	1.09	-
3/10	330	7.5	2.4	1.06	0.23
5/10	246	7.8	3.4	1.20	2.37
8/10	102	7.3	7.6	1.14	1.32
1	99	7.6	8.1	1.12	0.42

Table 4-8 - Through thickness microstructural features for X80-A4F steel

Normalized position	Subgrain size (nm)	Microstrain (%)	ρ_{disl} ($\times 10^9$) (cm/cm^3)	Texture index	Retained austenite (%)
0	148	7.7	5.5	1.01	0.84
3/10	59	6.2	11.2	1.23	6.15
5/10	150	7.0	5.0	1.26	6.12
8/10	187	7.7	4.4	1.01	1.02
1	139	6.5	5.0	1.07	0.20

Table 4-9- Through thickness microstructural features for X80-B4F steel

Normalized position	Subgrain size (nm)	Microstrain (%)	ρ_{disl} ($\times 10^9$) (cm/cm^3)	Texture index	Retained austenite (%)
0	154	6.7	4.6	1.01	0.20
4/10	241	6.8	3.0	1.21	7.05
5/10	223	8.3	4.0	1.27	7.02
8/10	185	6.9	4.0	1.15	2.10
1	202	6.7	3.5	1.01	0.20

Table 4-10 - Through thickness microstructural features for X100-2B steel

Normalized position	Subgrain size (nm)	Microstrain (%)	ρ_{disl} ($\times 10^9$) (cm/cm^3)	Texture index	Retained austenite (%)
0	95	13.6	15.2	1.01	-
3/10	52	12.8	26.2	1.17	-
5/10	50	11.7	24.9	1.34	-
7/10	87	14.8	18.1	1.02	-
1	68	15.0	23.4	1.09	-

Table 4-11 - Through thickness microstructural features for X100-2A steel

Normalized position	Subgrain size (nm)	Microstrain (%)	ρ_{disl} $(\times 10^9)$ (cm/cm^3)	Texture index	Retained austenite (%)
0	68	11.4	17.8	1.12	-
3/10	82	15.4	20.0	1.11	-
5/10	39	12.3	33.5	1.27	-
7/10	99	15.3	16.4	1.14	-
1	81	12.6	16.5	1.12	-

Table 4-12 -Through thickness microstructural features for X100-3C steel

Normalized position	Subgrain size (nm)	Microstrain (%)	ρ_{disl} $(\times 10^9)$ (cm/cm^3)	Texture index	Retained austenite (%)
0	75	11.7	16.6	1.08	0.20
3/10	153	13.3	9.2	1.01	0.20
5/10	68	11.5	18.0	1.32	0.20
7/10	91	10.7	12.5	1.32	1.77
1	94	12.5	14.0	1.06	0.60

XRD patterns at five positions for each steel are included in Appendix A, and corresponding figure numbers are listed in Table 4-13. The normalized intensity for XRD patterns and raw outputs from the Rietveld method are also attached in Appendix A, and corresponding table numbers are listed in Table 4-14. All the intensities are normalized with respect to the (110) peaks.

Table 4-13 – Figure number for XRD patterns through thickness in Appendix

Steels	Figure number for XRD pattern attached in Appendix				
X80-462	A-1	A-2	A-3	A-4	A-5
X80-A4B	A-6	A-7	A-8	A-9	A-10
X80-A4F	A-11	A-12	A-13	A-14	A-15
X80-B4F	A-16	A-17	A-18	A-19	A-20
X100-2A	A-21	A-22	A-23	A-24	A-25
X100-2B	A-26	A-27	A-28	A-29	A-30
X100-3C	A-31	A-32	A-33	A-34	A-35

Table 4-14 – Table number for XRD normalized intensity and raw outputs of the
Rietveld method in Appendix

Steels	Table of Normalized intensity	Table of direct output of Rietveld method
X80-462	A-1	A-8
X80-A4B	A-2	A-9
X80-A4F	A-3	A-10
X80-B4F	A-4	A-11
X100-2A	A-5	A-12
X100-2B	A-6	A-13
X100-3C	A-7	A-14

4.4 General microstructure analysis

For all seven steels, the microstructure through the pipe or plate thickness as obtained by OM and SEM are presented in this section. For two steels (X80-462 and X100-2A), TEM analysis was conducted on the pipe or plate surface. WDS was used to analyze the variation in alloying element contents through the pipe/plate thickness.

4.4.1 OM and SEM Analysis

Initial metallographic observations using OM were performed to identify the microstructure differences through the pipe or plate thickness. The images were taken along the S-T direction, one from the edge near the pipe surface and the other near the centerline, shown by Figure 3-7. The highest magnification for OM, 1000X, was used to present the morphology. SEM was also used to identify the morphology at higher magnification. A magnification of 2500X was used in this study.

4.4.1.1 X80 steels

The OM images for the X80-462 steel, taken near the edge and the centerline are shown in Figure 4-5 (A) and (B), respectively. The matrix is mainly composed of acicular ferrite (AF) with areas of polygonal ferrite (PF). Generally acicular ferrite is defined as highly substructured, non-equiaxed ferrite and is indicated by arrows in the images. The grains, shown in Figure 4-5, are mostly irregular in shape and elongated along the rolling direction and more elongated near the surface. Coarsened grains were obtained at locations near the center of the pipe compared with areas near the pipe surface. SEM images for X80-462 steel taken around the surface and the centerline are shown in Figure 4-5 (C) and (D) respectively. No major differences in morphology at different locations through the pipe thickness were observed. A pearlite-like microstructure was found in some areas. No obvious retained austenite regions were observed either by OM or SEM, which is consistent with the result obtained by XRD.

For the other three X80 steels (i.e., X80-A4B, X80-A4F and X80-B4F), the morphology observed using OM and SEM was similar as that shown here for X80-462. The matrix is mainly composed of polygonal ferrite and acicular ferrite. Coarsened grains were observed by OM at the center of the pipe in comparison with the surface of the pipe. For X80-A4F and X80-B4F, retained austenite was detected using XRD, but no obvious retained austenite areas were observed using OM and SEM. It is possible that the lower carbon content may make it more likely for retained austenite to appear at ferrite grain boundaries areas and not in isolated areas. Only one steel (X80-462) is shown here; the other steels are presented in Appendix B, i.e., Figures B-1, B-2 and B-3 for X80-A4B steel, X80-A4F steel, and X80-B4F steels, respectively.
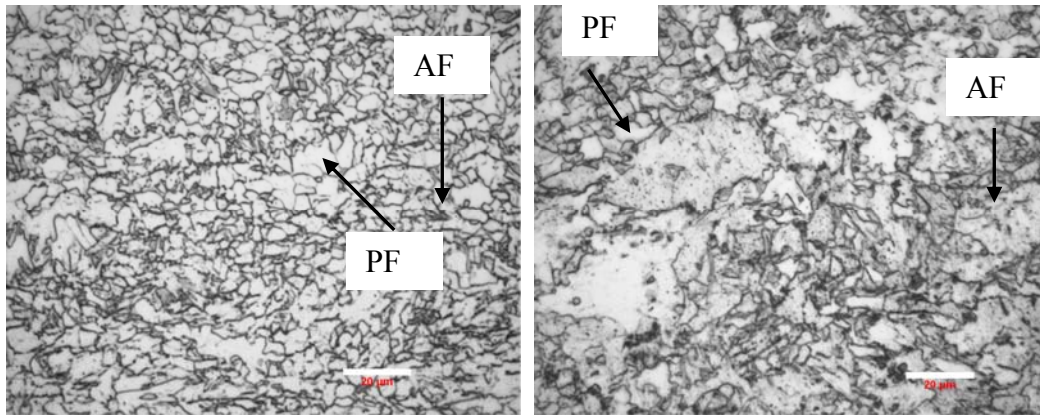
(A)

(B)
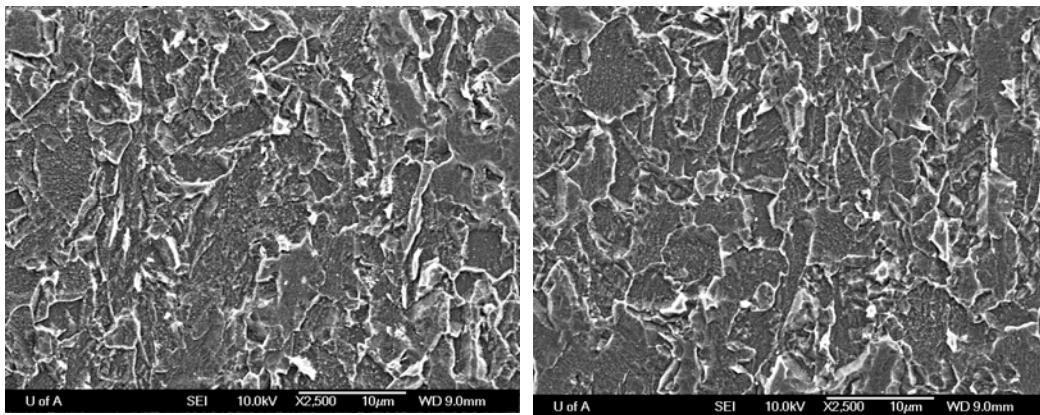
(C)

(D)
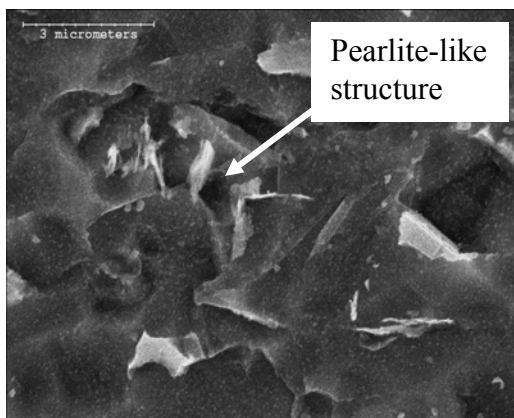
(E)

Figure 4-5 – Morphology for X80-462 steel along the rolling direction.
(A) OM image near the pipe surface. (B) OM image near the center of the strip.
(C) SEM image near the pipe surface. (D) SEM image near the center of the strip.
(E) Pearlite-like microstructure.

4.4.1.2 X100 steels

Compared to the X80 steels, X100 has relatively higher C, Mn, Mo and Cr contents. In terms of processing history, X100 steels have higher cooling rates and lower coiling temperatures. Both features can result in microstructure differences between the X100 and X80 steels.

The OM images for the X100-2A steels, taken from near the surface and the centerline are shown in Figure 4-6 (A) and (B) respectively. There were differences in morphology for the X100 steels compared with the X80 steels. The X80 steels are mostly composed of acicular ferrite with significant portion of polygonal ferrite; however, for X100 steels, the matrix is composed of mainly bainitic ferrite (B-F) and acicular ferrite (AF) as indicated by the arrows in Figure 4-6. This difference in grain structure morphology is shown more clearly in TEM images, which are included in the next section.

The grains for the X100 steels are also irregular in shape and elongated in the rolling direction. The OM images also show coarsened grains near the centerline. The SEM images show slight differences for the two different positions and no pearlite-like structure was obtained. The X100 steels all had similar morphology, only the microstructures for X100-2B steel are presented in this section. The microstructures for the other steels are presented in Appendix B as Figures B-4 and B-5 for X100-2A and X100-3C.
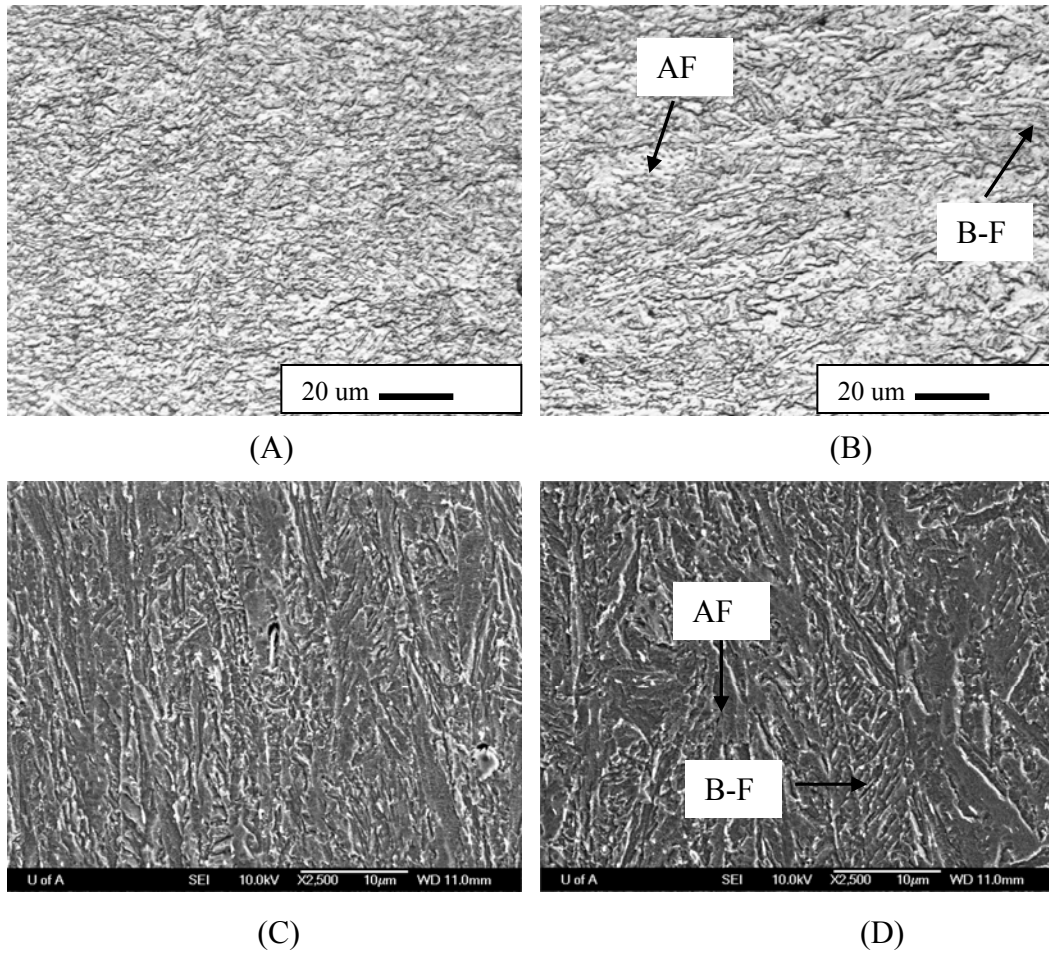
Figure 4-6 – Morphology for X100-2B steel along rolling direction.
(A) OM image near the pipe surface.   (B) OM image near the center of the strip.
(C) SEM image near the pipe surface.   (D) SEM image near the center of the strip.

4.4.2 TEM Analysis

OM and SEM were used to analyze the microstructures on a relatively large scale; however, they have the limitations in terms of resolution. To reveal more detailed microstructures, such as substructure, TEM has to be used. In this study, two steels were studied by TEM (X80-462 and X100-2A) and samples were taken from pipe or plate surfaces, which correspond to normalized position 0 from XRD analysis.

Figure 4-7 (A) is a TEM bright field (BF) image from a thin foil sample for the X80-462 steel pipe surface, at a magnification of 20,000X, and it shows that the matrix of the steel is mostly composed of acicular ferrite. At higher magnification (80,000X), the substructure (Figure 4-7(B)) and dislocation networks (Figure 4-7(C)) are observed. The subgrain size was measured by an intercept technique and this measurement included four different areas with 63 subgrains in total. The average size was 500 nm.

Figure 4-8 shows two TEM BF images from a thin foil sample for the X100-2A steel plate surface, at a magnification of 50,000X. There is mainly a lath structure. For selected areas, a twinned martensite microstructure is observed (Figure 4-9). Figure 4-9 shows a BF and a dark field (DF) image of a representative packet of twinned martensite. The corresponding SAD pattern and its simulation are presented in Figure 4-9 (C). The twins are marked in Figure 4-9 (A) by an arrow. The twin reflections in the SAD pattern are marked by black rectangle and the matrix reflections by the blue rectangle in Figure 4-9 (C). The DF image of the twinned martensite was obtained using the reflection streak marked by the arrow in the SAD pattern (Figure 4-9 (C)). The formation of twinned martensite is generally related to carbon content and the twinned structure formed because of carbon partitioning between the ferrite and the austenite during the bainitic transformation. The twinned martensite formed when the carbon concentration in the austenite exceeds a certain critical value.[68]
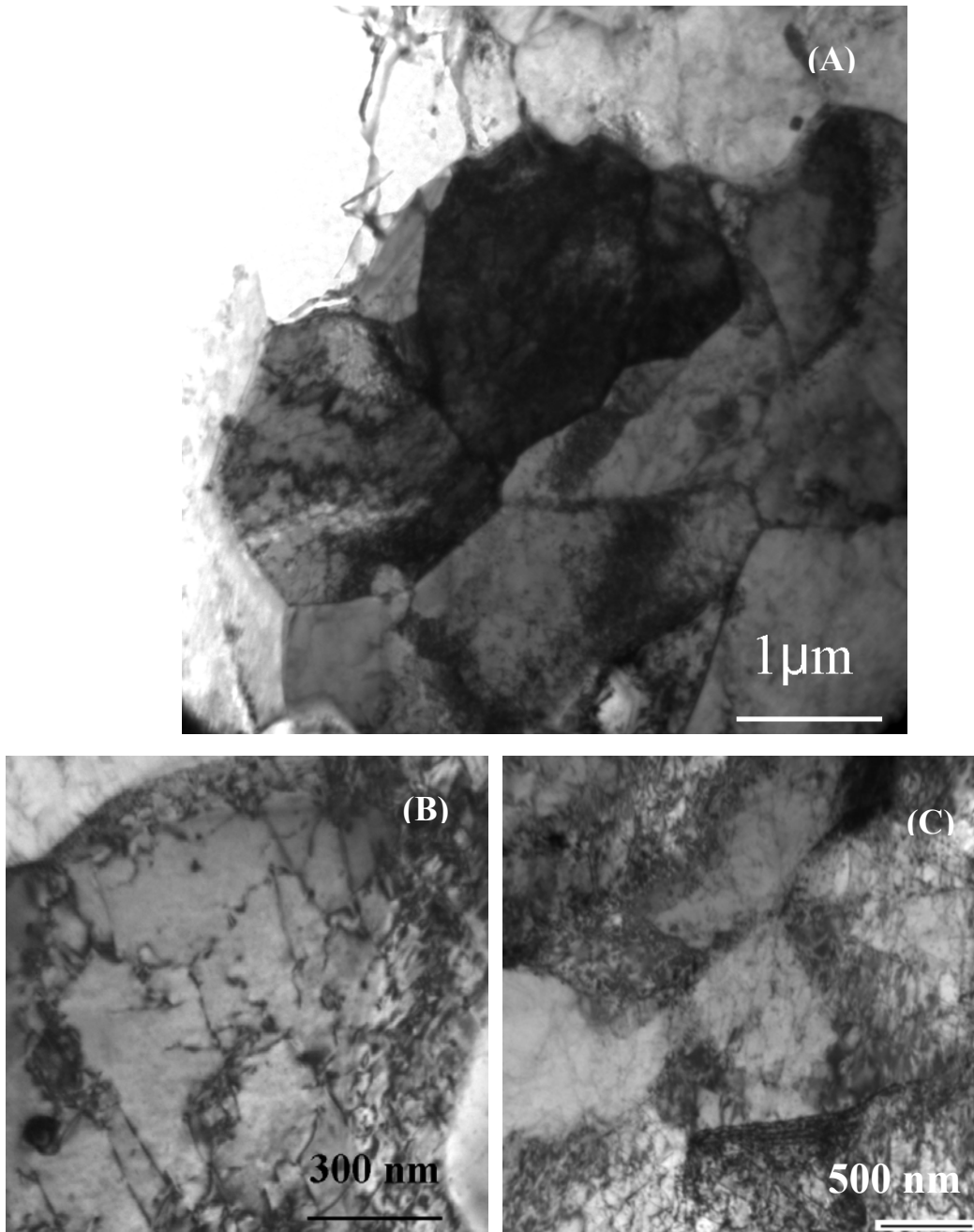
Figure 4-7 – (A) TEM BF image from a thin foil sample of the X80-462 steel pipe surface. (B) Microstructure at higher magnification. (C) Dislocation network.
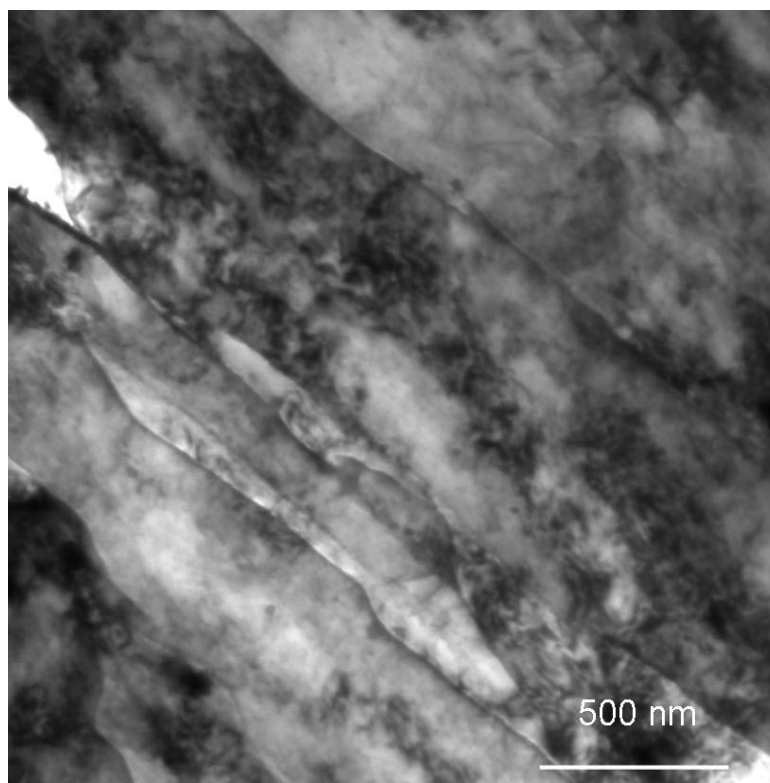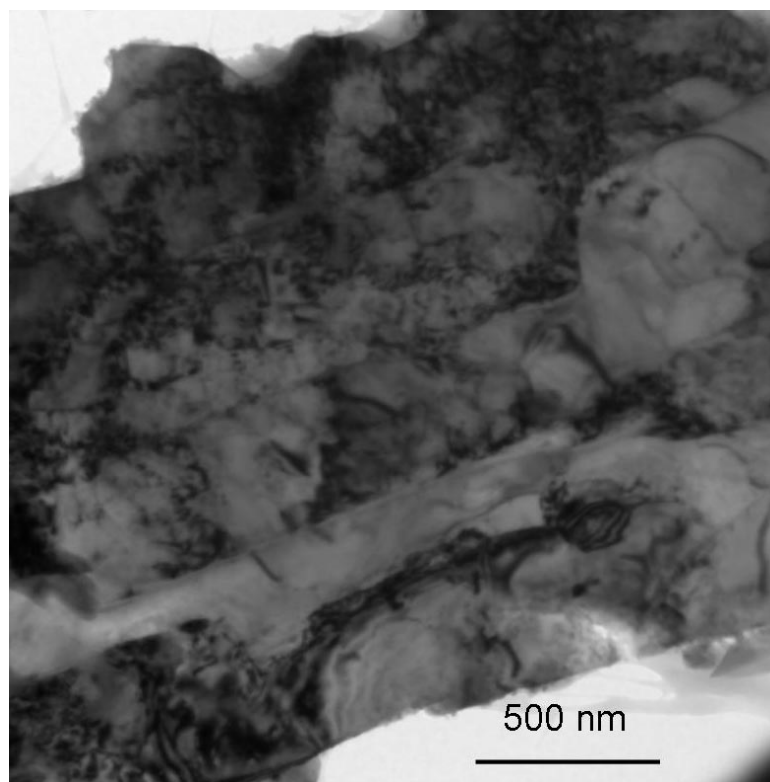
Figure 4-8 – Two TEM BF images from a thin foil sample of the X100-2A steel plate surface.
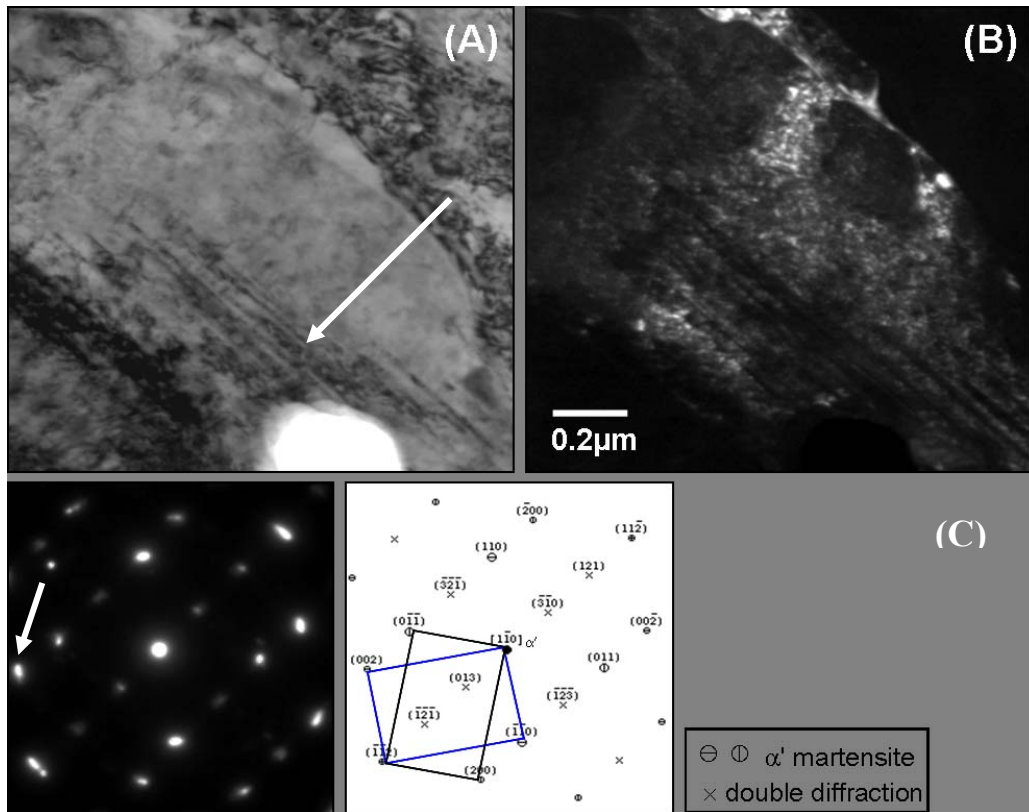
Figure 4-9 - (A) Twinned martensite. (B) DF image of martensite obtained with (002) reflection. (C) Corresponding SAD pattern and its simulation reveal the following orientation relationship for the two twin variants: $(112)\alpha''//(211)\alpha'T$; $[110]\alpha''//[011]\alpha'T$.

4.4.3 Subgrain size analysis by EBSD

EBSD was used to study the subgrain size change through thickness for steel X80-462. One of the most widely cited ASTM standards, i.e., E 112, for grain size measurement, was applied in this work. A mean linear intercept method is used to determine the subgrain size. An area, 20 μm^2, was included for each sample and 20 random lines were drawn for each. The number of grain boundaries intercepted by each line was counted. The intercept length over this quantity provided an estimate of the subgrain size. The standard deviation gave an indication of the degree of the mixed nature of subgrain sizes. Subgrain size was measured for all boundaries with a misorientation greater than 1º. Misorientations lower than 1º were disregarded, due to the angular resolution of 1º for EBSD.

Figure 4-10 is the EBSD map for X80-462 steel, obtained at normalized thickness position 0. Lines in different colors in this image represent different misorientations for boundaries. Generally, a misorientation of angle 15º separates a high angle grain boundary from a low angle grain boundary.[69] Red and pink lines represent high angle grain boundaries (>15º) and other lines represent low angle boundaries (<15º), which were dominated by green lines, i.e., misorientations between 1º and 2º.

=5 µm; Map3; Step=0.025 µm; Grid800x800
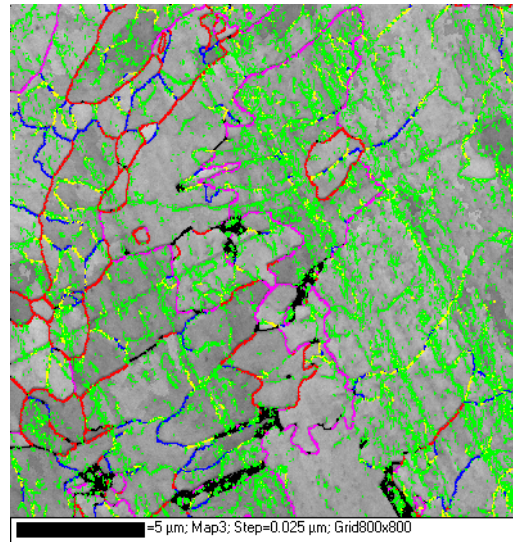
Figure 4-10 – EBSD map for X80-462 steel obtained at normalized thickness position 0. Green, yellow, blue, red and pink represent misorientations of grain boundaries in the range of, 1º-2º, 2º-5º, 5º-15º, 15º-50º and higher than 50º respectively.

Figure 4-11 shows two examples of intercept lines, obtained from the EBSD map shown by Figure 4-10. In these figures, indicated by arrows, within two high angle grain boundaries (>15º), there are several small angle grain boundaries, which clearly show the substructure within one large grain.

Table 4-15 summarizes the subgrain size at three different locations through thickness for steel X80-462. The subgrain size at the center is the coarsest. The subgrain size obtained at the outer surface is slightly smaller than that obtained at the inner surface.
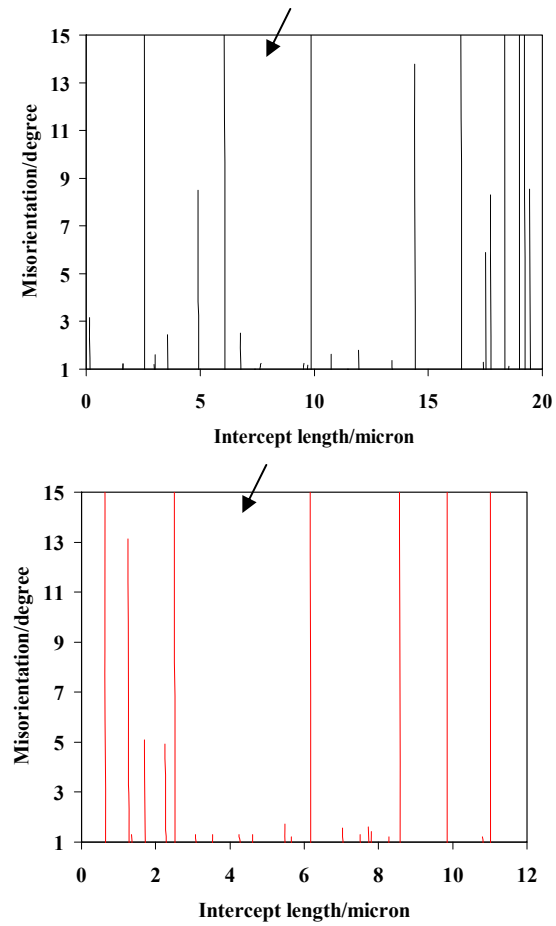
Figure 4-11- Misorientation vs. intercept length, showing higher angle boundaries
(>15º) and low angle boundaries (<15º).

Table 4-15– Subgrain size as an average intercept length for steel X80-462

Normalized position	Subgrain size (nm)	Standard deviation (nm)
0	388	41
5/10	471	30
1	324	32

4.5 WDS Analysis

WDS analysis was undertaken to study chemical variations through the pipe or plate thickness. WDS was chosen over energy dispersive X-ray spectroscopy (EDX) because of its better accuracy, precision and detection limit. Kuisma-Kursula conducted a comprehensive study, in which the accuracy of measurements of various elements by WDS was examined using a standard material with known chemistry. It was found that the error bars were mostly within 0.05 wt%.[74]

In this study, only results for Mn, Cr, Si, Mo and Ni compositions are included, since the composition of the other alloying elements is too low. Results for steel X80-462 are presented here, including compositions for Mn (Figure 4-12), Cr and Si (Figure 4-13) and Mo and Ni (Figure 4-14) through the pipe thickness. The dots in the diagram represent the experimental data and the solid lines correspond to the nominal concentration provided by Evraz Inc. NA. As shown in the figures, there is some scatter of the data, but no evident trend for composition variation was found through the thickness.

WDS results for the other four steels are included in Appendix C, and figure numbers are listed in Table 4-16. Generally, composition trend through the thickness was observed for the five steels studied, except for Si in X80-A4B. A lower Si composition was observed at the center of the pipe in compared with the surface (Figure A-42).

The Si and Mo compositions for two of the steels studied (X80-A4B and X80-B4F) show some differences compared with the nominal values. This is likely a sampling phenomenon, as sample sizes were small relative to the size of the steel.
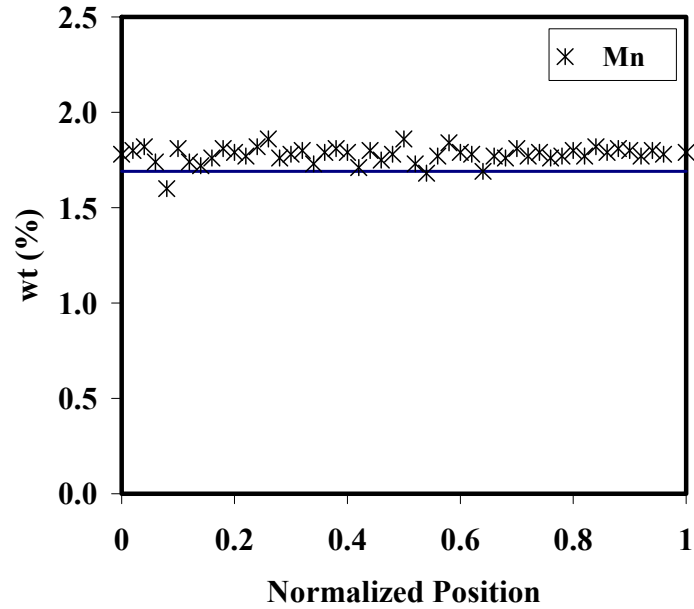
Figure 4-12 – WDS analysis for X80-462 showing Mn wt% as a function of pipe thickness. The solid line corresponds to the nominal concentration provided by Evraz Inc. NA.
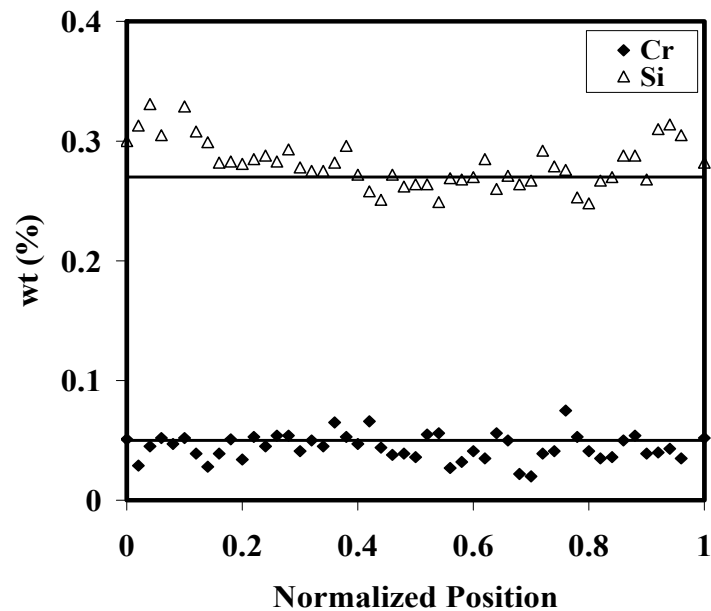
Figure 4-13 - WDS analysis for X80-462 showing Cr wt% and Si wt% as a function of pipe thickness. The solid line corresponds to the nominal concentration provided by Evraz Inc. NA.
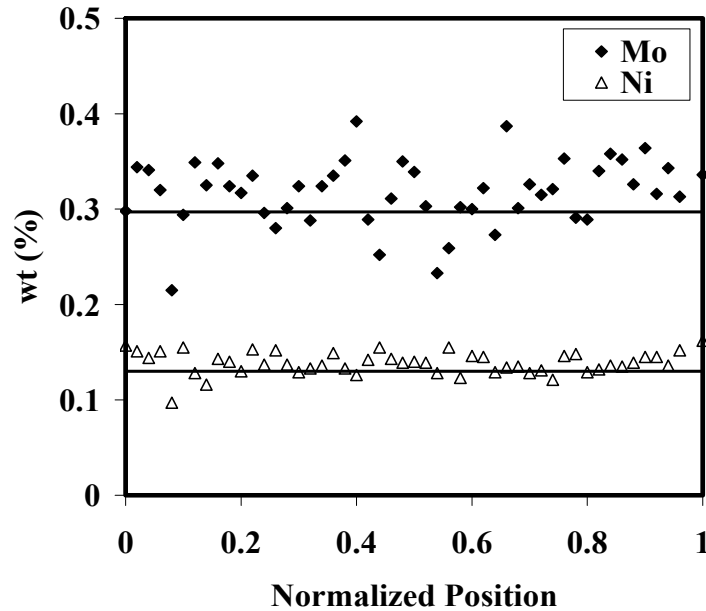
Figure 4-14 - WDS analysis for X80-462 showing Mo wt% and Ni wt% as a function of pipe thickness. The solid line corresponds to the nominal concentration provided by Evraz Inc. NA

Table 4-16 – Figure number of WDS analysis for alloying elements for four steels in the Appendix

Steels	Mn wt%	Cr wt%, Si wt%	Mo wt%, Ni wt%
X80-A4B	C-1	C-2	C-3
X80-A4F	C-4	C-5	C-6
X80-B4F	C-7	C-8	C-9
X100-2A	C-10	C-11	C-12

4.6 Summary

The results of the microstructure analysis through thickness for seven steels, obtained using the Rietveld method and other microstructure characterization techniques, were summarized in this chapter. More detailed discussion will be done in the next chapter, focusing on the effects of both processing and chemistry on microstructure variations.

5. DISCUSSION

The previous chapter summarized the microstructural analysis through the pipe/plate thickness using quantitative XRD analysis for subgrain size, dislocation density, texture and retained austenite weight fraction for seven microalloyed steels. Two steels (X80-462 and X100-2A) were selected for TEM analysis. Overall morphology was studied using OM and SEM for seven steels. The results obtained from these techniques show some microstructural variations either through the thickness or among the different steels.

This chapter is focused on determining the corresponding reasons for the microstructural change. Firstly, the microstructural features, i.e., subgrain size, dislocation density, texture index and retained austenite phase fraction as a function of pipe/plate thickness are discussed. Secondly, comparisons of the microstructural features are made among the different steels at both the surface and at the center of the strip. The microstructural changes for the different steels are explained in terms of variations in processing histories, i.e., CT and CR, alloying element concentrations and grain structure. Finally, a brief discussion of the relationship between microstructure and mechanical properties is given to provide an understanding of the mechanical property improvement for X100 steels in comparison with X80 steels.

5.1 Verification of Rietveld method data

The Rietveld method, which was developed in 1967, is a relative new technique compared with other microstructure characterization techniques, such as OM, SEM, TEM or EBSD. This study was the first time that the Rietveld method was applied to study the microstructure of microalloyed steels. Studies in the literature so far have shown that the Rietveld method is a powerful technique for determining a range of physical and chemical characteristics of materials. However, in comparison to other analysis techniques, such as TEM and SEM, which provide visual observation, the Rietveld method is an indirect method, so it is necessary to verify the data obtained from the Rietveld method using other characterization techniques. In this study, TEM and EBSD were conducted to verify the subgrain size measurements obtained by the Rietveld method for the X80-462 steel.

For the X80-462 steel, a thin foil sample was taken from the pipe inner surface for TEM study. This corresponds to the normalized position 0 for XRD analysis. A total of 63 domains were counted and the average value was 500 nm. According to the XRD data shown in Table 4-6, at normalized position 0, the subgrain size output from the Rietveld method is 303 nm. The difference may be due to the limited area analyzed by TEM. In the Rietveld method. the subgrain size is based on peak broadening and may be more sensitive to low angle misorientation giving a relatively smaller subgrain size.

EBSD analysis was conducted to study the subgrain size variation through thickness for X80-462 steel. Three samples were done. The subgrain size results are shown by Table 4-15. Figure 5-1 shows a comparison of subgrain sizes at three different locations through thickness for steel X80-462, obtained by EBSD and XRD. Generally, there are some differences in absolute values of subgrain size at all three locations. The difference in subgrain size is believed to be due to the different sensitivities for misorientation for EBSD and XRD. As described in section 4.4.3, subgrain size measured by EBSD disregarded misorientations lower than 1°; however, the sensitivity of Rietveld refinement to misorientation, is

unknown. In addition, the EBSD sampling volume was small relative to that for XRD. These factors may result in differences in subgrain size.

The variations in subgrain size as a function of location through thickness show the same trend for both methods. As shown in Figure 5-1, the subgrain sizes, obtained by both XRD and EBSD, are coarsest at the center. Subgrain sizes at the outer surface are finer than those at the inner surface.
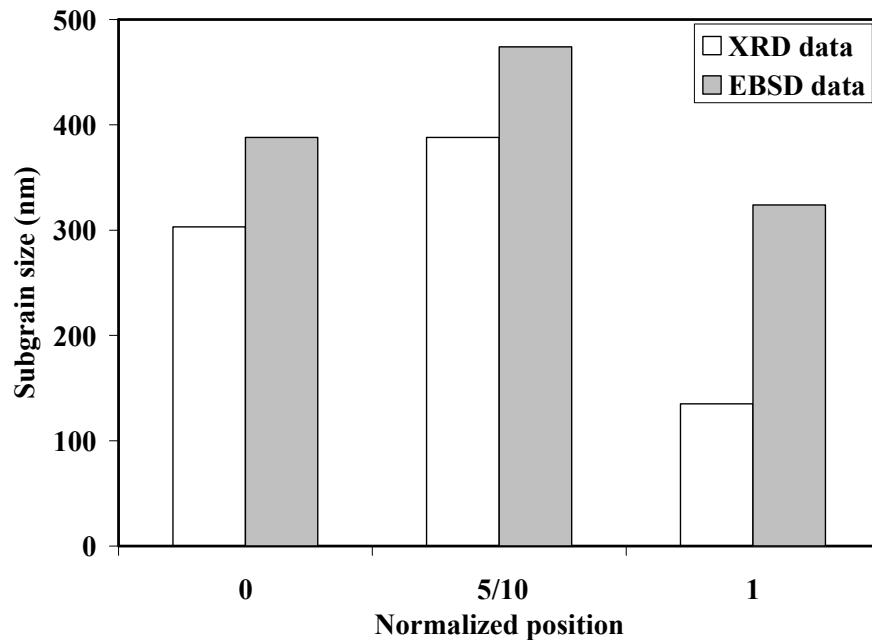
Figure 5-1– Subgrain size comparison obtained by EBSD and XRD for X80-462 steel. 0 and 1 represent the inner and outer surfaces.

5.2. Microstructure change through the thickness

In this section, the microstructural features, obtained from the Rietveld method, including subgrain size, dislocation density, texture index and retained austenite phase weight fraction, are plotted as a function of thickness for each steel. The variations in the microstructural features are mainly due to processing differences at the different locations through the thickness.

5.2.1 X80 Steels

5.2.1.1 Subgrain size and dislocation density

The subgrain sizes for two X80 steels (X80-462 and X80-A4B) measured as a function of relative location in the steel plates (where 0 and 1 represent the surfaces) are shown in Figure 5-2. Note that refined grain and subgrain sizes are both combined and reported as one parameter in Rietveld refinement. In general, the subgrain sizes are less than 500 nm. For both steels, generally the subgrains on the surface are finer than at other locations through the thickness, as shown in Figure 5-2. The middle of the pipe has been marked by a vertical dashed line in the diagrams.

The variation in subgrain size through the thickness may be due to chemistry and/or processing parameter differences. According to the WDS results presented in the previous chapter, in general there are no trends regarding chemistry variation through the thickness, so the effect from the chemistry on the variation in microstructure can be discounted. For TMCP, variations in microstructure could occur possibly due to differences in the extent of deformation, deformation temperature and CR between the surface and centre of the strip. It is difficult to quantify the processing parameter differences as a function of relative location through the thickness; however, it is a fact that the CR at the interior of the strip is lower than that at the surface. The accelerated cooling process further increases this difference in CR through the thickness.[5]

Subgrain size is observed to be finer at the pipe surface than at the center, as shown in Figure 5-2, which is likely due to the higher CR at the surface.

However, how the CR affects the subgrain size, obtained by the Rietveld method, has not been discussed in the literature.

As mentioned in Chapter 2, deformation in two phase areas is crucial for substructure generation. Deformation in the austenite-ferrite region allows deformation bands to continue to form in the austenite phase and the deformed ferrite produces a substructure. Higher deformation occurs near the strip surface, due to direct contact with the rollers, which results in a finer substructure than that in the center of the strip. The higher cooling rate at the surface also more effectively prevents the growth of subgrains. In addition, accelerated cooling results in a decrease in the austenite to ferrite transformation temperature and, consequently, causes an increase in the extent of undercooling, so ferrite or other phase nucleation rates are enhanced. The rapid cooling allows for the formation of very fine grain sizes by increasing the nucleation rate and preventing grain growth, as shown in Figure 5-2. Higher cooling rates at the surface result in finer grain size than that in the center of the strip.

There is some variation in subgrain size obtained at both surfaces, which could be due to different cooling conditions at the surfaces. Water is sprayed on both surfaces; however, water sprayed on the bottom surface will fall away because of gravity effects. The water on the top surface may form a warm water film, which will block contact between fresh water and the strip surface. For steel X80-462, which was up coiled, the top surface corresponds to the inner surface of the pipe. For steel X80-A4B, which was down coiled, the top surface corresponds to the outer surface of the pipe. Therefore, as shown by Figure 5-2, the top surface has a finer subgrain size for steel X80-A4B and the bottom surface has a finer grain size for steel X80-462. As such, the different cooling conditions at the surfaces did not contribute to the variation in subgrain size between two surfaces. The subgrain size difference between the two pipe surfaces may, instead, be due to deformation variations between the inner and outer surfaces in the process of pipe forming. A numerical model needs to be developed to confirm both cooling rate and deformation variations through thickness, in order to quantitatively interpret subgrain size variation.
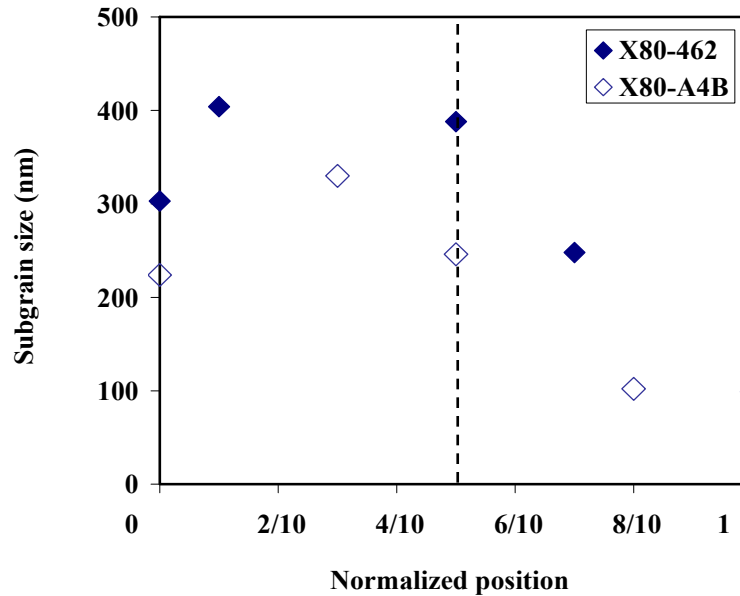
Figure 5-2 – Subgrain size vs. normalized position for X80 steels
(X80-462 and X80-A4B).

The subgrain sizes for the other two X80 steels (X80-A4F and X80-B4F), measured as a function of relative location in the steel plates (where 0 and 1 represent the surfaces) are shown in Figure 5-3. In general, the subgrain size values are between 100 nm and 200 nm. There is no significant variation in subgrain size for these two X80 steels through the thickness. The 59 nm subgrain size, at the 3/10 position for X80-A4F, is much finer than that at other positions. Two additional samples from the same position were prepared and analyzed by XRD. The subgrain sizes output from the Rietveld method were 52 nm and 56 nm, respectively, which are virtually as the value from the first result. As such the subgrain size at this position is not an artifact. From the processing information provided by Evraz Inc. NA, the reason for the finer subgrain size at this position is unknown at this time and further study is needed.
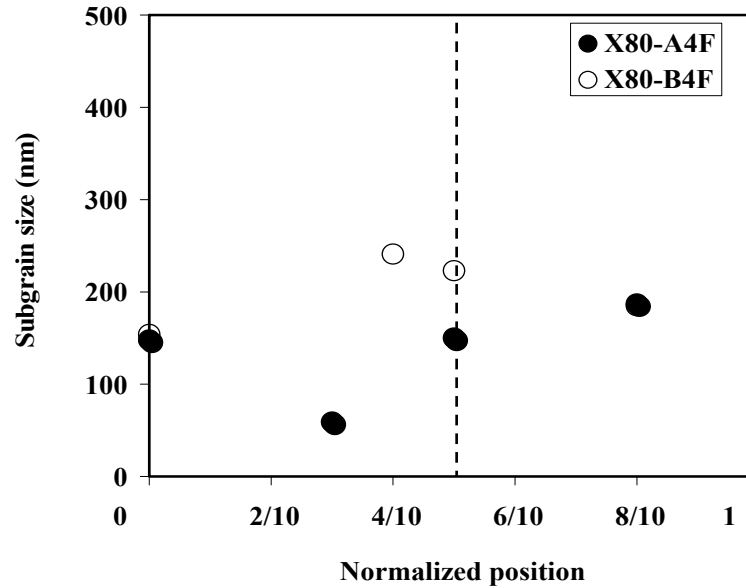
Figure 5-3 - Subgrain size vs. normalized position for X80 steels
(X80-A4F and X80-B4F).

Figure 5-4 shows the dislocation density variation as a function of relative location through thickness for the X80-462 and X80-A4B steels (where 0 and 1 represent the surfaces). The variations in dislocation density through thickness for the two X80 steels (X80-462, X80-A4B) show a similar trend, which is that a higher dislocation density is observed at the surface compared with that at the center of the strip. In particular, the dislocation density at the outer surface changes more significantly compared with interior of the pipe than that at the inner surface.

The difference in dislocation density through thickness is not as evident as that of subgrain size. The dislocation is calculated using equations 2-10, 2-11 and 2-12, so that dislocation density is indirectly measured from subgrain size and microstrain. Since the microstrain values did not show variation through thickness (see Appendix A Tables A-8 and A-9), the variation in dislocation density is mainly due to subgrain size change. The variation is not as significant as that of subgrain size, due to the low sensitivity of the model used to calculate the dislocation density.

According to the WDS analysis, which shows no variation in chemistry through the thickness, the effect of chemistry on dislocation density is negligible. The higher dislocation density at the surface, shown in Figure 5-4, may be due to the higher CR at the pipe surfaces, which increases the chances for displacive phase transformations, such as acicular ferrite and/or bainitic formation. From the CCT curve shown in Figure 2-8, bainitic ferrite and acicular ferrite are obtained through faster cooling rates, while polygonal ferrite forms at lower cooling rates. Bainitic ferrite and/or acicular ferrite phase have higher dislocation densities in comparison with polygonal ferrite.[27] The difference in dislocation density at both surfaces is speculated to be due to the same reason discussed in subgrain size section, i.e., different cooling conditions.
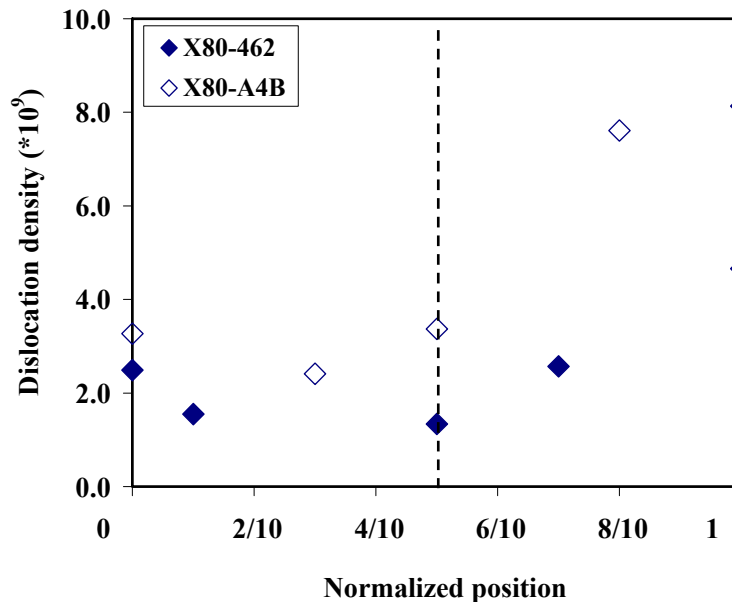
Figure 5-4 – Dislocation density vs. normalized position for X80 steels
(X80-462 and X80-A4B).

Figure 5-5 shows the dislocation density as a function of relative location in the steel plate for X80-A4F and X80-B4F steels (where 0 and 1 represent the surfaces). Generally, the dislocation density does not change significantly through the thickness for these two X80 steels. This result is similar to the subgrain size

variation results. There is one location (normalized position 3/10) for steel X80-A4F, with a dislocation density significantly higher than the values at other locations. As mentioned in Section 5.2.1.1, two more samples at the same position, then have been analyzed by Rietveld method, and similar subgrain sizes (52 nm and 56 nm relative to 59 nm) and consequently similar dislocation density have been obtained. Except for this point in Figure 5-5, the dislocation density is approximately constant through the thickness for both steels.
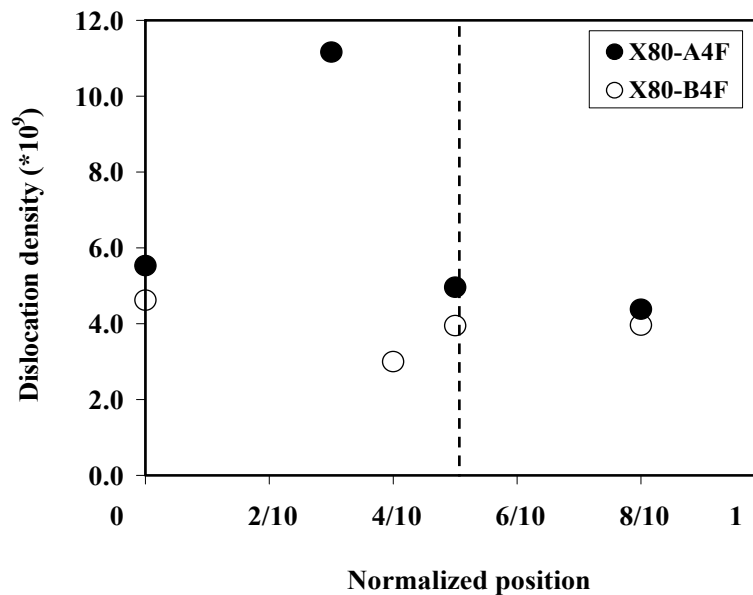
Figure 5-5 - Dislocation density vs. normalized position for X80 steels (X80-A4F and X80-B4F).

As described above, the variations in subgrain size and dislocation density through thickness show some differences for the four X80 steels. In terms of processing parameters and chemistry, there are some differences as well. The main chemistry variations are in terms of Ni and Mo compositions. Table 5-1 lists the average subgrain size, average dislocation density, FRT, CT, ΔT, thickness and Ni and Mo contents for the four X80 steels. ΔT is the temperature difference between the FRT and CT. The FRT and CR are normalized relative to the actual values for the X100-2A steel. Subgrain size and dislocation density were averaged through the thickness for each steel.

Table 5-1– Comparison of the microstructure, processing parameters and chemistry for four X80 steels

Steel	Average Subgrain Size (nm)	Average ρ_{disl} ($\times 10^9$) (cm/cm^3)	FRT	CT	ΔT (°C)	Thickness (mm)	Ni wt%	Mo wt%
X80-462	296	2.5	0.94	1.47	156	11.8	0.13	0.297
X80-A4B	200	5.0	1.05	1.32	302	12.1	0.25	0.305
X80-A4F	137	6.2	1.00	1.28	278	15.6	0.41	0.404
X80-B4F	201	3.8	1.00	1.42	222	15.1	0.41	0.299

Overall, X80-A4F steel has the finest subgrain size and highest dislocation density, while X80-462 has the largest subgrains and lowest dislocation density. The microstructural features for X80-A4B and X80-B4F steels are intermediate. X80-A4B steel shows a higher dislocation density in comparison with X80-B4F.

X80-A4F steel, with the smallest subgrain size and highest dislocation density, has second highest FRT (1.00), lowest CT (1.28) and second largest ΔT (278 °C), which means it has the second longest accelerated cooling process. Second longest accelerated cooling process and lowest CT result in finer structure. X80-A4F also has the highest Ni and Mo concentrations, both of which increase the hardenability and promote the formation of bainitic ferrite or acicular ferrite by shifting the CCT diagram to longer times. Bainitic ferrite and acicular ferrite have finer substructures and higher dislocation densities than polygonal ferrite.[70] The combination of high alloying element content, e.g., Ni and Mo, the second longest accelerated cooling process and the lowest CT lead to the finest subgrains and highest dislocation density for X80-A4F steel among the four X80 steels.

X80-462 has the largest subgrains and lowest dislocation density. In terms of processing, it has the lowest FRT (0.94), highest CT (1.47) and smallest ΔT (156°C). In terms of chemistry, it has lowest combined amount of Ni and Mo. The combination of the shortest accelerated cooling process and lowest Ni and Mo contents results in the most coarsened microstructure. Also as discussed in the Chapter 2, a lower FRT is helpful for structure refinement; however, the

temperature should be higher than the austenite to ferrite transformation temperature. For X80-462, the actual FRT is close to 750°C, which may be lower than the austenite to ferrite transformation temperature. The ferrite formed before the accelerated cooling process coarsens at such high temperatures, producing a coarse structure for X80-462. In addition, a high CT is more likely to result in a coarser microstructure during strip cooling to room temperature after coiling.

X80-A4B has intermediate values of subgrain size and dislocation density. It has the highest FRT (1.05), second lowest CT (1.32) and largest ΔT (302°C). In terms of chemistry, it has intermediate levels of Ni and Mo (Table 5-1). Chemistry (e.g., Ni and Mo) appears to dominate over processing, since this steel has an intermediate subgrain size and dislocation density, although it has the longest accelerated cooling process. The subgrain size and dislocation density for X80-B4F are also intermediate, and X80-B4F has intermediate FRT (1.00), second highest CT (1.42) and second smallest ΔT (222 °C). In terms of chemistry, X80-B4F has the highest Ni content and intermediate Mo content. Compared with X80-B4F, X80-A4B has higher dislocation density, which is believed to be due to the longer accelerated cooling process.

The four X80 steels the variations in subgrain size and dislocation density through thickness also show different trends.

X80-462 and X80-A4B steels (first group) have similar trends in terms of subgrain size and dislocation density changes through thickness, i.e., the subgrain size is finer at the surfaces than at the center (Figure 5-2) and dislocation density is lower at the center compared to the surfaces (Figure 5-4). X80-A4F and X80-B4F (second group) show similar trends in terms of subgrain size and dislocation density changes through thickness. For both steels, there was little variation through thickness for both subgrain size and dislocation density (Figure 5-3 and Figure 5-5). Generally, the trends for subgrain size (Figure 5-2 and Figure 5-3) and dislocation density (Figure 5-4 and Figure 5-5) are essentially opposite. This is not surprising, since the dislocation density value is calculated using the values for subgrain size and microstrain (Equations 2-9, 2-10 and 2-11). As shown in

Table 4-6, Table 4-7, Table 4-8 and Table 4-9, the microstrain values change slightly through the thickness for all X80 steels, and the variation is within 1%, so the difference in dislocation density variation through the thickness is mainly due to the variation in subgrain size.

The changes in microstructure, as a function of the thickness, do not appear to be affected by the processing conditions; see, for example, X80-462 and X80-A4B, in Table 5-1. Both steels have larger subgrain sizes at the center compared with the surfaces, but X80-462 had the lowest FRT and ΔT, while X80-A4B had highest FRT and ΔT. However, the X80-A4F and X80-B4F samples are from thicker pipes, approximately 15 mm, compared with the other two X80 steel samples (X80-462 and X80-A4B), which are about 12 mm thick. Thicker pipe are expected to have more variations in temperature and strain through thickness than thinner pipe and, consequently, more variation in microstructure. However, the results in this study show opposite trends, i.e., more variation in microstructure change through thickness for thinner pipes. Further study is needed.

5.2.1.2 Texture index

As described in Chapter 2, texture index represents the strength of texture in a sample. A texture index of 1 corresponds to a randomly oriented sample and a higher texture index corresponds to stronger texture in the sample, e.g., 1.2 as discussed previously. The texture index for X80-462 and X80-A4B steels, measured as a function of relative location in the steel plates, (where 0 and 1 represent the surfaces) is shown in Figure 5-6. In general, the texture indices are close to 1.1 with no significant difference in texture index through the pipe thickness. At normalized position 1/2 for X80-A4B steel, the texture index shows a higher value than at other positions.
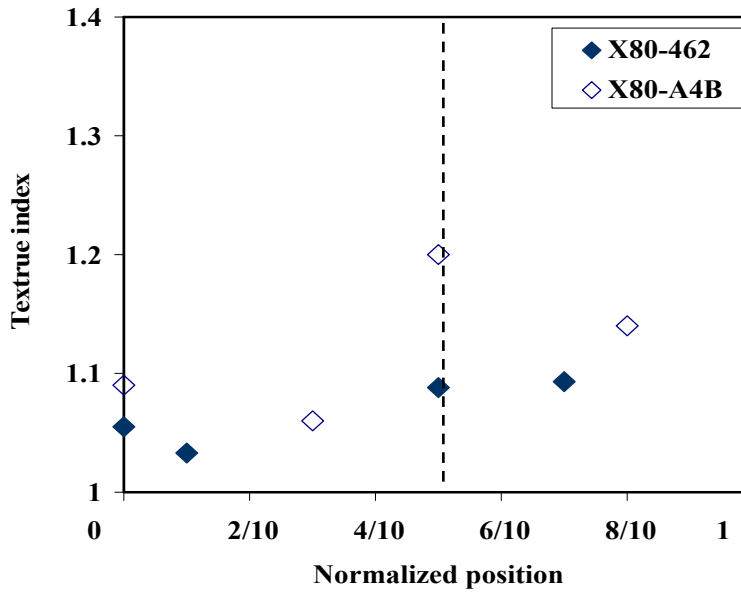
Figure 5-6 – Texture index vs. normalized position for X80 steels
(X80-462 and X80-A4B).

The texture index for X80-A4F and X80-B4F steels, measured as a function of relative location in the steel plates (where 0 and 1 represent the surfaces) is shown in Figure 5-7. Stronger texture (in excess of 1.2) was observed at locations near the centerline (marked by the vertical dashed line) compared with the pipe/plate surfaces. As discussed before, a texture index of 1.2 represents relatively strong texture in microalloyed steels. At pipe surfaces, nearly no texture was observed, with texture indices close to 1.
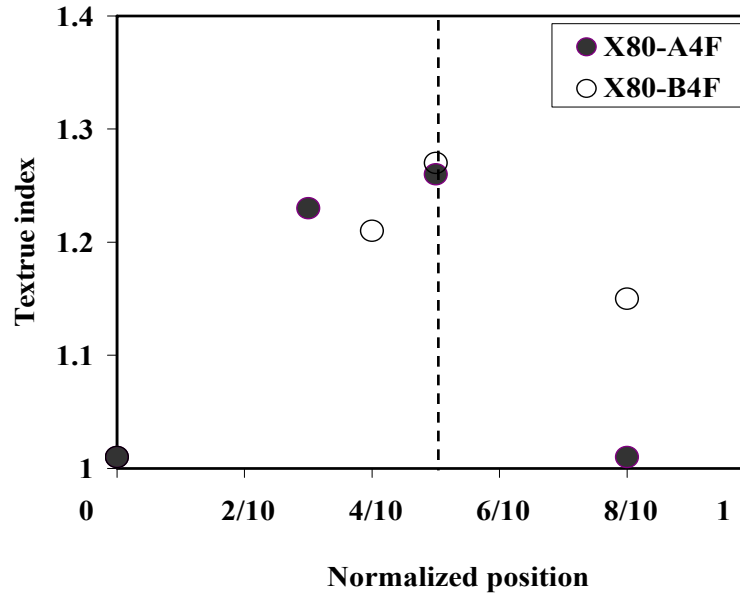
Figure 5-7 – Texture index vs. normalized position for X80 steels
(X80-A4F and X80-B4F).

In the previous discussion, there is an assumption that the deformation is uniformly distributed through the thickness; however, this cannot be the case since there are different hot rolling temperatures and different deformation rates through strip thickness. There are non-negligible differences in strain through the pipe/plate thickness. The differences in strain and strain rate could result in variations in austenite recrystallization rates and also the extent of deformation. Therefore, lower texture at the surface may be a consequence of more static recrystallization for prior austenite grains at the pipe surfaces, producing more equaxied grains at the pipe surfaces and more elongated grains at the centerline. Consequently, the elongated grains will have stronger texture compared with the equaxied grains at the pipe surfaces.

However, the above is speculation, investigation of the types of texture and corresponding intensity need to be made before coming to any conclusions and corresponding reasons.

5.2.1.3 Retained austenite

The amount of retained austenite, as a function of relative location in the steel plates (where 0 and 1 represent the surfaces), for X80-462 and X80-A4B steels is shown in Figure 5-8. The amount of retained austenite for X80-462 steel is below the sensitivity of XRD; i.e., no austenite peaks were observed. X80-A4B steel overall has a low amount of retained austenite, with the highest amount near 2% at the centerline (marked by the vertical dashed line in the Figure 5-8).

Figure 5-9 shows the measured amount of retained austenite as a function of relative location in the steel plates for X80-A4F and X80-B4F steels. The amounts of retained austenite at the centerline for two X80 samples were approximately 7%. More retained austenite was always obtained at positions near the centerline relative to the pipe/plate surfaces.

Retained austenite is substantially enriched in carbon and partitioned into small rectangular blocks by the ferrite transformation. The carbon concentration has a great effect on the retained austenite phase weight fraction.

The amount of the retained austenite, which is found to linearly increase with decreasing martensite transformation start temperature, M_s, is controlled by various parameters, especially chemistry.[71,72] Most of the alloying elements have a significant effect on M_s,[73] as shown by equation 5-1.

$$M_S = 500 - 333C - 34Mn - 35V - 20Cr - 17Ni - 11Mo - 10Cu - 5W - 15CO + 30Al$$

$$(5-1)$$

where the alloying element amounts are given in weight percent. A lower M_s results in less martensite before reaching room temperature, and consequently more austenite is retained.

As shown in Figure 5-8 and Figure 5-9, a higher retained austenite weight fraction was obtained at the center of the strip. More alloying elements are generally present near the centerline, due to segregation although this was not shown by the WDS results. The detection limit of WDS ordinarily varies between 0.03 and 0.05 wt%. The accuracy depends on the type of the element and

decreases with decreasing content of the element. The amount of Mo and Ni in these steels is in the 0.3-0.4 wt% range. For this composition range, the accuracy in WDS measurements is 10-20%. Segregation effects should have been detectable by WDS, but as mentioned above were not. Carbon has by far the greatest effect on M_s (Equation 5-1); however, the accuracy in WDS measurements is even worse, i.e., 150%-200% for the C contents in these steels.[74] As such, C levels were not measured by WDS. There are likely C segregation effects, but these were not confirmed by WDS.
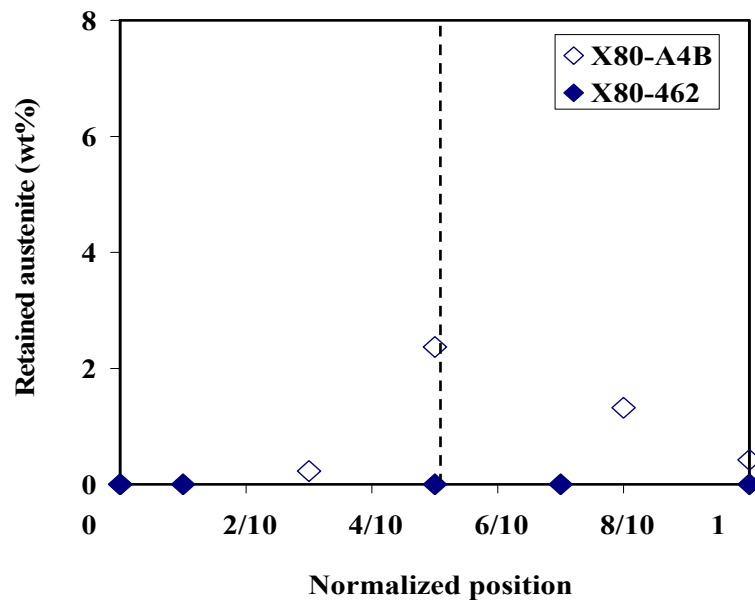

Figure 5-8 – Retained austenite phase wt% vs. normalized position
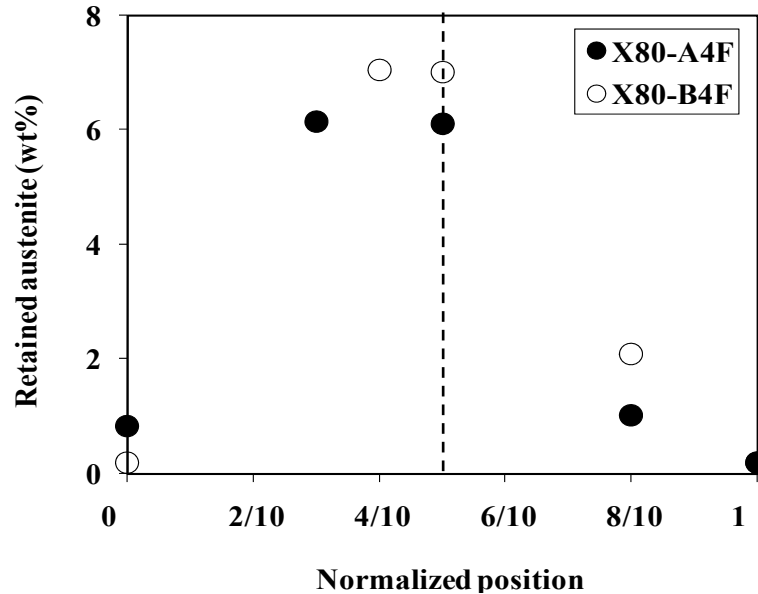for X80 steels (X80-462 and X80-A4B).

Figure 5-9- Retained austenite phase wt% vs. normalized position
for X80 steels (X80-A4F and X80-B4F).

Generally, higher amounts of retained austenite were obtained at the center of the strip relative to the surfaces for three X80 steels, except X80-462 which had no retained austenite at any position. However, X80-A4F and X80-B4F show more retained austenite relative to X80-A4B. The reasons for the differences will be discussed in Section, 5.3.1.

5.2.1.4 Summary

According to the analysis discussed above, the four X80 steels show two different trends for the variations in microstructural features through the pipe thickness, specifically subgrain size, dislocation density, texture index and amount of retained austenite.

For X80-462 and X80-A4B steels, which are thin pipes, the maximum dislocation densities and finest subgrain sizes were observed at the pipe surface. Generally, these two X80 steels have a low overall texture index and low amounts of retained austenite.

For X80-A4F and X80-B4F steels, which are thick pipes, both subgrain size and dislocation density do not show significant variation through the thickness.

Texture index and the amount of retained austenite phase are higher at the center of the strip compared with the surfaces.

5.2.2 X100 steels

5.2.2.1 Subgrain size

The subgrain sizes for the three X100 steels (X100-2A, X100-2B and X100-3C), measured as a function of relative location in the steel plates (where 0 and 1 represent the surfaces), are shown in Figure 5-10. In general, the subgrain sizes are less than 100 nm; The exception is X100-3C steel at the normalized position of 3/10. There is no significant variation through thickness for all three X100 steels. This result may be due to more uniform processing for the X100 steels (experimental steels) through the thickness, compared with processing for the X80 steels (industrial steels).
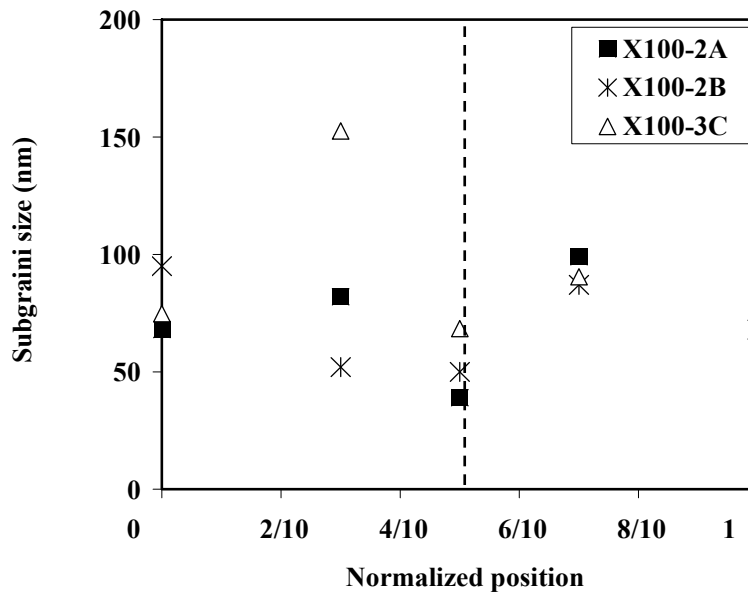
Figure 5-10 - Subgrain size vs. normalized position for X100 steels.

5.2.2.2 Dislocation density

The dislocation densities for the three X100 steels (X100-2A, X100-2B and X100-3C), measured as a function of relative location in the steel plates (where 0

and 1 represent the surfaces), are shown in Figure 5-11. The dislocation density is calculated using the values of subgrain size and microstrain, using equations 2-10, 2-11 and 2-12. As shown in Table 4-10, Table 4-11 and Table 4-12, the microstrain values for the three X100 steels did not show significant variations through the thickness. The dislocation density variation through the thickness is mainly due to the subgrain size change (Figure 5-10). In addition, the fine subgrain size values result in high dislocation densities and large variations in dislocation density. In general, there is no trend for dislocation density as a function of relative location through thickness.
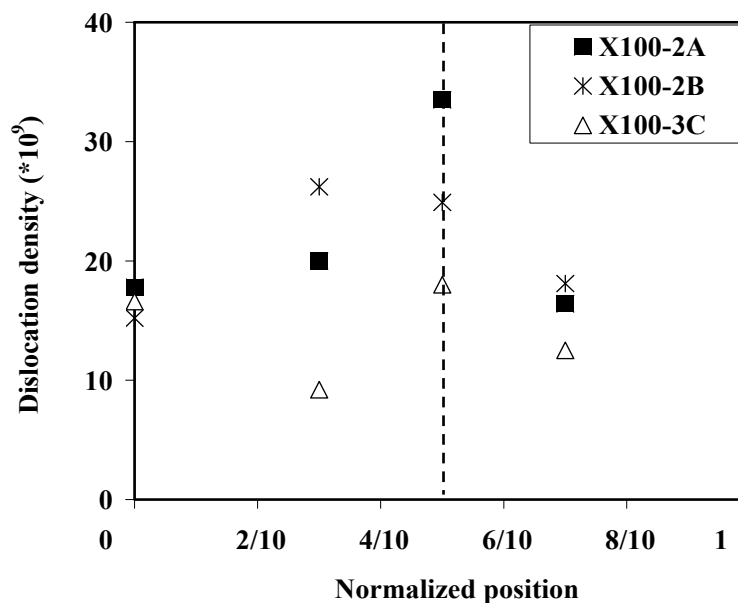
Figure 5-11 - Dislocation density vs. normalized position for X100 steels.

5.2.2.3 Texture index

The texture indices for the three X100 steels (X100-2A, X100-2B and X100-3C), measured as a function of relative location in the steel plates (where 0 and 1 represent the surfaces), are shown in Figure 5-12. A higher texture index is obtained at the centerline, likely for the same reason described for the texture change in X80 steels. Higher deformation in the surface region and a greater chance for the prior austenite to recrystallize, leads to more equiaxed and regularly shaped prior austenite. In comparison, prior austenite grains near the

centerline are elongated. Consequently, the grains have stronger texture near the centerline compared with the grains near the pipe surfaces.

Figure 5-12 – Texture index vs. Normalized position for X100 steels.

5.2.2.4 Retained austenite
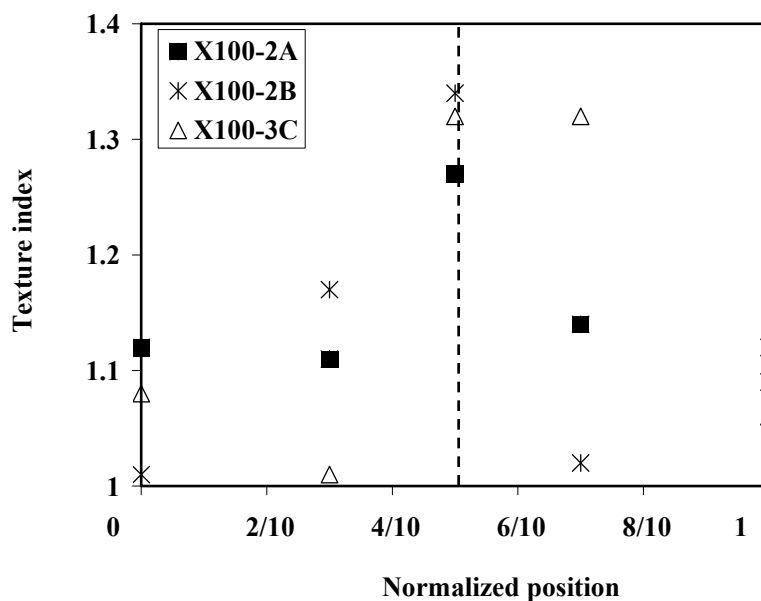
As shown in Table 4-10, Table 4-11 and Table 4-12, retained austenite was only detected for the X100-3C steel, with a maximum of 1.77%. This may be related to the higher CR for the X100 steels compared with the X80 steels. It is expected that more martensite will form in the X100 steels with less retained austenite. A detailed discussion of the amount of retained austenite for the seven steels is given in the next section.

5.2.2.5 Summary

For the X100 steels, there is no significant variation in subgrain size through thickness and no general trend for dislocation density as a function of thickness. The texture index is higher at the center of the strip compared to the surface. The amount of retained austenite is generally below the sensitivity of the XRD techniques utilized.

For the three X100 steels, there are some differences in chemistry and processing parameters, as discussed in Section 3.1.2. However, the variations in subgrain size, dislocation density, texture and retained austenite through thickness did not show much difference. Microstructure comparisons for the seven steels, at the surface and center of the pipe, will be made in the next section.

5.3 Microstructural comparison for different steels

This section will focus on summarizing the microstructural features obtained from the surfaces and center of the strip for the different steels. Differences in microstructures are believed to be due to different processing histories, differences in chemistry and/or different grain structures. Therefore, in this section, the discussion is divided into the effects from processing, chemistry and grain structure.

5.3.1 Summary of microstructure features for different steels

Table 5-2 summarizes the average microstructural features obtained from the two surfaces for each steel, including subgrain size, microstrain, dislocation density and texture index values. Table 5-3 lists the microstructural features obtained at the center of the strip for the seven steels.

For the average microstructural features obtained at the surfaces, i.e., average values of both surfaces, there were no major differences among either the X80 or X100 steels (Table 5-2). However, there are significant differences in microstructural features for the X80 pipe steels versus the X100 plate steels. The X100 microalloyed steels have finer subgrains, higher microstrains and higher dislocation densities (ρ_{disl}). For the microstructural features at the center of the strip (Table 5-3), significant differences exist among the X80 steels, but not among the X100 steels. X80-462 has the coarsest subgrain size (388 nm) and lowest dislocation density (1.3×10^9 cm/cm^3) among the four X80 steels. X80-A4F has the finest subgrain size (150 nm) and highest dislocation density (5.0×10^9 cm/cm^3). The microstructural features obtained from the center of the strip

show larger differences overall than those obtained from the pipe/plate surfaces among the seven steels.

Table 5-2 - Microstructural features at the surfaces for X80 and X100 steels

Steel	Subgrain size (nm)	Microstrain (%)	ρ_{disl} $(\times 10^9)$ (cm/cm^3)	Texture index
X80-462	219	6.5	3.6	1.02
X80-A4B	162	7.3	5.7	1.11
X80-A4F	144	7.1	5.3	1.04
X80-B4F	178	6.7	4.1	1.01
X100-2A	75	12.0	17.2	1.12
X100-2B	82	14.3	19.3	1.05
X100-3C	85	12.1	15.3	1.07

Table 5-3 - Microstructural features at the center of the strip for X80 and X100 steels

Steel	Subgrain size (nm)	Microstrain (%)	ρ_{disl} $(\times 10^9)$ (cm/cm^3)	Texture index
X80-462	388	4.9	1.3	1.09
X80-A4B	246	7.8	3.4	1.20
X80-A4F	150	7.0	5.0	1.26
X80-B4F	223	8.3	4.0	1.27
X100-2A	39	12.3	33.5	1.27
X100-2B	50	11.7	24.9	1.34
X100-3C	68	11.5	18.0	1.32

Table 5-4 summarizes the highest texture index value for the ferrite phase from each steel and the corresponding normalized intensities for the four peaks. No significant variations were obtained for the highest texture index values, and there was strong texture for every steel except X80-462.

Table 5-4 - Highest texture index for X80 and X100 steels

Normalized position	Texture index (J)	Normalized intensity for the four peaks			
		I(110)	I(200)	I(211)	I(220)
X80-462	1.093	100	30.8	74.2	4.4
X80-A4B	1.200	100	41.7	128.9	4.6
X80-A4F	1.264	100	89.9	404.3	7.6
X80-B4F	1.265	100	67.9	296.3	5.2
X100-2A	1.267	100	56.3	273.3	7.4
X100-2B	1.336	100	71.3	417.3	7.8
X100-3C	1.274	100	114.3	591.3	3.9

Table 5-5 lists the maximum retained austenite phase weight fraction obtained from each steel, as well as the corresponding chemistry and some of the processing parameters. As discussed previously, the maximum amount of retained austenite is always obtained at the center of the strip. For two X80 steels (X80-A4F and X80-B4F), the amount of retained austenite exceeded 6 wt%. These two steels had high coiling temperatures; however, higher CT is not the only factor responsible for more retained austenite, since the other two X80 steels (X80-462 and X80-A4B) also had high coiling temperatures relative to the three X100 steels. The higher carbon content, as well as the extra Ni (an austenite stabilizer) for X80-A4F and X80-B4F relative to X80-462 and X80-A4B, likely contributed to the higher amounts of retained austenite. In fact, the X80-A4B steel contains more C than the X80-462 steel and has more Ni as well. Austenite retention is therefore strongly influenced by chemical composition and TMCP parameters.[21, 75, 76, 77, 78] In addition, more retained austenite is reported to be

obtained at lower finishing rolling temperatures, which was not observed in this study.[12]

The amount of retained austenite linearly increases with decreasing martensite transformation start temperature, M_s.[71,72] M_s is calculated using equation 5-1, and listed in Table 5-5. Steels X80-A4F and X80-B4F show relatively low M_s temperatures compared X80-462 and X80-A4B steels. However, M_s for all X100 steels are lower than those for X80 steels.

Therefore, all the factors discussed above, including higher CT, higher C and austenite stabilizer compositions, and lower M_s, together affect the amount of retained austenite.

Table 5-5 – Maximum retained austenite phase (wt%) for X80 and X100 steels

Steel	Austenite Phase (wt%)	Normalized CT/ICT	M_s (°C)	Ni	Cr	Mo	Mn	C
X80-462	/	1.47	423	0.13	0.05	0.297	1.69	0.030
X80-A4B	2.37	1.32	418	0.25	0.07	0.305	1.70	0.035
X80-A4F	6.15	1.28	407	0.41	0.08	0.404	1.77	0.052
X80-B4F	7.05	1.42	410	0.41	0.06	0.299	1.62	0.052
X100-2A	/	1.00	406	0.47	0.17	0.41	1.81	0.039
X100-2B	/	0.90	395	0.44	0.17	0.40	1.87	0.065
X100- 3C	1.77	1.14	398	0.40	0.19	0.40	1.88	0.064

5.3.2 The effect of processing

The reheating temperatures were assumed to be similar for all the steels. All steels were subjected to a controlled rolling schedule in which approximately 70% reduction was applied between the no-recrystallization temperature and the FRT. There were no major differences in FRT. Subsequent to rolling, the steels were subjected to accelerated cooling to an interrupted cooling temperature or CT. There were some differences in CT and CR for the steels studied, especially when comparing different grades of steels.

5.3.2.1 Effect of CT

The subgrain size increased and dislocation density decreased with increasing normalized CT, as shown in Figure 5-13 and Figure 5-14, respectively. A better combination of yield strength and toughness is achieved at lower CT,[79] which is believed to be due to a microstructure with finer subgrains and higher dislocation density. Accelerated cooling starts at the FRT and is completed at the CT (or interrupted cooling temperature for X100 steels). After the coiling process, the strip remains at a relatively higher temperature for X80 steels compared with X100 steels and then cools down to room temperature with a CR of approximately 38°C/min,[80] during which the subgrains coarsen.

There have been many studies conducted concerning the effect of CT on the dislocation density and it was found that a lower CT leads to a higher dislocation density.[28,29] Decreasing the CT results in a lower transformation temperature microstructure which has a higher dislocation density, e.g., martensite or more bainitic ferrite. A bainitic ferrite microstructure has a higher dislocation density compared with polygonal ferrite, while the dislocation density in martensite is even higher than that in the bainitic structure.

As shown in Figure 5-13 and Figure 5-14, greater variations of subgrain size and dislocation density were observed at the center of the strip (dashed line in Figure 5-13 and Figure 5-14) when compared with the surfaces (solid line Figure 5-13 and Figure 5-14). This is an indication of more changes in processing parameters at the center of the strip for different steels relative to the nominal

processing parameters that Evraz provided, e.g., CT. This may be due primarily to differences in plate/pipe thicknesses.
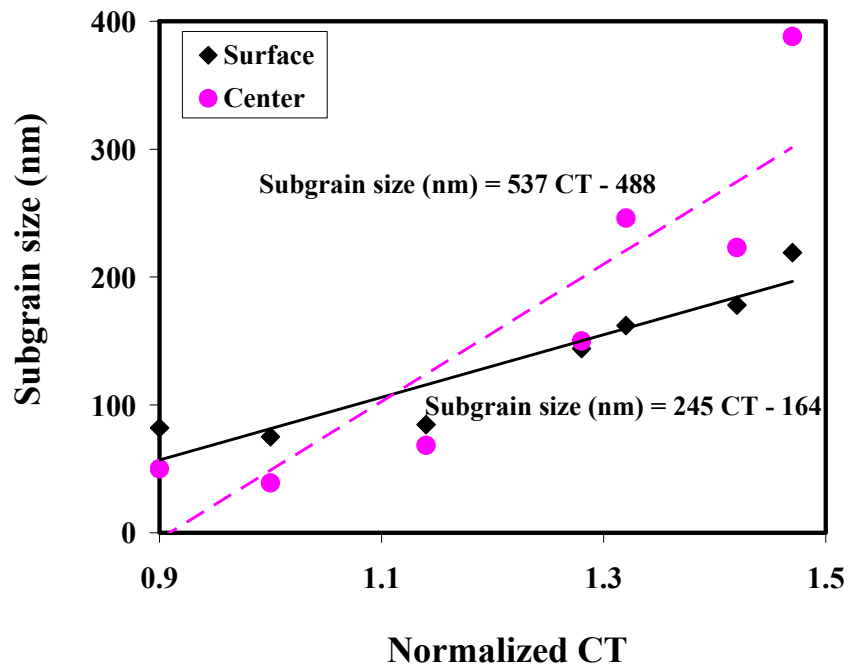

Figure 5-13- Subgrain size (nm) vs. normalized CT for the seven steels.
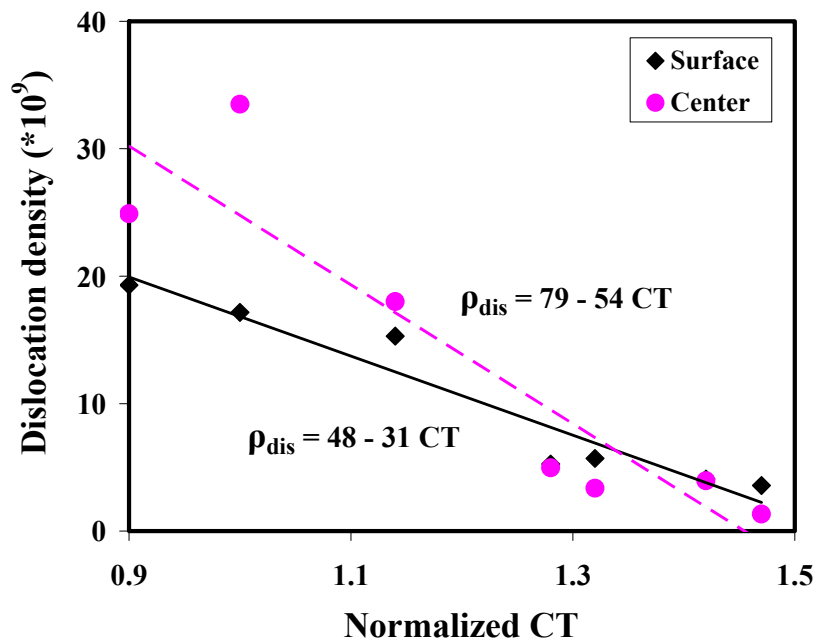

Figure 5-14 – Dislocation density ($\times 10^9$ cm/cm^3) vs. normalized CT for the seven steels.

Texture index decreased with increasing normalized CT, as shown in Figure 5-15. It is believed that texture index is more dependent on the rolling conditions. In general, the texture indices at the center of the strip are above 1.2; however, the values are below 1.1 at the pipe/plate surfaces. Misra also found stronger texture at the center of microalloyed steels, which were hot rolled with 95% reduction.[35]

The reasons for the texture index variation with CT are not clear. Further study into texture types and corresponding intensity are needed. Mesplont extensively investigated the evolution of the texture as a function of CT for microalloyed steel using EBSD, and relationships of CT with specific textures were discussed. However, no conclusion on the effect of CT on general texture intensity was reached.[81] Generally, X100 steels, have stronger texture than X80 steels, as shown in Figure 5-15. X100 steels are mostly composed of bainitic ferrite and acicular ferrite and X80 steels mainly consist of polygonal ferrite and acicular ferrite, as discussed in Section 4.4. Bhadesia has indicated that the texture in bainitic ferrite, which is inherited from the austenite phase, is more prominent, in comparison to the case where austenite transforms to polygonal ferrite. [82]
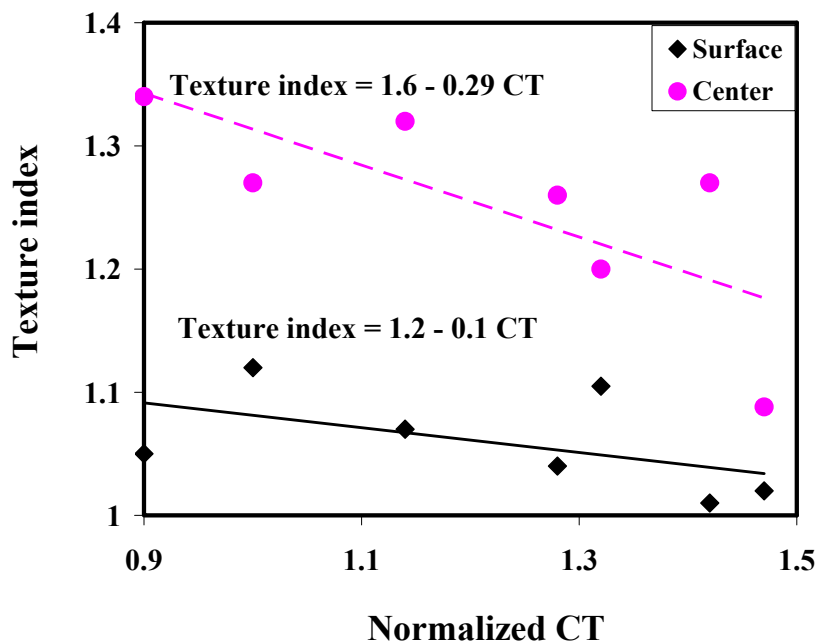

Figure 5-15 – Texture index vs. normalized CT for the seven steels.

5.3.2.2 Effect of CR

Generally, there were no effects observed for normalized CR on the microstructural features, including subgrain size, dislocation density and texture index, as shown in Figure 5-16, Figure 5-17 and Figure 5-18.

The four X80 steels have the same CR (Figure 5-16); however, different subgrain sizes were observed at the center or the surface. The difference in subgrain size for four X80 steels is believed to due to other factors, e.g., CT and chemistry. For the X100 steels, the subgrain sizes are almost constant, although there were differences in CR. As such, there is no effect of CR on subgrain size.

The four X80 steels also have different dislocation densities, which may be not be clear in Figure 5-17, since the scale for dislocation density was expanded due to the high values for the X100 steels. The differences in dislocation density are shown in Tables 4-6, 4-7, 4-8 and 4-9. For the three X100 steels, dislocation density seems to increase with increasing CR, especially the dislocation density at the center. However, the high dislocation density for X100-2A is believed to be due to the alloying element B. X100-2B has a relatively high dislocation density compared with X100-3C, since it has a lower CT (0.9) relative to X100-3C (1.14), which corresponds to a 94°C difference.

As shown in Figure 5-18, with the same CR for four X80 steels, texture index shows a range of values. For the X100 steels with different CR values, the texture indices are generally constant. Therefore, CR has little effect on texture index, either at the surface or center.
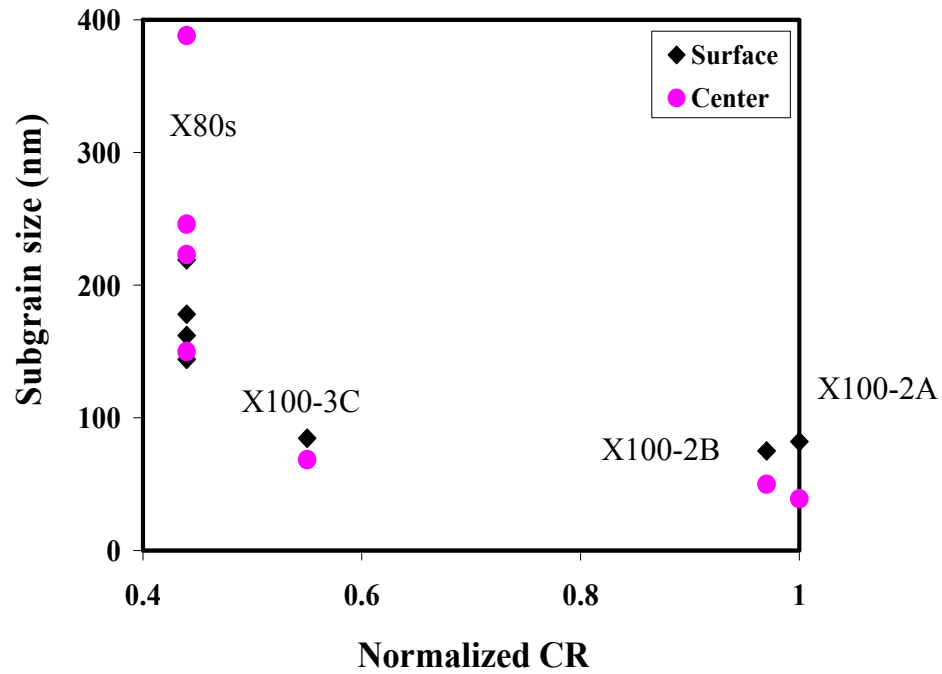
Figure 5-16 - Subgrain size (nm) vs. normalized CR for the seven steels.
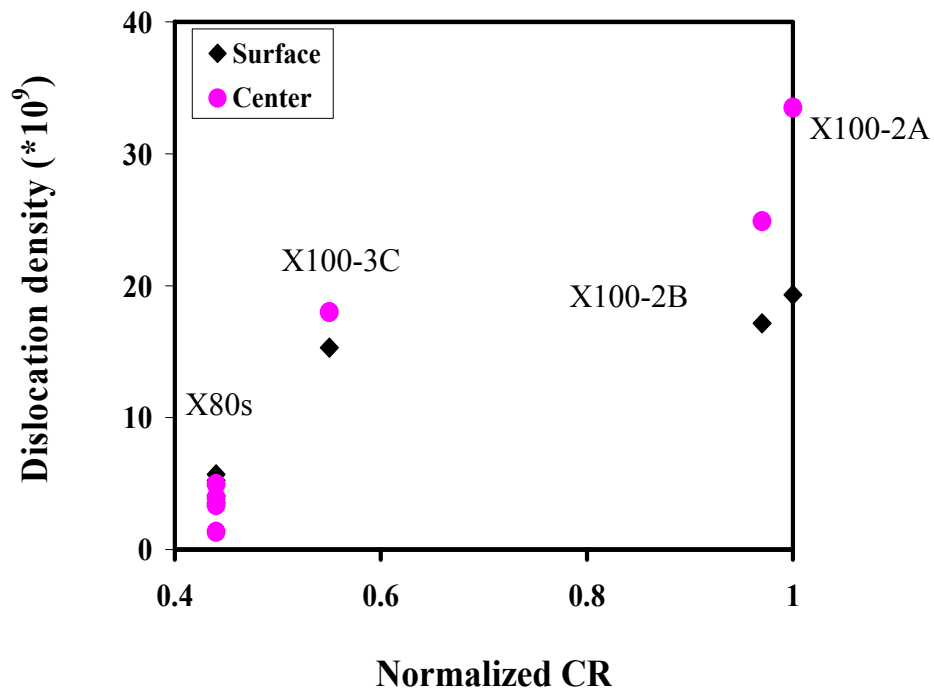

Figure 5-17 - – Dislocation density ($\times 10^9$ cm/cm^3) vs. normalized CR for the seven steels.
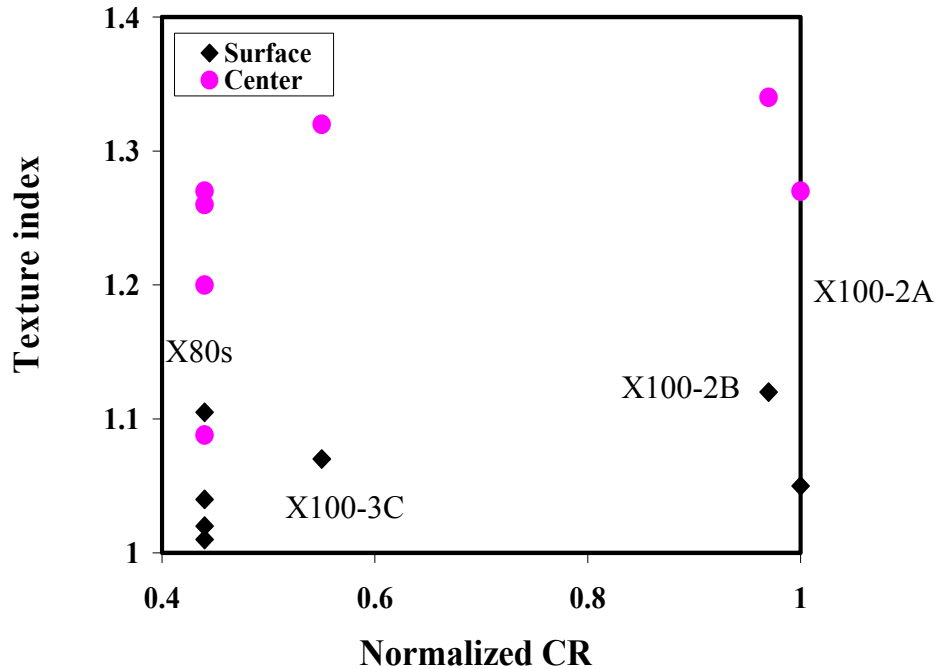
Figure 5-18 – Texture index vs. normalized CR for the seven steels.

Other parameters, including reheat temperature and FRT, all affect the final microstructure, so every parameter should be optimized during design. For example, the percent of deformation during each rolling stage would also have an effect on the final grain size. Deformation during finish rolling, at temperatures below the austenite recrystallization temperature and above the transformation temperature, forms deformation bands and increases the dislocation density. Since ferrite nucleates both on austenite grain boundaries and deformation bands, the ferrite grains would be finer with higher deformation. The detailed effects of these parameters on microstructure can be found in Chapter 2.

5.3.3 The effect of chemistry

The desired steel properties are achieved by selection of both optimal TMCP and composition, so the influence of alloying elements on microstructure should be considered as well. Adding alloying elements has various effects during different stages of the whole TMCP, changing the transformation temperature, as

well as increasing the hardenability, corrosion resistance, electrical resistance, wear resistance and weldability.

Figure 2-9 shows that different alloying elements lower or increase the transformation temperature, depending on whether they are austenite stabilizers or ferrite stabilizers. A lower austenite to ferrite transformation temperature can be obtained by adding austenite stabilizers, allowing a fine grain or subgrain size to be attained. In particular, austenite stabilizers Mn and Ni generally exist in microalloyed steels at higher levels than in structural carbon steels, and control the transformation temperature and kinetics and refine the structure. Also as discussed in Chapter 2, adding Mo, Mn and Ni can promote the formation of a bainitic structure. In this section, the effect of these alloying elements on subgrain size is evaluated. The results obtained from the Rietveld method for the seven steels in this study also verified the effects of alloying elements, i.e., Mo, Ni, and Mo, on refining substructure.

Figure 5-19 shows the effects of Mn on the subgrain size and Figure 5-20 shows the effects of Ni and Mo on the subgrain size. Mn, Mo and Ni enhance the hardenability of the steels to allow for the formation of enough bainitic ferrite to increase the strength while maintaining sufficient impact toughness. Compared with Ni, both Mn and Mo have stronger effects on the hardenability, however, Mn has a slightly more pronounced effect than Mo. The relative hardening effects for the Mo and Ni have been considered in Figure 5-20 by incorporating the appropriate multiplying factors (Mo is approximately 8 times more effective than Ni).[83]

In both figures, the solid lines and dashed lines represent the microstructural features obtained from the surface and the center of the strip, respectively. As shown by Figure 5-19 and Figure 5-20, increasing the concentration of these threee elements refine the substructure. As described above, Mn, Ni and Mo increase the hardenability and promote the formation of bainitic ferrite or acicular ferrite by shifting the CCT diagram to longer times. Bainitic ferrite and acicular ferrite have finer substructures than polygonal ferrite.[70] Adding Mn and Ni lowers

the austenite to ferrite transformation temperature, allowing finer structure to be obtained.
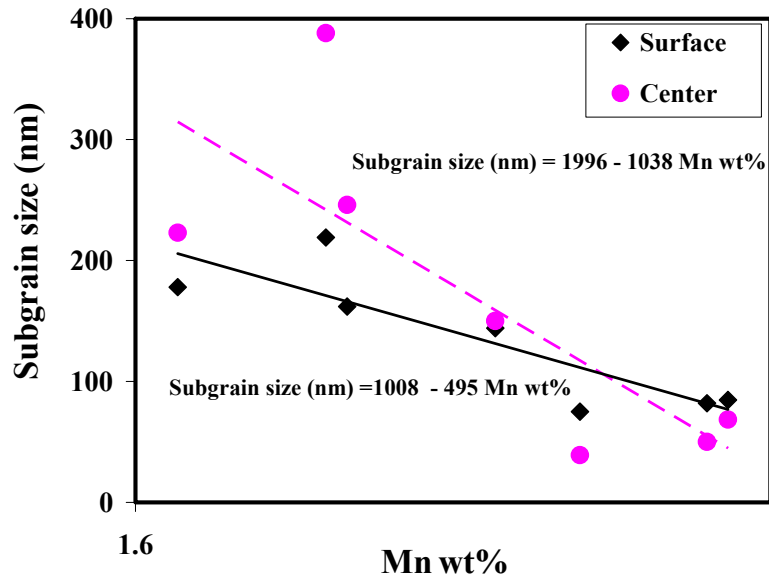

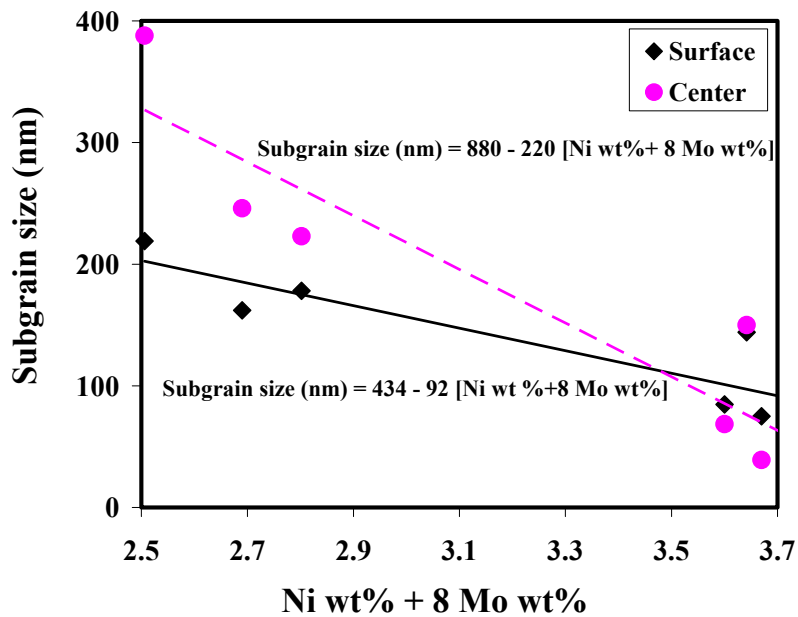Figure 5-19 - The effects of alloying elements Mn and Ni on the subgrain size for the seven steels.

Figure 5-20- The effects of alloying elements Mn, Ni and Mo on the subgrain size for the seven steels.

5.3.4 The effect of grain structure

Two steels were selected as representatives for the X80 steels and X100 steels, X80-462 and X100-2A. They were studied using TEM for grain structure analysis and Figure 4-7 (A) and Figure 4-8 show typical microstructures for X80-462 and X100-2A, respectively. X80-462 is mainly composed of acicular ferrite and X100-2A is mostly composed of bainitic ferrite with a lath structure. The characteristics for the two different grades of steels are also shown by SEM imaging. SEM images for X80-462 and X100-2A are shown in Figure 5-21. The microstructure of X100-2A shows a more bainitic structure, which should result in a finer subgrain size and a higher dislocation density, compared with polygonal ferrite.

(A)   (B)
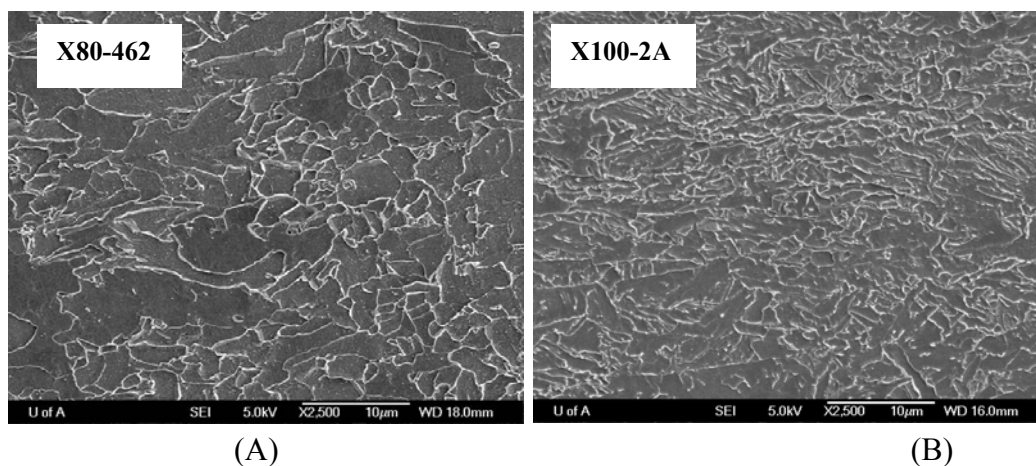
Figure 5-21 - SEM images for X80-462 (A) and X100-2A (B) steels.

5.4 The relationship between microstructures and properties

There are four main strengthening mechanisms: solid solution strengthening, grain refinement, precipitation strengthening and work hardening. The contributions from each are shown in the equation 5-2 below.[5]

$$\sigma_y(MPa) = \sigma_i + k_y d^{-1/2} + \left(\frac{10.8 v_f^{1/2}}{x}\right) \ln\left(\frac{x}{6.125*10^{-4}}\right) + \sum k_i C_i \quad (5\text{-}2)$$

where σ_y is the yield stress, σ_i is the friction stress of iron, k_y is the strengthening coefficient for grain size, d is the grain diameter in microns, x is the size of the precipitates in microns, v_f is the volume fraction of a given precipitate size, k_i is the strengthening coefficient for solute strengthening of solute i and C_i is the concentration of solute i.

In this study, subgrain size and dislocation density have been characterized. Figure 5-22 and Figure 5-23 show the effect of subgrain size and dislocation density on the yield strength, respectively. Both subgrain size and dislocation density are average values for the five pieces of each steel. The dots represent the experimental data and the solid line represents the regression relationship. The yield strength increases linearly with the square root of the dislocation density and with the inverse of the square root of the subgrain size.
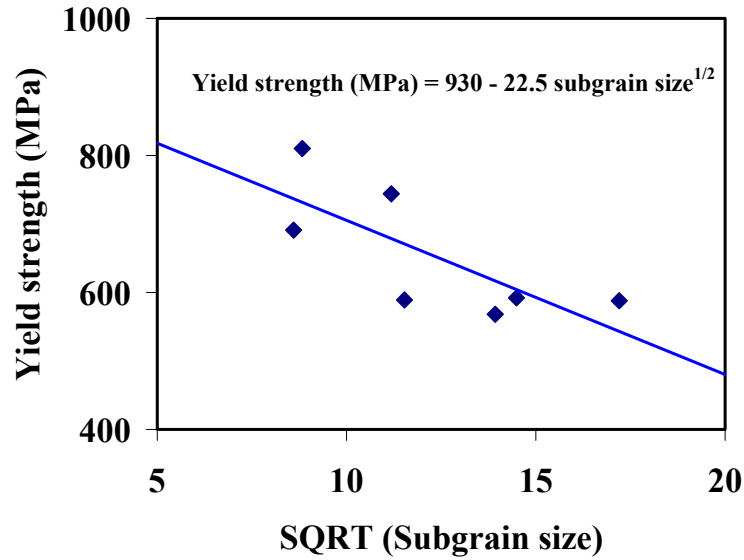
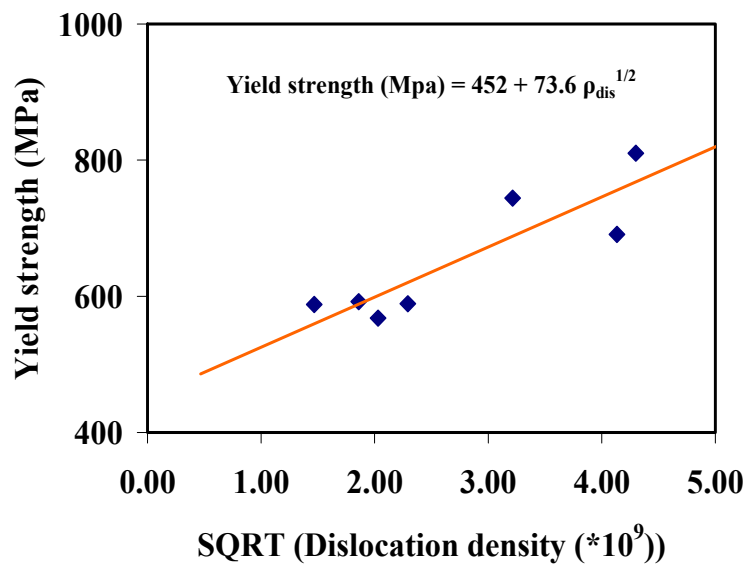Figure 5-22 – Yield strength relationship with subgrain size
for the seven steels.

Figure 5-23 – Yield strength relationship with dislocation density
for the seven steels.

6. CONCLUSIONS

Microstructures for four X80 and three X100 steels have been fully characterized by XRD (Rietveld method). Other techniques, including OM, SEM and TEM, were also applied to verify the data obtained by the Rietveld method. WDS was used to study chemistry differences through thickness for each steel. Variations in microstructural features, including subgrain size, dislocation density, texture index and retained austenite phase weight fraction, were studied both through pipe/plate thickness and among the different steels. Variations in these features were discussed based on differences in chemistry, processing parameter and grain structure. In this section the conclusions obtained in this study are presented.

Technique

- The Rietveld method can be used to quantify subgrain size, microstrain, texture and retained austenite phase weight fraction in microalloyed steels.
- Subgrain size measured by TEM and the Rietveld method are of the same order of magnitude, but show some differences.

Microstructure

X80 steels (X80-462 and X80-A4B)

- The matrix of the steels is composed of polygonal ferrite and acicular ferrite. The grains are irregular in shape and elongated along the rolling direction.
- The maximum dislocation density and finest subgrain size were observed at the pipe surfaces.
- Texture index values overall were low through the pipe thickness, indicating little preferred orientation.
- Retained austenite phase weight fractions overall were low through the pipe thickness.

- There was no significant composition change in the alloying elements through the pipe thickness.

X80 steels (X80-A4F and X80-B4F)

- The matrix of the steels is composed of polygonal ferrite and acicular ferrite. The grains are irregular in shape and elongated along the rolling direction.
- There were no significant variations in dislocation density and subgrain size through thickness.
- Texture index values were higher near the centerline, i.e., 1.26 at the center relative to 1.01 at the surface for X80-A4F and 1.27 at the center relative to 1.01 at the surface for X80-B4F.
- Retained austenite phase weight fraction was higher at the center of the strip.
- There was no significant composition change in alloying elements through the pipe thickness.

X100 steels

- The X100 steels consisted of a mainly bainitic structure (lath structure) and acicular ferrite.
- No major variations were observed through thickness in subgrain size values and dislocation density.
- Texture index values were higher at the center of the strip.
- Generally, retained austenite phase weight fractions were below the sensitivity of the XRD technique.

Comparison of the microstructural features among different steels

- The matrix of the X80 steels is mostly composed of polygonal ferrite and acicular ferrite, while the X100 steels contained mainly bainitic structure (lath structure) and acicular ferrite.

- The X100 steels have finer subgrain sizes and higher calculated dislocation densities than the X80 steels.

The effects of processing

- Subgrain size increased with increasing CT.
- Calculated dislocation densities decreased with increasing CT.
- Texture index values decreased with increasing CT
- Subgrain size decreased with increasing CR.
- Calculated dislocation densities increased with increasing CR.
- Texture index slightly increased with increasing CR.

The effects of chemistry

- Alloying elements, such as Ni, Mo and Mn, are helpful in refining the subgrain grain size.
- Higher CT and higher carbon content, combined with austenite stabilizers, are helpful to obtain higher retained austenite phase weight fractions.
- The variations in microstructural features among the different steels at the surfaces are more pronounced than those obtained at the center of the strip.

The effects of grain structure

- The lath structure in X100 steels may contribute to the higher dislocation density and finer subgrain size in comparison with the X80 steels.

Mechanical properties

- The higher yield strengths for the X100 steels compared with the X80 steels are due to the higher dislocation densities and finer subgrain sizes to some extent.
- Yield strength shows a linear relationship with the inverse of the square root of the subgrain size.

- Yield strength shows a linear relationship with the square root of dislocation density.

7.   FUTURE WORK

7.1 Neutron diffraction analysis

In this study, bulk samples were sliced into several thin pieces through the thickness direction in order to examine the effect of sampling position on microstructure. A standard sample preparation procedure was established using annealed samples; however, neutron diffraction could provide an alternative method without the time consuming sample preparation. Since neutrons can penetrate much deeper than X-rays (up to ~30mm in steel), bulk samples can be tested.

7.2 Texture analysis

EBSD or neutron diffraction or X-ray diffraction with texture goniometers could be used to analyze the texture types with better quantification, since the Rietveld method only gives a general idea of the extent of the texture, i.e., whether it is weak, moderate or strong. Pole figures or orientation distribution functions (ODF) could be obtained and then the specific type of texture with corresponding intensity could be identified. The same steels could be used for this purpose. Comparison of the texture index obtained using XRD and texture information obtained by other techniques could be made and confirmation of texture index from Rietveld method could also be achieved. In addition, understanding the effect of processing parameters on the specific texture type could be established and overall texture intensity as well.

REFERENCES

[1] I.V. Alexandrov, K. Zhang, A.R. Kilmametov, K. Lu, and R.Z. Valiev, "The X-ray characterization of the ultrafine-grained Cu processed by different methods of severe plastic deformation," Materials Science and Engineering A – Structural Materials Properties Microstructure and Processing, 1997, vol. 234, pp. 331-334.

[2] P. Mukherjee, A. Sarkar, P. Barat, S.K. Bandyopadhyay, P. Sen, S.K. Chattopadhyay, P. Chatterjee, S.K. Chatterjee, and M.K. Mitra, "Deformation characteristics of rolled zirconium alloys: a study by X-ray diffraction line profile analysis," Acta Materialia, 2004, vol. 52, pp. 5687-5696.

[3] J. Ghosh, S.K. Chattopadhyay, A.K. Meikap, and S.K. Chatterjee, "Microstructural studies on variation of defect parameters in Zr-Sn alloys and their transition with interchange of solvent and solute in Zr-Ti and Ti-Zr alloy systems by modified Rietveld method and Warren-Averbach method," Bulletin of Materials and Science, 2004, vol. 29(4), pp. 385-390.

[4] H.M. Rietveld, "Line profiles of neutron powder-diffraction peaks for structure refinement," Acta Crystallographica, 1967, vol. 22, pp. 151-152.

[5] T. Gladman, The Physical Metallurgy of Microalloyed Steels, The Institute of Materials, 1997.

[6] T. Takaaki and M. Youichi, "Application of ultra high-strength steel sheets for automotive body parts," "R&D" Kobe Steel Engineering Reports, 2002, Vol. 52(3), pp. 6-9.

[7] D.Q. Bai, I.A. Bettendorf, M.A. Cooke, I.A. Davenport, J. Asante, J. Dorricott, and I.L. Aurora, "Process for making high strength micro-alloy steel," **Patent No**.: US 6682613 B2, 2004.

[8] R.W. Cahn, P. Haasen, E.J. Kramer, and F.B. Pickering, Materials Science & Technology: A comprehensive treatment volume 7 - Constitution and Properties of Steels, Ed. F.B.Pickering, VCH-Wiley publishing, 1992.

[9] M.C. Zhao, K. Yang, and Y.Y. Shan, "The effect of thermo-mechanical control process on microstructures and mechanical properties of a commercial pipeline steel," Materials Science and Engineering A – Structural Materials Properties Microstructure and Processing, 2002, vol. 335, pp. 14-20.

[10] S.J. Zhao, Q.F. Wang, T. Pan, C.Y. Zhang, H. Su, C.F. Yang, Z.S. Yan, and Y.Q. Mang, "Fundamental evaluations on microstructure and mechanical properties of on-line normalizing V-N microalloyed N80 class oil casing," Journal of Iron and Steel Research International, 2007, vol. 14, pp. 227-233.

[11] S.C. Wang, "The effect of titanium and reheating temperature on the microstructure and strength of plain-carbon, vanadium- and niobium-microalloyed steels," Journal of Materials Science , 1990, vol. 25, pp. 187-193.

[12] Zh. Li, and D. Wu, "Effects of finishing rolling temperatures and reduction on the mechanical propertied of hot rolled multiphase steel", Journal of Zhejiang University Science A, 2007, vol. 8 (5), pp. 797-804.

[13] J. Zrnik, T. Kvachaj, D. Sripinproach, and P. Sricharoenchai, "Influence of plastic deformation conditions on structure evolution in Nb-Ti microalloyed steel," Journal of Materials Processing Technology, 2003, vol. 133, pp. 236–2420.

[14] S. Shanmugam, N.K. Ramisetti, R.D.K. Misra, T. Mannering, D. Panda, and S. Jansto, "Effect of cooling rate on the microstructure and mechanical properties of Nb-microalloyed steels," Materials Science and Engineering A – Structural Materials Properties Microstructure and Processing, 2007, vol. 460, pp. 335-343.

[15] A. Bakkaloglu, "Effect of processing parameters on the microstructure and properties of an Nb microalloyed steel," Materials Letters, 2002, vol. 56, pp. 200-209.

[16] V.B. Ginzburg, Metallurgical Design of Flat Rolled Steels, publisher - Marcel Dekker Inc., 2005.

[17] G. Dini, M.M. Vaghefi, and A. Shafyei, "The influence of reheating temperature and direct-cooling rate after forging on microstructure and mechanical properties of V-microalloyed steel 38MnSiVS5," ISIJ International, 2006, vol. 46 (1), pp. 89-92.

[18] F. Vodopivec, M. Gabrovsek, and J.J. Zvokel, "Effects of finish-rolling temperature and carbon content on microstructure and mechanical anisotropy of 0.04-0.13% Steels," Transactions of The Iron and Steel Institute of Japan, 1988, vol. 28 (2), pp. 117-124.

[19] A. Bakkaloglu, "Effect of processing parameters on the microstructure and properties of an Nb microalloyed steel," Materials Letters, 2002, vol. 56, pp. 200–209.

[20] L. Li, H. Ding, L.X. Du, H.M. Song, and F. Zheng, "Microstructures and mechanical property of low carbon manganese steel with grain boundary allotriomorphic ferrite/bainite structure," Acta Metallurgica Sinica, 2006, vol. 42, pp.1227-1232.

[21] D. Q. Bai, S. Yue, T. M. Maccagno and J. J. Jones, "Effect of deformation and cooling rate on the microstructure of low carbon Nb-B steels," ISIJ International, 1998, vol. 38, pp. 371-379.

[22] B. Donnay, J.C. Herman, and V. Leroy, "Microstructure evolution of C-Mn Steels in the hot deformation process: the stripcam model," Conference Proceedings, Second International Conference on Modeling of Metal Rolling Processes, Inst. of Mat., London, 1996, pp. 23-23.

[23] I.L. Dillamore, R.F. Dewsnap, and M.G. Frost, Metallurgical aspects of steel rolling technology, Metals Technology, 1975, pp. 294-302.

[24] M. Cohen and W.S. Owen, "Thermo-mechanical processing of microalloyed steels," Proc. Conf. "Microalloying'75," Ed. Korchynsky, M., Union Carbide, New York, 1977, pp. 2-8.

[25] V. I. Bol'shakov, and I.A. Mongait, "Hardening from the rolling heat of low-pearlite constructional steel microalloyed with niobium and vanadium," Metal Science and Heat Treatment, 1983, vol. 25 (12), pp. 42-44.

[26] L.E. Collins; M.J. Godden, and J.D. Boyd, "Microstructure of linepipe steels," Canadian Metallurgical Quarterly, 1983, vol. 22 (2), pp. 169-179.

[27] D.V. Edmonds and R.C. Cochrane, "Structure-Property Relationships in Bainitic Steels," Metallurgical Transactions A, 1990, vol. 21 (6), pp. 1527-1540.

[28] Q.Y. Sha, G.Y. Li, L.F. Qiao, P.Y. Yan, "Effect of cooling rate and coiling temperature on precipitate in ferrite of a Nb-V-Ti microalloyed strip steel," Journal of Iron and Steel Research International, 2007, vol. 14, pp. 316-319.

[29] S.Y. Nastich, Y.D. Morozov, B.F. Zin'ko, V.L. Kornilov, S.V. Denisov, E.A. Kudryakov, "Production of high-weldability steel for large-diameter pipe," Metallurgist, 2006, vol. 50, pp. 54-60.

[30] ASM International Handbook Committee, ASM Handbook -Metalworking: Bulk Forming, ASM International, 2005, vol. 14A.

[31] R.K. Ray, M.P. Butronguillen, J.J. Jones, and G.E. Ruddle, "Effect of Controlled rolling on texture development in a plain carbon and a Nb microalloyed steel," ISIJ International, 1992, vol. 32 (2), pp. 203-212.

[32] R.K. Ray, J.J. Jonas, M.P. Butronguillen, and J. Savoie, "Transformation textures in steels," ISIJ International, 1994, vol. 34 (12), pp. 927-942.

[33] H. Takatani, C.A. Gandin, and M. Rappaz, "EBSD characterization and modeling of columnar dendritic grains growing in the presence of fluid flow," Acta Mater, 2000, vol. 48, pp. 675-688.

[34] P.J. Young, O.K. Hwan, and R.H. Yong, "Texture and deformation behavior through thickness direction in strip-cast 4.5 wt% Si steel sheet," ISIJ International, 2000, vol. 40 (12), pp. 1210-1215.

[35] R.D.K. Misra and J.P. Anderson, "Transformation textures in new ultrahigh strength hot rolled microalloyed steel," Material Science and Technology, 2001, vol. 17, pp. 116-118.

[36] D. R. Tikhovskiy and F. Roters, "Simulation of the deformation texture of a 17%Cr ferritic stainless steel using the texture component crystal plasticity finite element method considering texture gradients," Scripta Materialia, 2006, vol. 54, pp. 1537-1542.

[37] D. Raabe and M. Ylitalo, "Experimental investigation of the transformation texture in hot rolled ferritic stainless steel using single orientation determination," Metallurgical and Materials Transactions A, 2007, vol. 27(1), pp. 49-57.

[38] D. Raabe, "On the influence of the chromium content on the evolution of rolling textures in ferritic stainless steels," Journal of Materials Science, 2004, vol. 31(14), pp. 3839-3845.

[39] M.Y. Huh and O. Engler, "Effect of intermediate annealing on texture, formability and ridging of 17%Cr ferritic stainless steel sheet," Materials Science and Engineering A-Structural Materials Properties Microstructure and Processing, 2001, vol. 308, pp. 74-87.

[40] W.B. Hutchinson and M. Hatherley, "An introduction to texture in metals," The institution of metallurgists, 1979.

[41] G.J. Baczynski, J.J. Jonas, and L.E. Collins, "The influence of rolling practice on notch toughness and texture development in high strength linepipe," Mater. Trans. A, 1999, vol. 30A, pp. 3045-3054.

[42] J.E. Hartmann, R. Misra, K. Devesh, A.J. Boucek, "Method of making a high-strength low-alloy hot rolled steel," **US Patent** 6488790, 2002.

[43] E. P. Degarmo, J. T. Black, and R. A. Kohser, Materials and Processes in Manufacturing (9th ed.), published by Jonh Wiley and Son Inc., 2004.

[44] M. P. Groover, Fundamentals of Modern Manufacturing: Materials, Processes and Systems (3rd ed), published by John Wiley & Sons Inc., 2007.

[45] R.A. Yough, The Rietveld Method, published by Oxford University Press, 1993.

[46] V.K. Pecharsky, and P.Y. Zavalij, Fundamentals of Powder Diffraction and Structural Characterization of Materials, published by Springer US, 2005.

[47] G. Caglioti, A. Paoletti, and F.P. Ricci, "Choice of collimators for a crystal spectrometer for neutron diffraction," Nuclear Instrument and Methods, 1958, vol. 3 (4), 223-228.

[48] A. Coelho, Technical reference of Topas Academic, 2004, pp. 54-78.

[49] P.CIZEK, J.A. Whiteman, W.M. Rainforth, and J.H. Beynon, "EBSD and TEM investigation of the hot deformation substructure characteristics of a type 316L austenitic stainless steel," Journal of Microscopy, 2004, vol. 213 (3), pp. 285-295.

[50] P. Sahu, M. De, and S. Kajiwara, "Microstructural characterization of stress-induced martensite evolved at low temperature in deformed powders of Fe-Mn-C alloys by the Rietveld method," Journal of Alloys and Compounds, 2002, vol. 346 (1-2), pp. 158-169.

[51] A.A. Cavaleiro, M.A. Zaghete, C. Paiva-Santos, M. Giotto, M. Cilense, J.A. Varela, and Y.P. Mascarenhas, "Structural characterization of LC-MN doped powders prepared by Pechini's method," Advanced Powder Technology II, 2001, vol. 189 (1), pp. 27-31.

[52] D. Martiez-Blanco, P. Gorria, J.A. Blanco, M.J. Perez, and J. Campo, "Analysis of the diffraction-line broadening on nanostructured Fe: size-strain effects induced by milling and heating," Journal of Physics-Condensed Matter, 2008, vol. 20 (33), pp. 335213.

[53] J. Ghosh, S.K. Chattopadhayay, A.K. Meikap, and S.K. Chatterjee, "Microstructure characterization of titanium-base aluminum alloys by X-ray diffraction using Warren-Averbach and Rietveld method," Journal of Alloys and Compounds, 2008, vol. 453, pp. 131-137.

[54] A.L. Ortiz, and L. Shaw, "X-ray diffraction analysis of a severely plastically deformed aluminum alloy," Acta Materialia, 2004, vol. 52(8), pp. 2185-2197.

[55] F.H.D. Torre, A.A. Gazder, CH.F. Gu, C.H.J. Davies, and E.V. Pereloma, "Grain size, misorientation, and Texture Evolution of Copper Processed by Equal Channel Agular Extrusion and the Validity of the Hall-Petch Relationship," Metallurgical and Materials Transactions A, 2007, vol. 38A, pp. 1080-1095.

[56] A.P. Maciel, P.N. Lisboa, E.R. Leite, C.O. Paiva-Santos, W.H. Schreiner, Y. Maniette, and E. Longo, "Microstructural and morphological analysis of pure and Ce-doped tin dioxide nanoparticles," Journal of The European Ceramic Society, 2003, vol. 23, pp. 707-713.

[57] I. Djerdj, and A.M. Tonejc, "Structural investigation of nanocrystalline TiO_2 samples," Journal of Alloys and Compounds, 2006, vol. 413, pp. 159-174.

[58] D.A. Hughes and N. Hansen, " Microstructure and strength of nickel at large strains," Acta Materialia, 2000, vol. 48 (11), pp. 2985-3004.

[59] P. Sahu, "Bainite and stress-induced martensite in an AISI type 300 steel: and X-ray diffraction study of the microstructure by the Rietveld method," Journal of Applied Crystallography, 2005, vol. 38, pp. 112-120.

[60] P. Sahu, A.S. Hamada, S.G. Chowdhury, and L.P. Karjalainen, "Structure and microstructure evolution during martensite transformation in wrought Fe-26Mn-0.14C austenitic steel: an effect of cooling rate," Journal of Applied Crystallography, 2007, vol. 40, pp. 354-361.

[61] G.K. Williamson, and R.E. Smallman, "Dislocation densities in some annealed and cold-worked metals from measurements on the X-ray Debye-Scherrer spectrum," Philosophical Magazine, 1955, vol. 1, pp. 34-46.

[62] H. Sitepu, B.H. O'Connor, and D. Li, "Comparatively evaluation of the March and general spherical harmonics preferred orientation models using X-ray diffraction data from molybdite and calcite powders," J. Appl. Cryst., 2005, vol. 38, pp. 158-167.

[63] Laurie Collins, Director of Research & Development Center at Evraz Inc. NA, E-mail message, April, 14th, 2008.

[64] U. Sharma, "Microstructure characterization of microalloyed linepipe steels," Master thesis, University of Alberta, 2000.

[65] D. Bai, L, Collins, F. Hamad, X. Chen, and R. Klein, "Microstructure and mechanical properties of high strength linepipe steels," Materials Science and Technology (MS&T) 2007, 2007, pp. 355-366.

[66] JCPDS Data Base, International Center for Diffraction Data, PDF #06-0696, USA.

[67] F.J. Humphreys, "Review – Grain and subgrain characterization by electron backscatter diffraction," Journal of Materials Science, 2001, .vol. 36 (16), pp. 3833-3854.

[68] G.R. Speich and W.C. Leslie, "Tempering of steel," Metall. Trans., 1972, vol. 3, pp. 1043-1054.

[69] L. Tan and T.R. Allen, " An electronbackscattered diffraction study of grain boundary-engineered incoloy alloy 800H," Metallurgical and Materials Transactions A, 2007, vol. 36, pp. 1921-1925.

[70] W.W. Cias, "Phase transformational kinetics and hardenability of low-carbon, boron-treated steels," Metallurgical transactions, 1973, vol. 4, pp. 603-614.

[71] B. K. Jha, R. Avtar, and V. S. Dwivedi, "Retained austenite and its effect on properties of a commercially produced dual phase steel," Transactions of the iron and steel institute of Japan, 1988, vol. 28 (2), pp. 125-128.

[72] S. C. Baik, S. Kim, Y. S. Jin, and O. Kwon, "Effects of alloying elements on mechanical properties and phase transformation of cold rolled trip steel sheets," ISIJ international, 2001, vol. 41 (3), pp. 290-297.

[73] J. D. Makinson, W. N. Weins, T. W. Snyder, and R. J. De Angelis, "Diffracting particle size analysis of martensite-retained austenite microstructures." JCPDS-International Center for Diffraction Data - Advances in X-ray Analysis, 2000, vol.43. pp. 326-331.

[74] P. Kuisma-Kursula, "Accuracy, precision and detection limits of SEM-WDS, SEM-WDS, SEM-EDS and PIXE in the muliti-elemetal analysis of medieval glass,'" X-ray spectrometry, 2000, vol. 29, pp. 111-118.

[75] O. Matsumura, Y. Sakuma, and H. Takechi, "Enhancement of elongation by retained austenite in intercritical annealed 0.4C-1.5Si-0.8Mn steel," Transactions of the Iron and Steel Institute of Japan, 1987, vol. 27 (7), pp. 570-579.

[76] A. Z. Hanzaki, P.D. Hodgson, and S. Yue, "Hot deformation characteristics of Si-Mn trip steels with and without Nb microalloy additions," ISIJ International, 1995, vol. 35 (3), pp. 324-331.

[77] S.J. Kim, C.G. Lee, T.H. Lee, and S. Lee, "Effects of Coiling Temperature on Microstructure and Mechanical Properties of High-strength Hot-rolled Steel Plates Containing Cu, Cr and Ni," ISIS International, 2000, vol. 40 (7), pp. 692-698.

[78] A. Basuki, and E. Aernoudt, "Influence of rolling of trip steel in the intercritical region on the stability of retained austenite," Journal of Material processing technology, 1999, vol. 9 (90), pp. 37-43.

[79] D. Bai, L.E. Collins, F. Hamad, X. Chen, and R. Klein, "Microstructure and mechanical properties of high strength linepipe steels," Proceedings of Materials Science and Technology (MS & T), Detroit, Michigan, 2007, pp. 335-366.

[80] W.F. Smith, and J. Hashemi, Foundations of Materials Science and Engineering (4th ed.), 2006, McGraw-Hill.

[81] C. Mesplont and B.C. De Cooman, " Effect of austenite deformation on crystallographic texture during transformations in microalloyed steels," Materials Science and Technology, 2003, vol. 19, pp. 875-886.

[82] H.K.D.H. Bhadeshia, "Bainite in steels," IOM communications Ltd., 2001.

[83] W.F. Smith, "Structure and Properties of Engineering Alloys," McGraw-Hill Publishing Co. 1981.

APPENDIX A - XRD PATTERNS AND DIRECT OUTPUTS FROM RIETVELD METHOD

X80-462 steel Rietveld refinement patterns through thickness
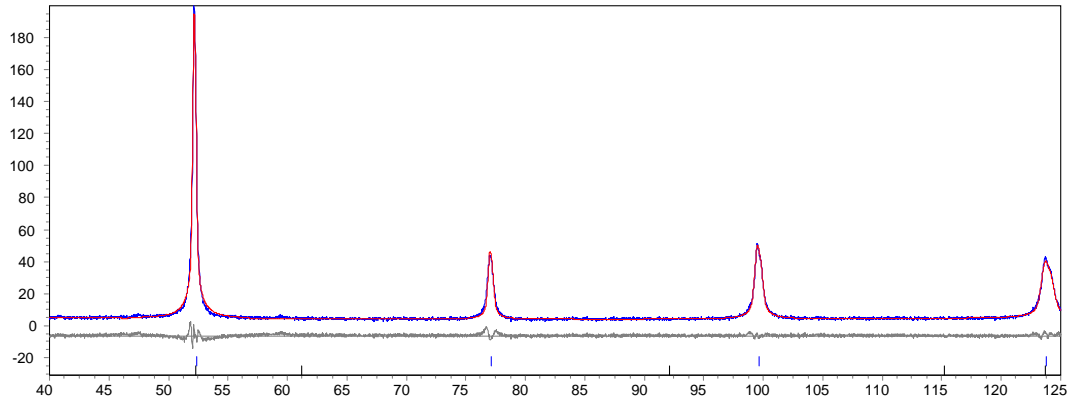
Figure A -24- XRD Rietveld refinement pattern for X80-462 at normalized position 0.
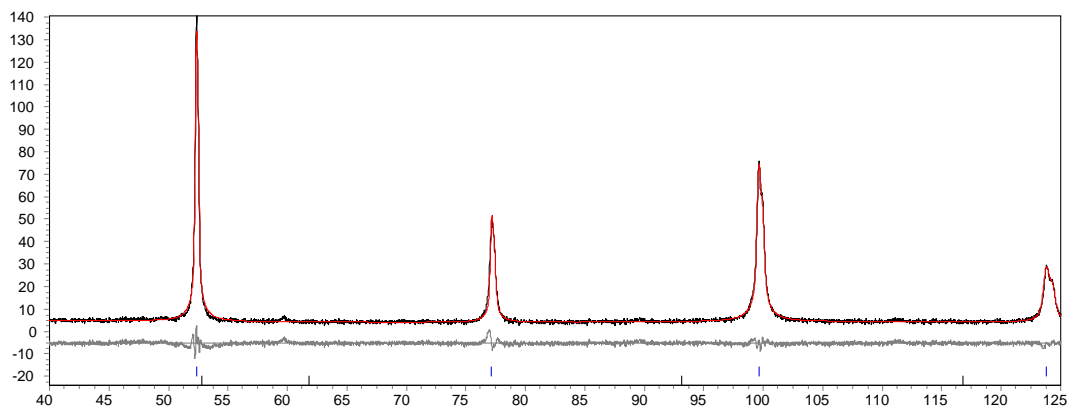
Figure A- 25 - XRD Rietveld refinement pattern for X80-462 at normalized position 1/10.
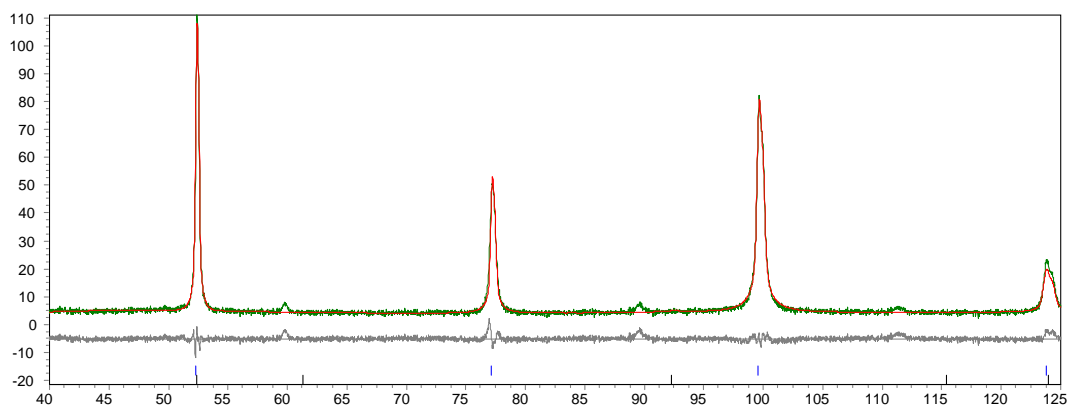
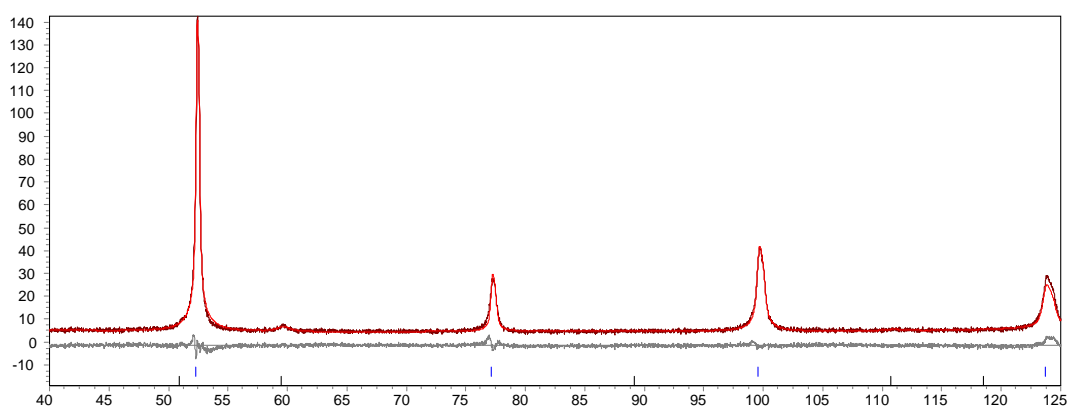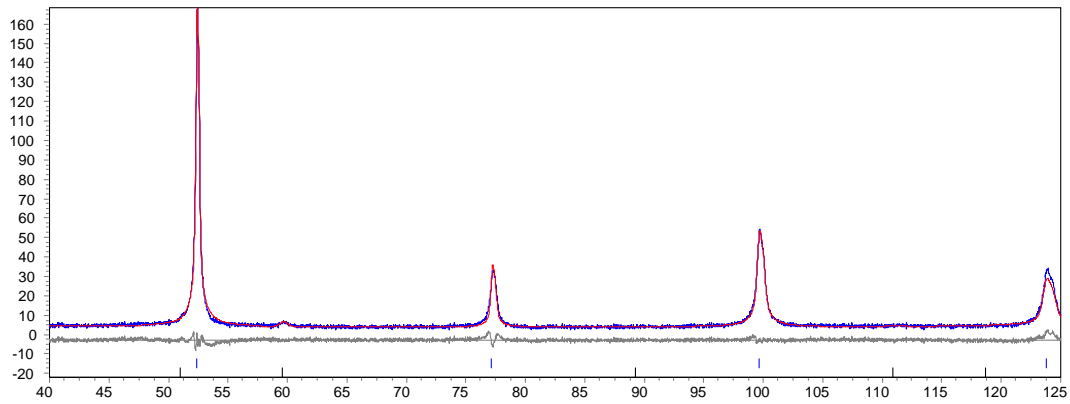Figure A- 26 - XRD Rietveld refinement pattern for X80-462 at normalized position 5/10.
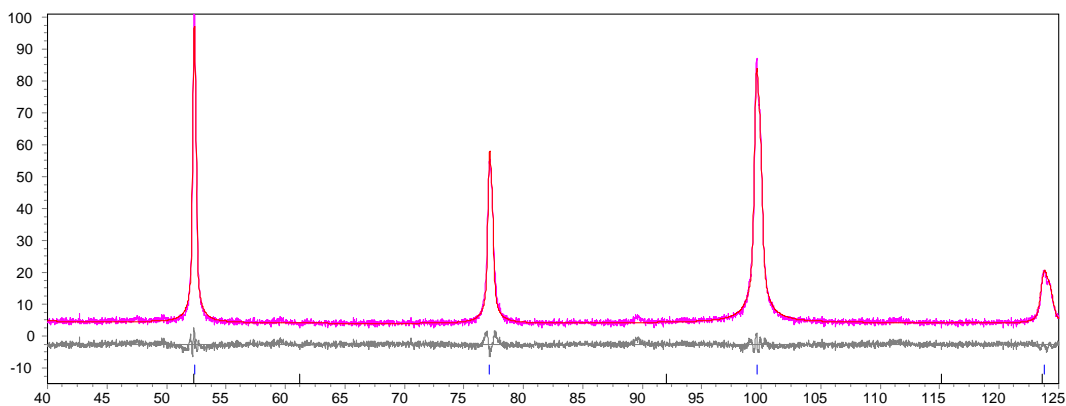
Figure A-27 - XRD Rietveld refinement pattern for X80-462 at normalized position 7/10.
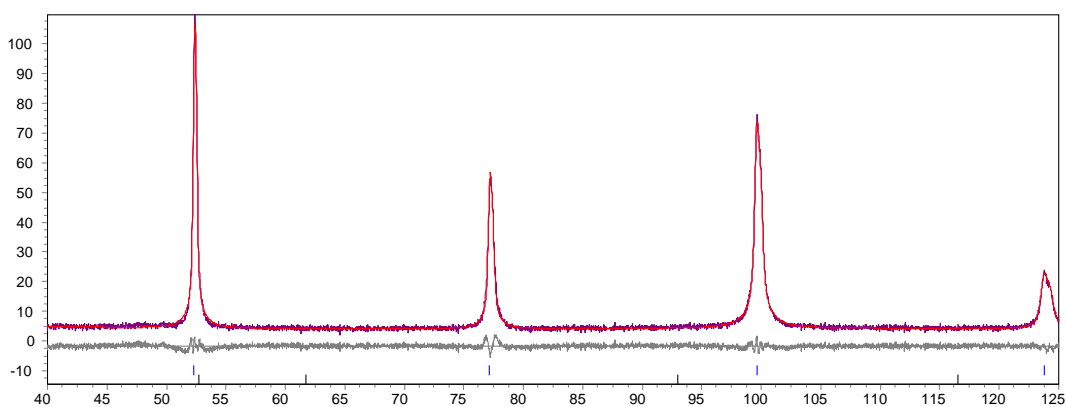
Figure A-28 - XRD Rietveld refinement pattern for X80-462 at normalized position 1.

Table A-6 – Normalized intensities for XRD patterns for steel X80-462 through thickness

Normalized position	Normalized intensity			
	I(110)	I(200)	I(211)	I(220)
0	100	5.2	6.7	5
1/10	100	3.7	7.7	4.6
5/10	100	21.2	54.9	4.8
7/10	100	30.8	74.2	4.4
1	100	24.8	48.5	4.8

X80-A4B steel Rietveld refinement patterns through thickness
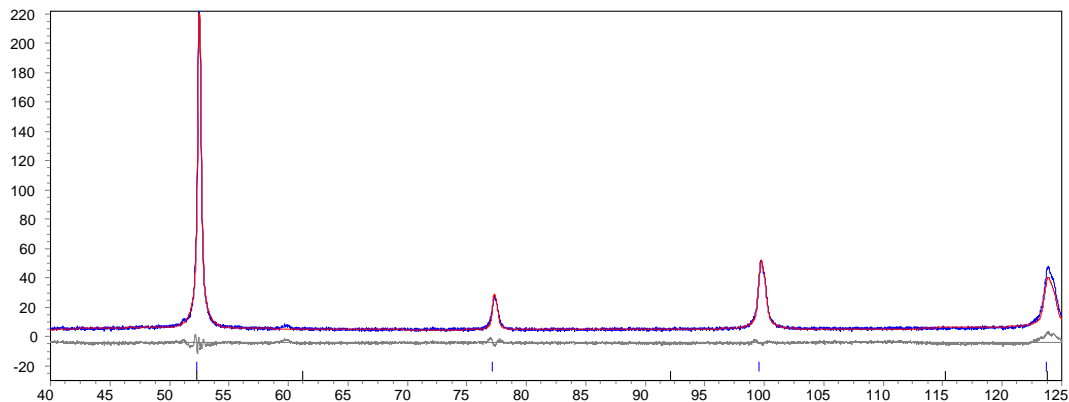
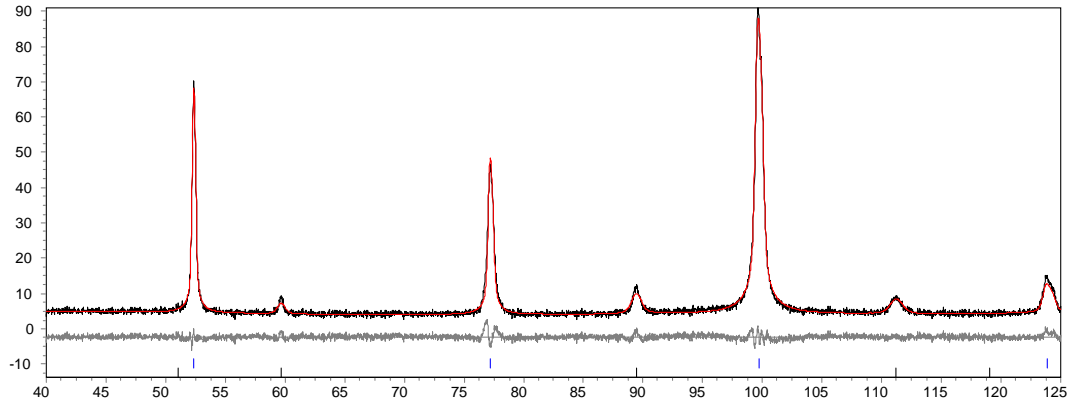FigureA-29 - XRD Rietveld refinement pattern for X80-A4B at normalized position 0.
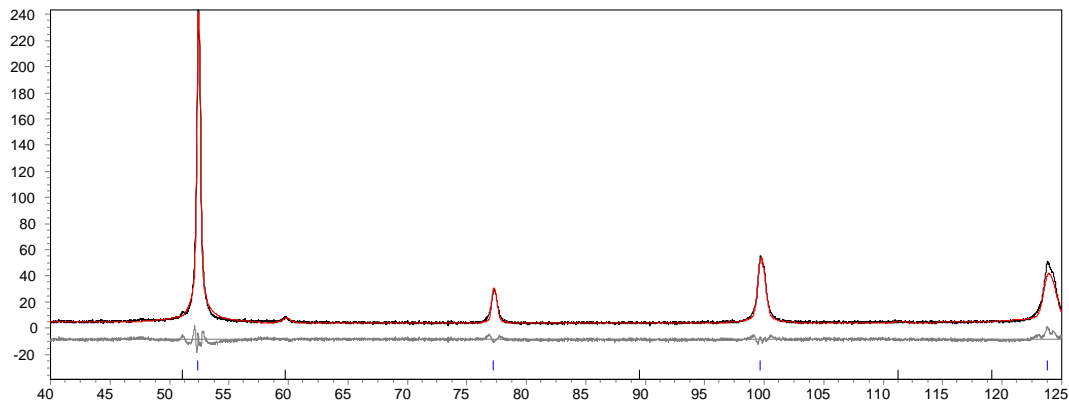
Figure A-30 - XRD Rietveld refinement pattern for X80-A4B at normalized position 3/10.
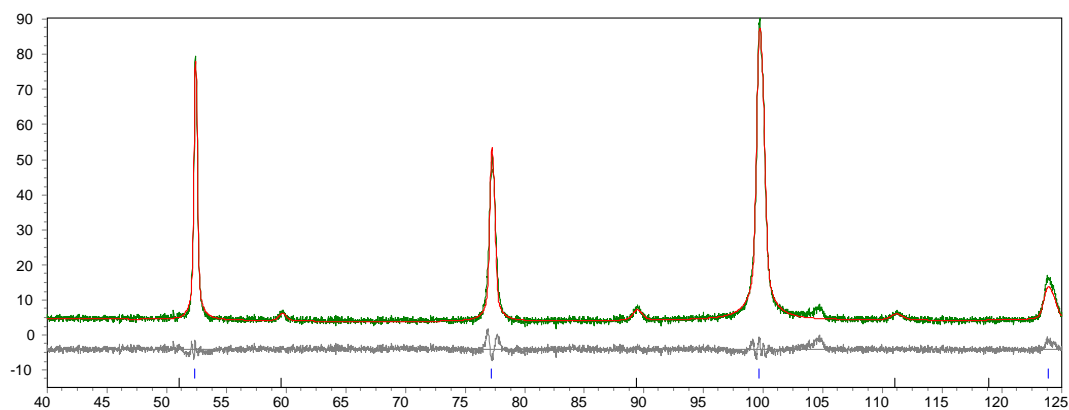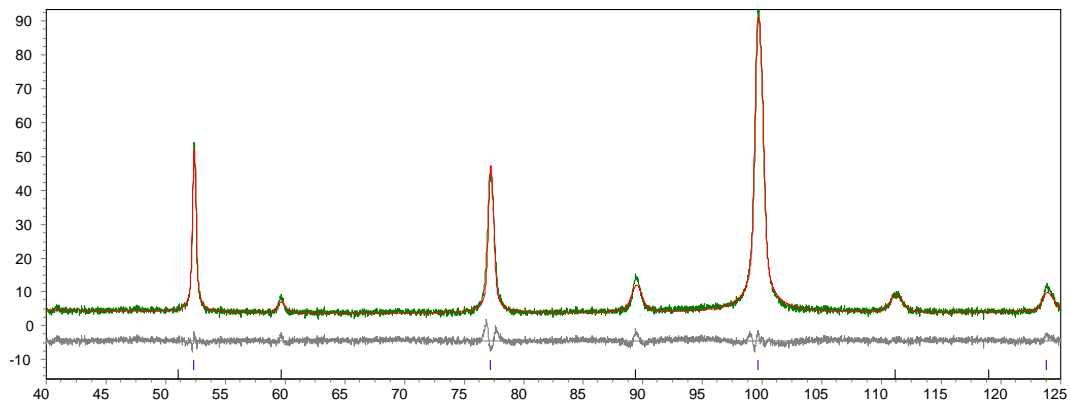

Figure A-31 - XRD Rietveld refinement pattern for X80-A4B at normalized position 5/10.
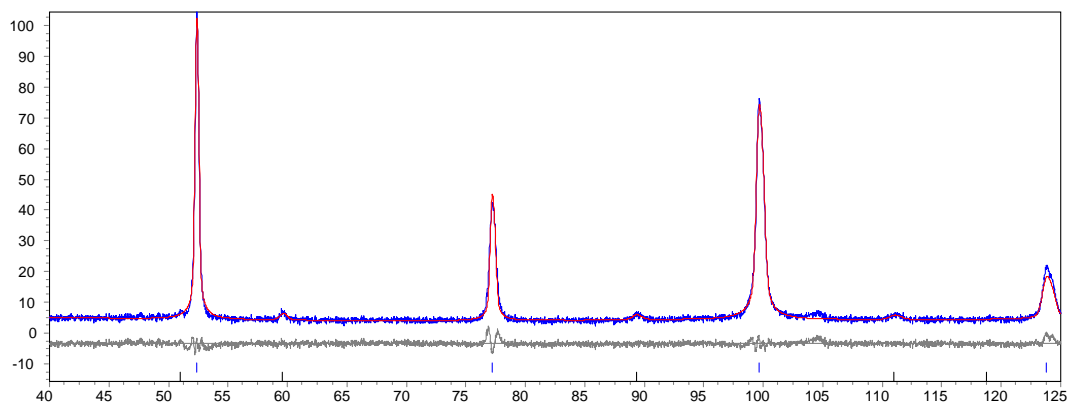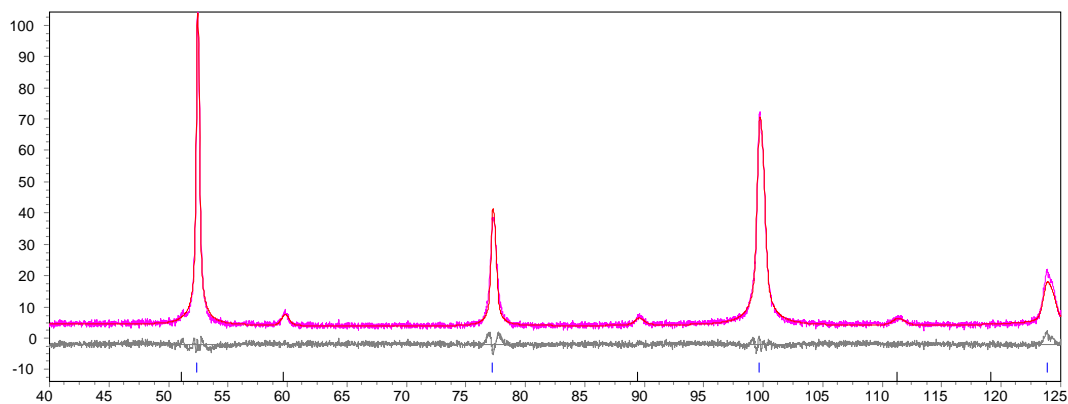
Figure A-32 - XRD Rietveld refinement pattern for X80-A4B at normalized position 8/10.
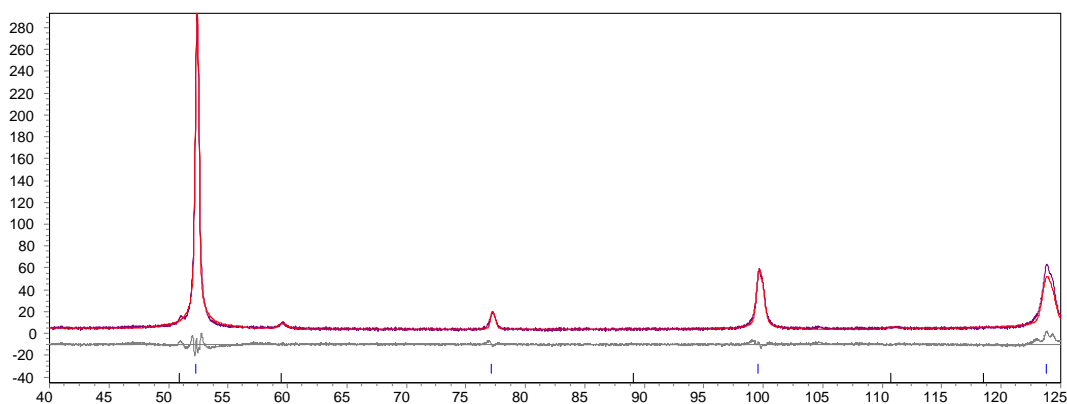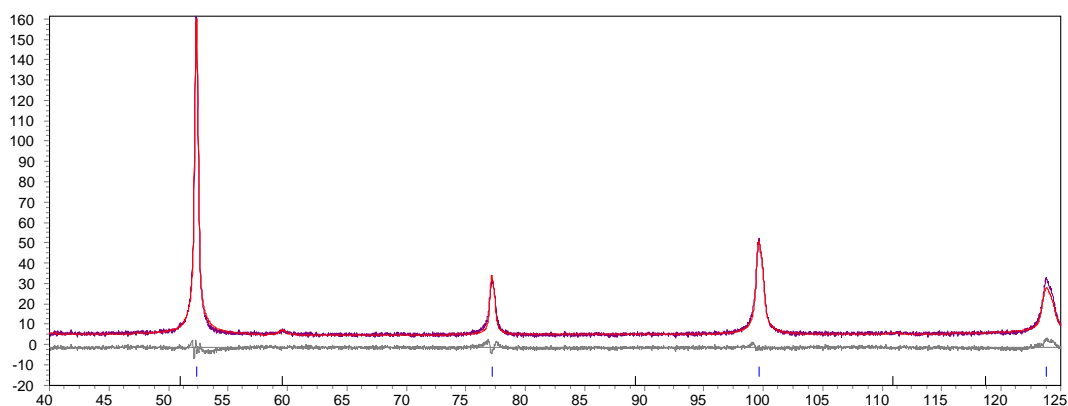

Figure A-33 - XRD Rietveld refinement pattern for X80-A4B at normalized position 1.

Table A-7 - Normalized intensities for XRD patterns for steel X80-A4B through thickness

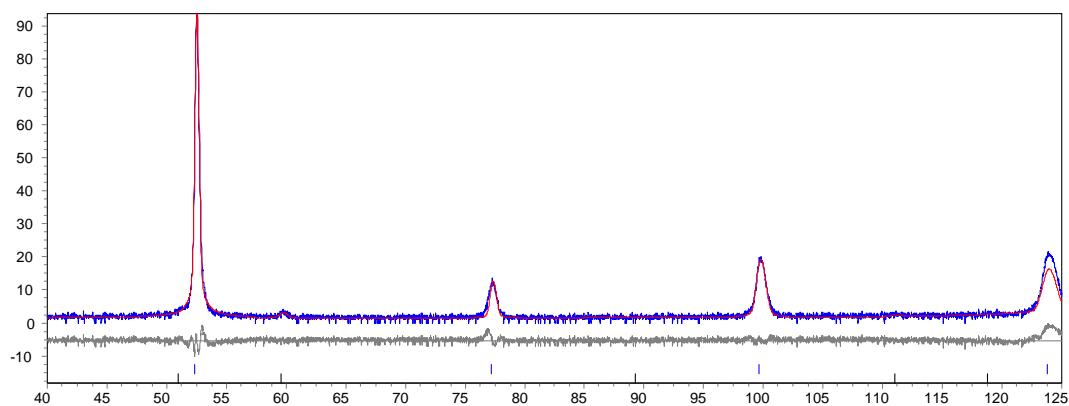| Normalized position	Normalized intensity			
	I(110)	I(200)	I(211)	I(220)
0	100	1.5	5.5	4.7
3/10	100	1.5	5.2	4.4
5/10	100	41.7	128.9	4.6
8/10	100	16.6	53.3	4.4
1	100	0.4	4.1	4.7

X80-A4F steel Rietveld refinement patterns through thickness
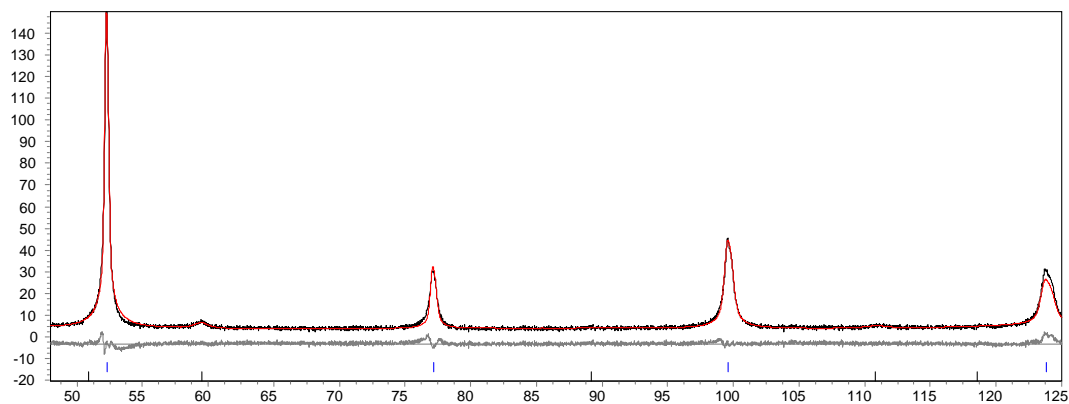
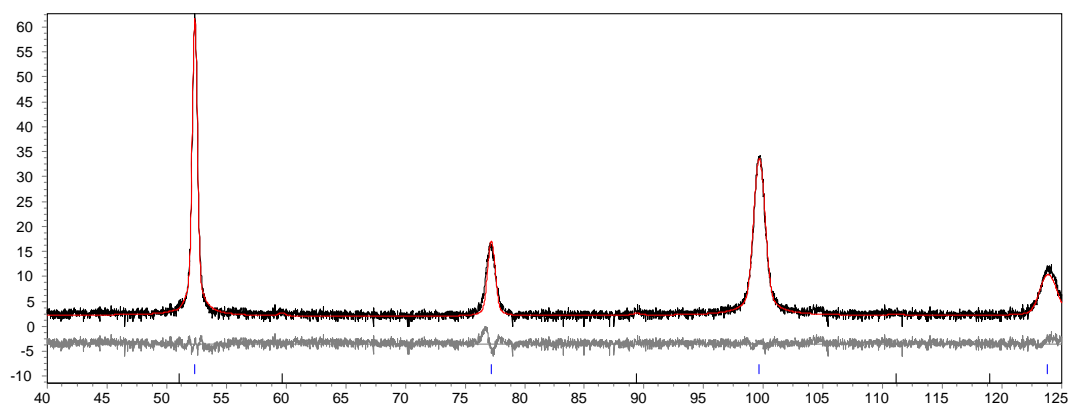Figure A-34 - XRD Rietveld refinement pattern for X80-A4F at normalized position 0.
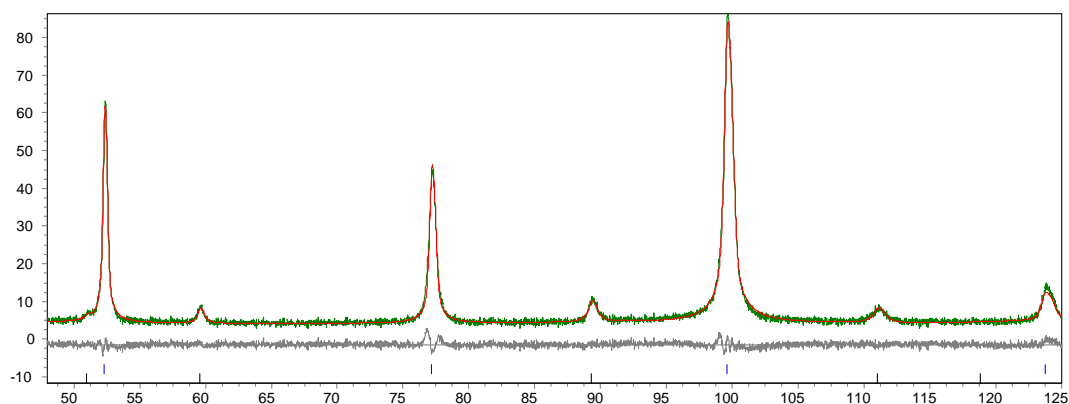
Figure A-35 - XRD Rietveld refinement pattern for X80-A4F at normalized position 3/10.
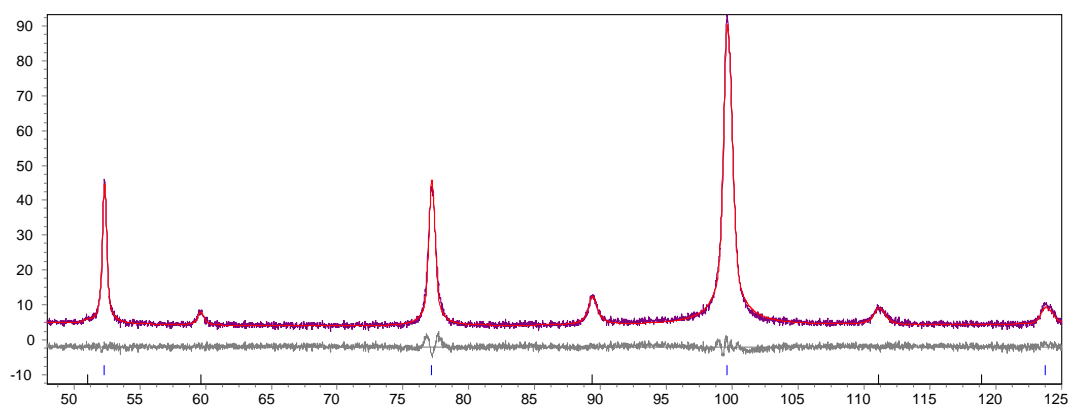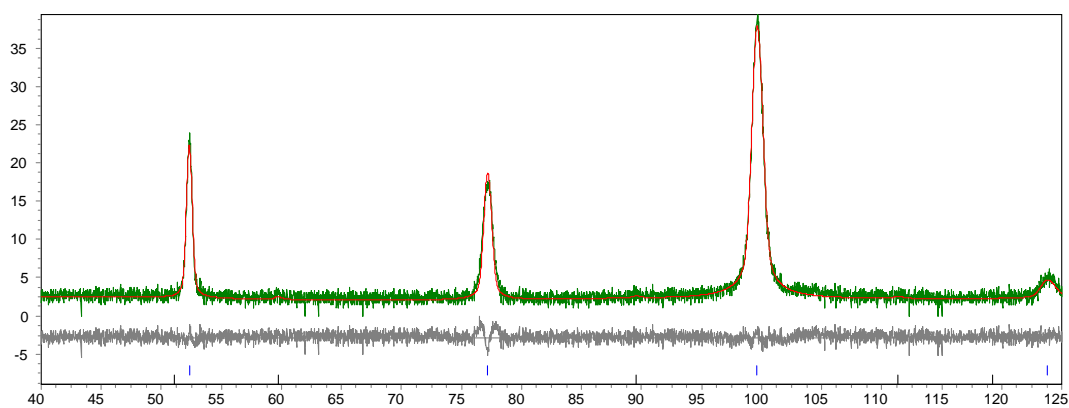

Figure A-36 - XRD Rietveld refinement pattern for X80-A4F at normalized position 5/10.
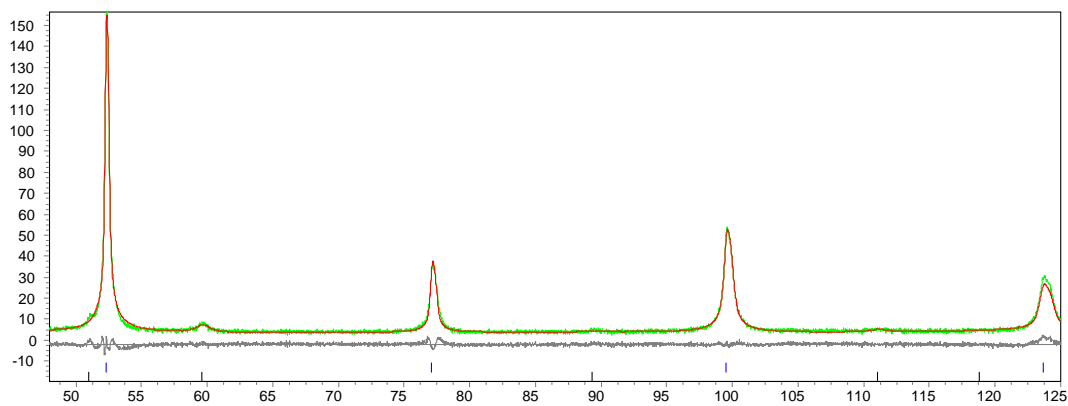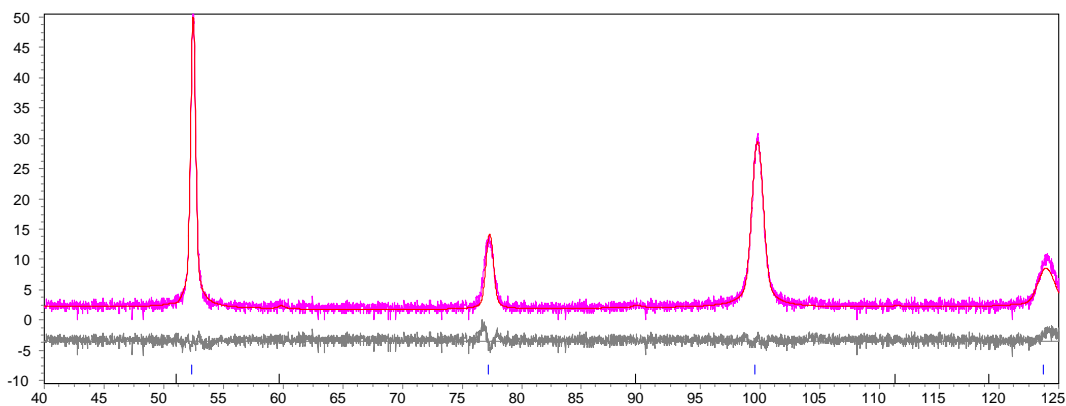
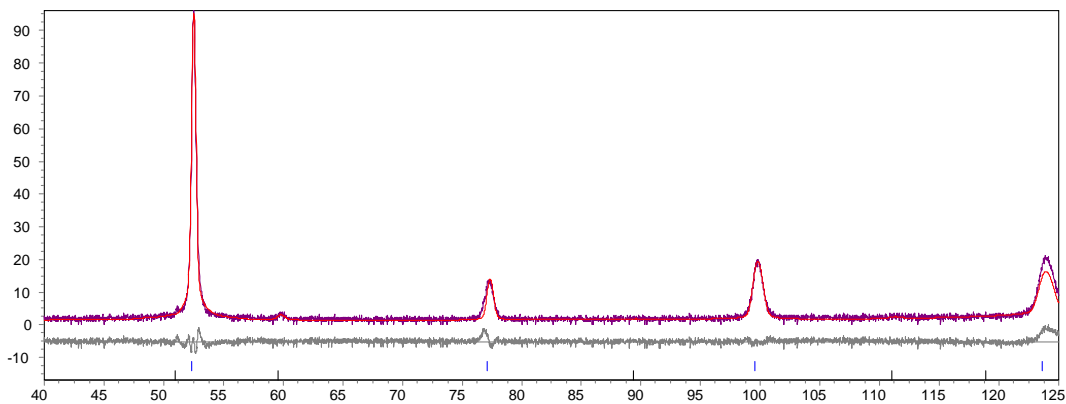Figure A-37 - XRD Rietveld refinement pattern for X80-A4F at normalized position 8/10.

Figure A-38 - XRD Rietveld refinement pattern for X80-A4F at normalized position 1.

Table A-8 - Normalized intensities for XRD patterns for steel X80-A4F through thickness

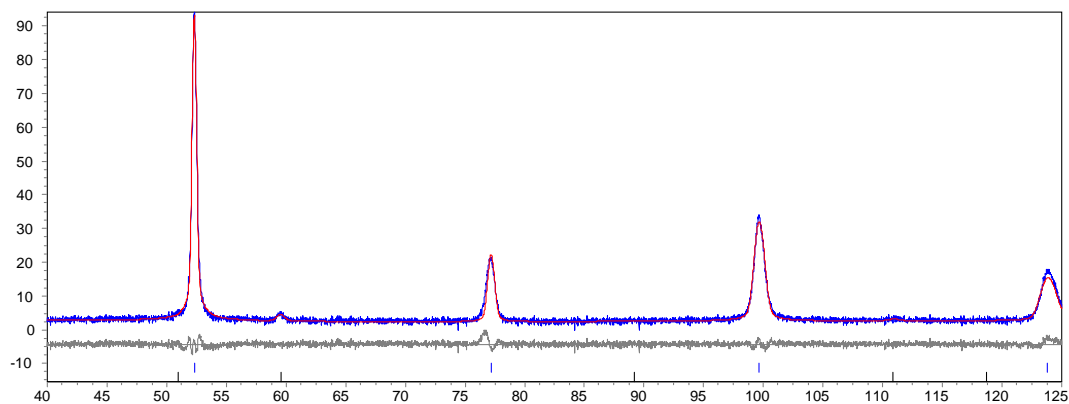| Normalized position	Normalized intensity			
	I(110)	I(200)	I(211)	I(220)
0	100	4.2	9.4	4.4
3/10	100	50.9	186.8	5.8
5/10	100	89.9	404.3	7.6
8/10	100	5.6	12.3	4.2
1	100	3.8	8.6	4.2

X80-B4F steel Rietveld refinement patterns through thickness

Figure A-39 - XRD Rietveld refinement pattern for X80-B4F at normalized position 0.

Figure A-40 - XRD Rietveld refinement pattern for X80-B4F at normalized position 4/10.

Figure A-41 - XRD Rietveld refinement pattern for X80-B4F at normalized position 5/10.

Figure A-42 - XRD Rietveld refinement pattern for X80-B4F at normalized position 8/10.

Figure A-43 - XRD Rietveld refinement pattern for X80-B4F at normalized position 1.

Table A-9 - Normalized intensities for XRD patterns for steel X80-B4F through thickness

Normalized position	Normalized intensity			
	I(110)	I(200)	I(211)	I(220)
0	100	3.9	10.4	4.1
4/10	100	44.4	167.7	4.7
5/10	100	67.9	296.3	5.2
8/10	100	13.6	48.0	4.5
1	100	3.9	10.4	4.1

X100-2A steel Rietveld refinement patterns through thickness

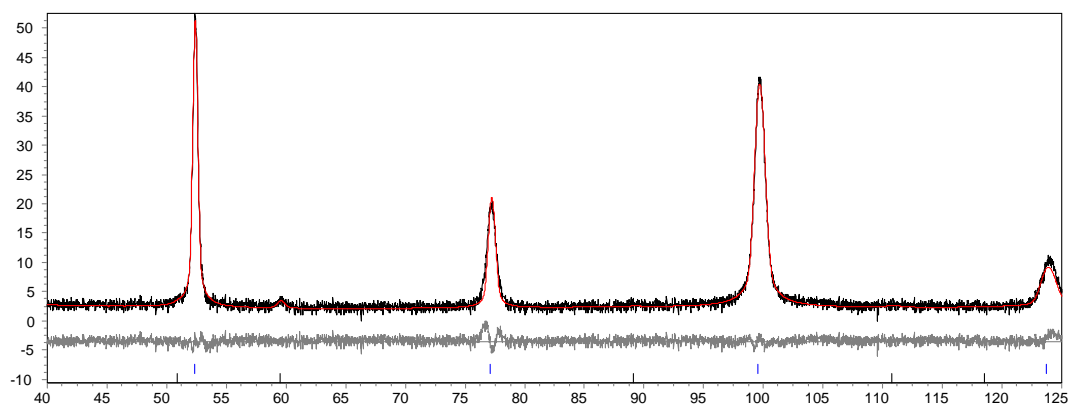Figure A-44 - XRD Rietveld refinement pattern for X100-2A at normalized position 0.

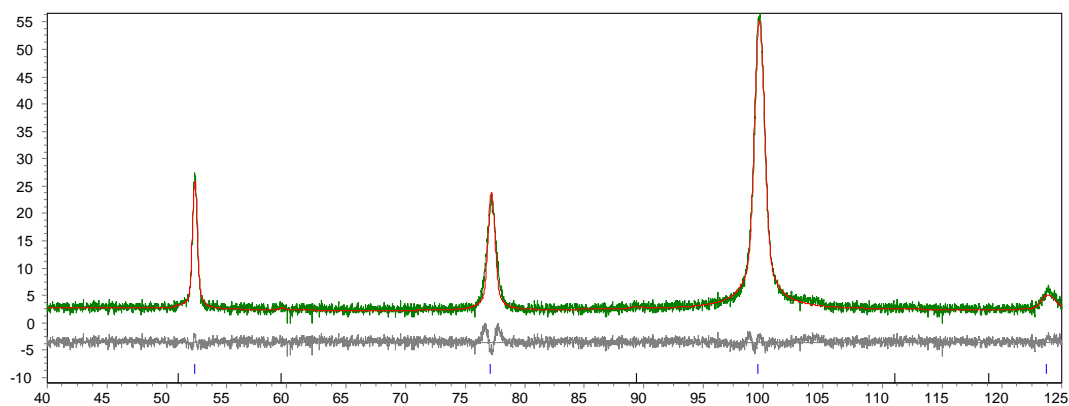Figure A-45 - XRD Rietveld refinement pattern for X100-2A at normalized position 3/10.

Figure A-46 - XRD Rietveld refinement pattern for X100-2A at normalized position 5/10.
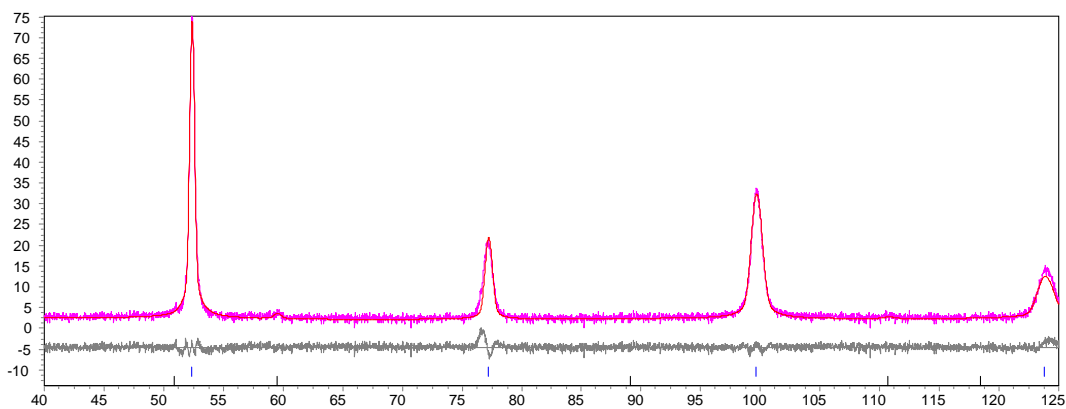
Figure A-47 - XRD Rietveld refinement pattern for X100-2A at normalized position 7/10.
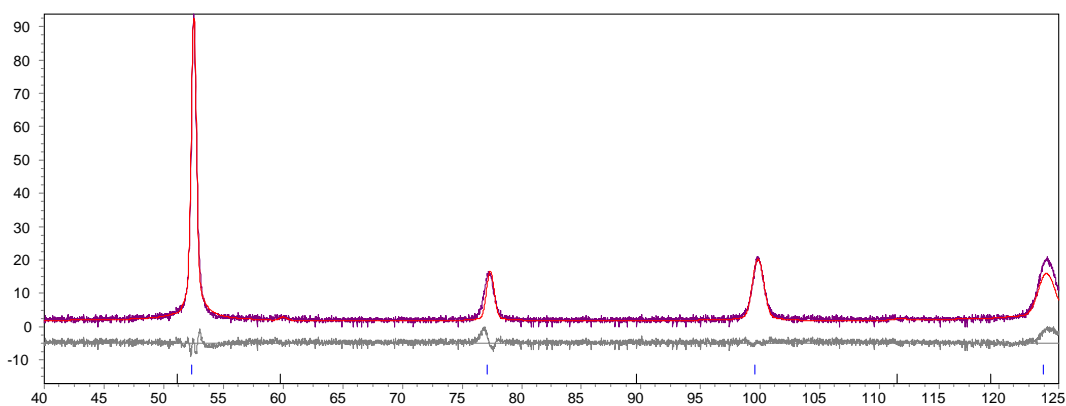

Figure A-48 - XRD Rietveld refinement pattern for X100-2A at normalized position 1.

Table A-10 - Normalized intensities for XRD patterns for steel X100-2A through thickness

Normalized position	Normalized intensity			
	I(110)	I(200)	I(211)	I(220)
0	100	2.5	4.6	5.6
3/10	100	7.5	29.6	4.2
5/10	100	56.3	273.3	7.4
7/10	100	7.7	37.6	4.6
1	100	2.3	4.4	5.2

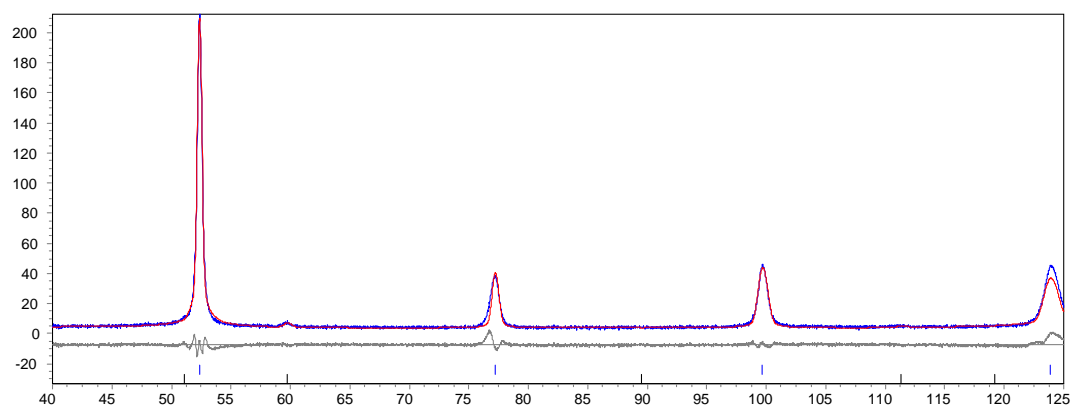**X100-2B steel Rietveld refinement patterns through thickness**

Figure A-49 - XRD Rietveld refinement pattern for X100-2B at normalized position 0.
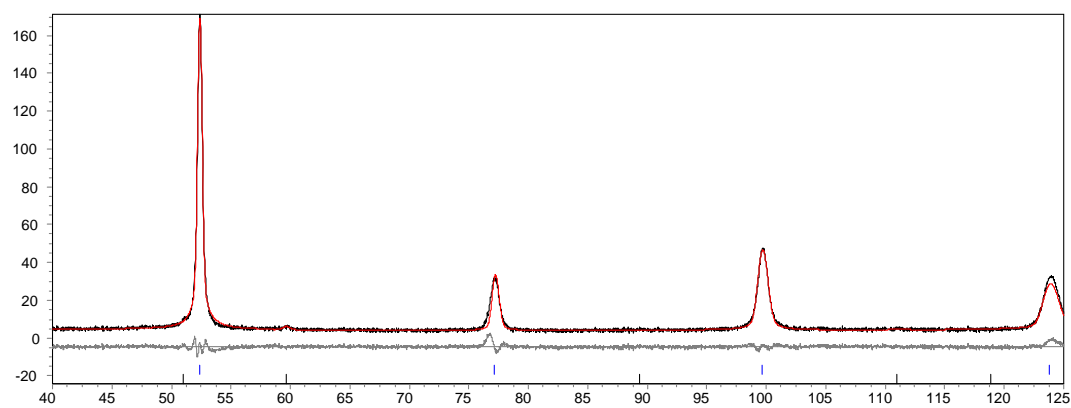

Figure A-50 - XRD Rietveld refinement pattern for X100-2B at normalized position 3/10.

Figure A-51 - XRD Rietveld refinement pattern for X100-2B at normalized position 5/10.

Figure A-52 - XRD Rietveld refinement pattern for X100-2B at normalized position 7/10.

Figure A-53 - XRD Rietveld refinement pattern for X100-2B at normalized position 1.

Table A-11 - Normalized intensities for XRD patterns for steel X100-2B through thickness

Normalized position	Normalized intensity			
	I(110)	I(200)	I(211)	I(220)
0	100	6.5	13.4	4.0
3/10	100	15.2	62.9	4.6
5/10	100	71.3	417.3	7.8
7/10	100	7.9	20.4	4.2
1	100	3.3	5.0	5.2

X100-3C steel Rietveld refinement patterns through thickness

Figure A-54- XRD Rietveld refinement pattern for X100-3C at normalized position 0.

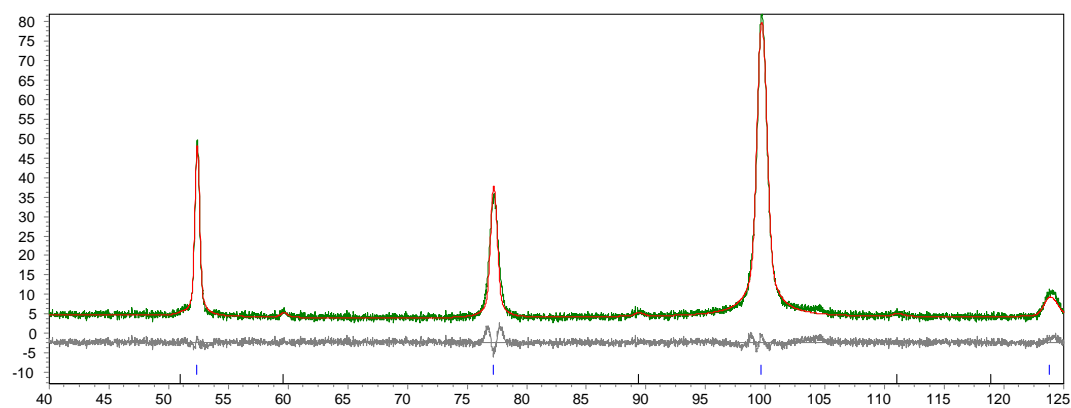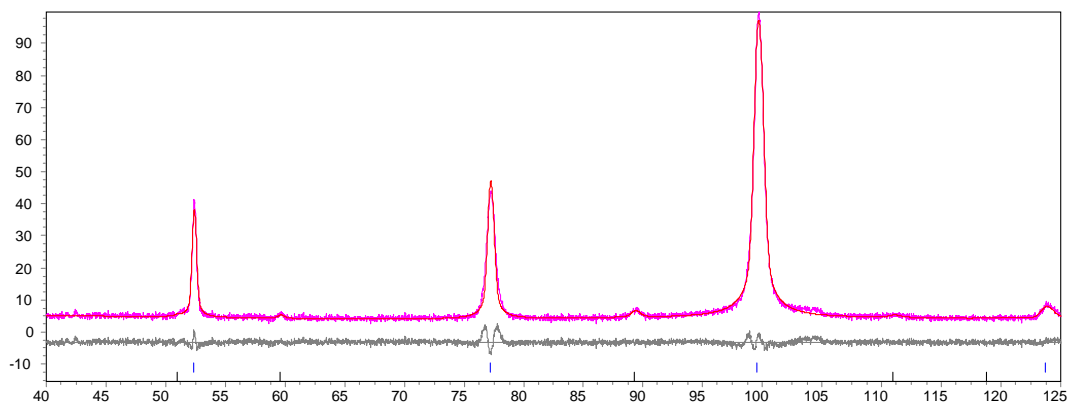Figure A-55 - XRD Rietveld refinement pattern for X100-3C at normalized position 3/10.

Figure A-56 - XRD Rietveld refinement pattern for X100-3Cat normalized position 5/10.

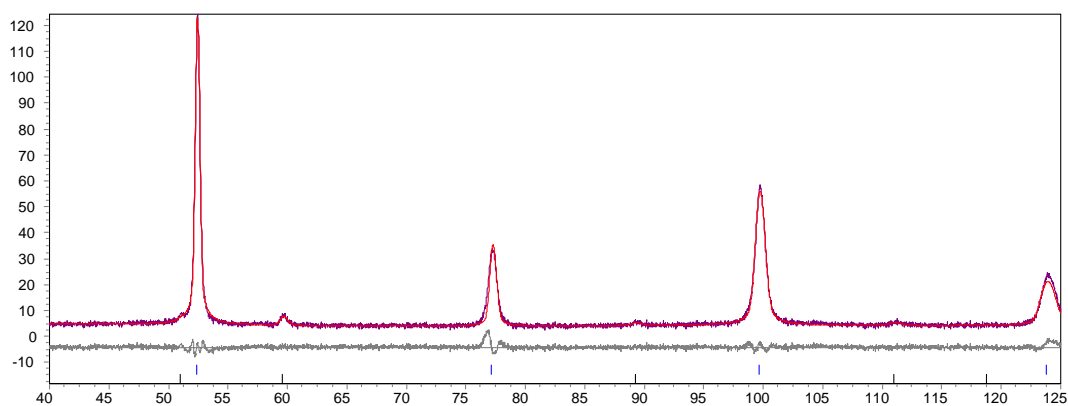Figure A-57 - XRD Rietveld refinement pattern for X100-3C at normalized position 7/10.

Figure A-58 - XRD Rietveld refinement pattern for X100-3C at normalized position 1.

Table A-12 - Normalized intensities for XRD patterns for steel X100-3C through thickness

Normalized position	Normalized intensity			
	I(110)	I(200)	I(211)	I(220)
0	100	3.4	4.8	4.6
3/10	100	3.5	7.7	3.7
5/10	100	52.3	271.6	5.2
7/10	100	114.3	591.3	5.5
1	100	7.3	22.0	3.9

Rietveld method raw outputs

Table A-13 – Direct outputs of Rietveld method for steel X80-462 through thickness

Normalized position	Domain size (nm)	Microstrain (%)	Spherical harmonics		Retained austenite (%)
			C41	C61	
0	303	7.1	0.33184	-0.74615	-
1/10	404	5.9	0.04641	-0.65949	-
5/10	388	4.9	-0.055251	0.83538	-
7/10	248	6.0	-0.50516	0.9193	-
1	135	5.9	-0.24867	0.70441	-

Table A-14 – Direct outputs of Rietveld method for steel X80-A4B through thickness

Normalized position	Domain size (nm)	Microstrain (%)	Spherical harmonics		Retained austenite (%)
			C41	C61	
0	224	6.9	-0.07479	-1.07257	-
3/10	330	7.5	-0.17616	-0.87578	0.23
5/10	246	7.8	-0.90313	1.187495	2.37
8/10	102	7.3	-0.80989	0.944063	1.32
1	99	7.6	-0.1933	-1.24578	0.42

Table A-15 – Direct outputs of Rietveld method for steel X80-A4F through thickness

Normalized position	Domain size (nm)	Microstrain (%)	Spherical harmonics		Retained austenite (%)
			C41	C61	
0	148	7.7	-0.16967	-0.27135	0.84
3/10	59	6.2	-1.03287	1.25229	6.15
5/10	150	7.0	-1.16754	1.35636	6.12
8/10	187	7.7	-0.29064	0.02469	1.02
1	139	6.5	-0.6493	-0.49209	0.20

Table A-16 – Direct outputs of Rietveld method for steel X80-B4F through thickness

Normalized position	Domain size (nm)	Microstrain (%)	Spherical harmonics		Retained austenite (%)
			C41	C61	
0	154	6.7	-0.31145	-0.1298	0.20
4/10	241	6.8	-1.04983	1.25304	7.05
5/10	223	8.3	-1.1578	1.34308	7.02
8/10	185	6.9	-0.8551	0.93473	2.10
1	202	6.7	-0.17035	-0.34079	0.20

Table A-17 – Direct outputs of Rietveld method for steel X100-2A through thickness

Normalized position	Domain size (nm)	Microstrain (%)	Spherical harmonics		Retained austenite (%)
			C41	C61	
0	68	11.4	0.09734	-1.25016	-
3/10	82	15.4	-0.82758	0.62909	-
5/10	39	12.3	-1.11133	1.29919	-
7/10	99	15.3	-0.92303	0.73431	-
1	81	12.6	0.15792	-1.22413	-

Table A-18 – Direct outputs of Rietveld method for steel X100-2B through thickness

Normalized position	Domain size (nm)	Microstrain (%)	Spherical harmonics		Retained austenite (%)
			C41	C61	
0	95	13.6	-0.21978	-0.10316	-
3/10	52	12.8	-0.92564	0.96181	-
5/10	50	11.7	-1.30003	1.38885	-
7/10	87	14.8	-0.37185	0.28168	-
1	68	15.0	0.22732	-1.04745	-

Table A-19 – Direct outputs of Rietveld method for steel X100-3C through thickness

Normalized position	Domain size (nm)	Microstrain (%)	Spherical harmonics		Retained austenite (%)
			C41	C61	
0	75	0	0.277535	-0.94119	0.2
3/10	153	3/10	-0.16893	-0.36777	0.2
5/10	68	5/10	-1.25509	1.357713	0.2
7/10	91	7/10	-1.24636	1.400188	1.77
1	94	1	-0.60353	0.486315	0.6

APPENDIX B - GRAIN MORPHOLOGY

X80-A4B
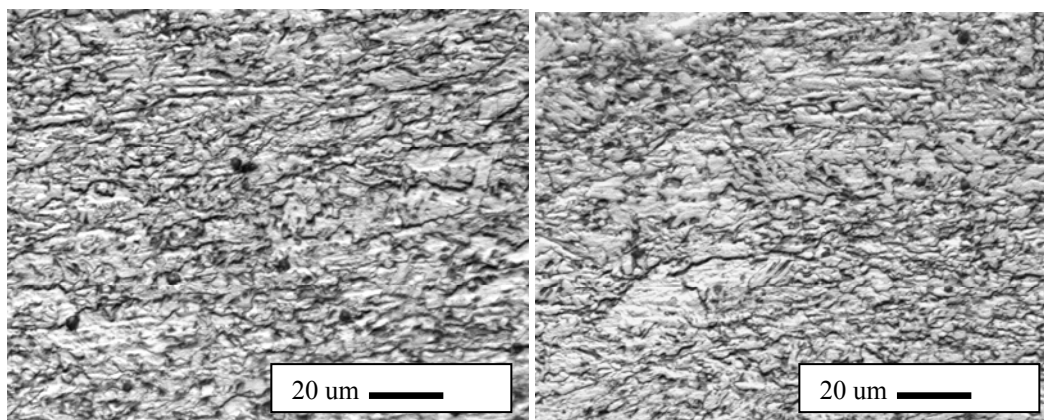
(A)

(B)
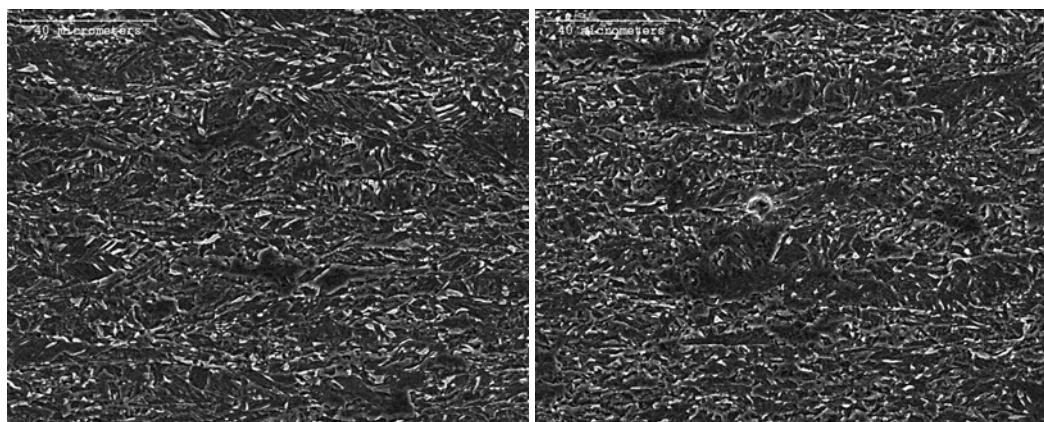
(C)

(D)

Figure B- 1 – Morphology for X80-A4B steel along rolling direction.
(A) OM image near pipe surface.   (B) OM image near center of strip.
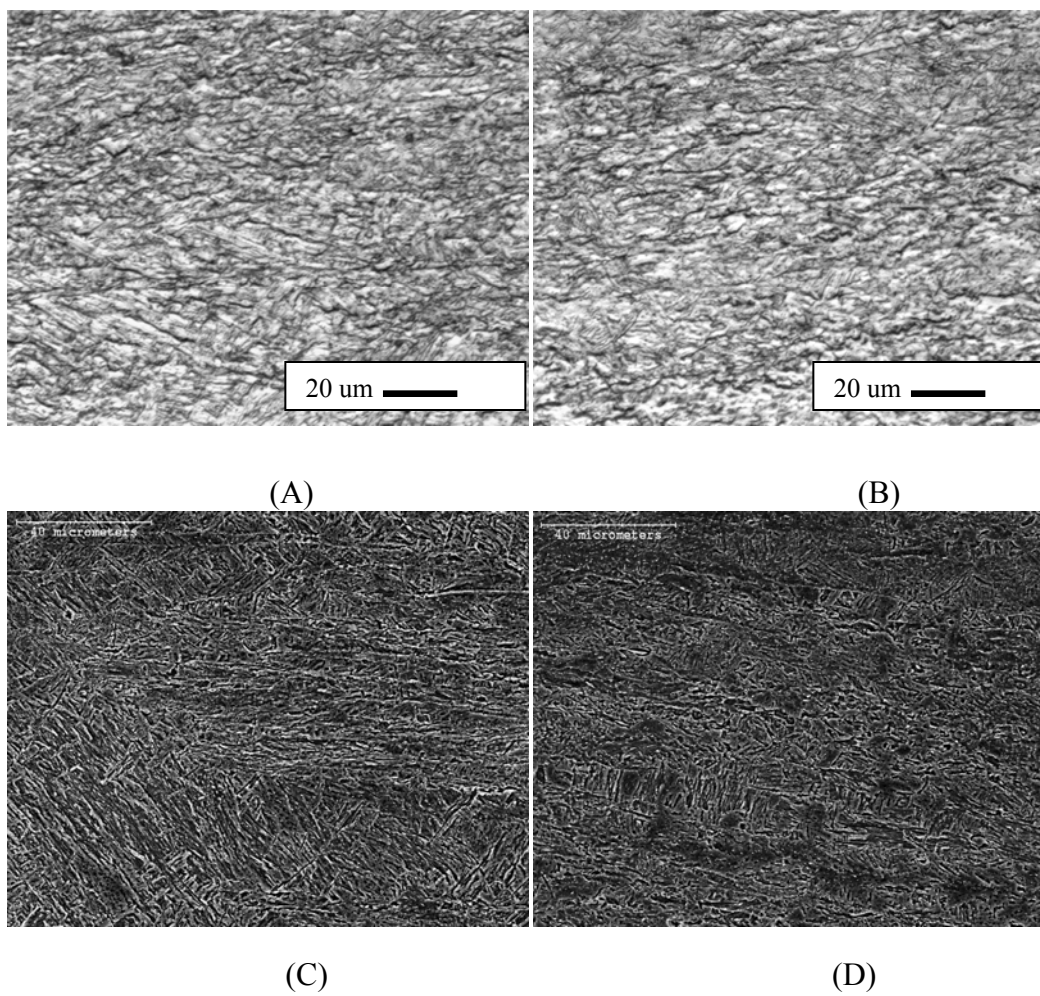(C) SEM image near pipe surface.   (D) SEM image near center of strip.

X80-A4F

(A)   (B)

(C)   (D)
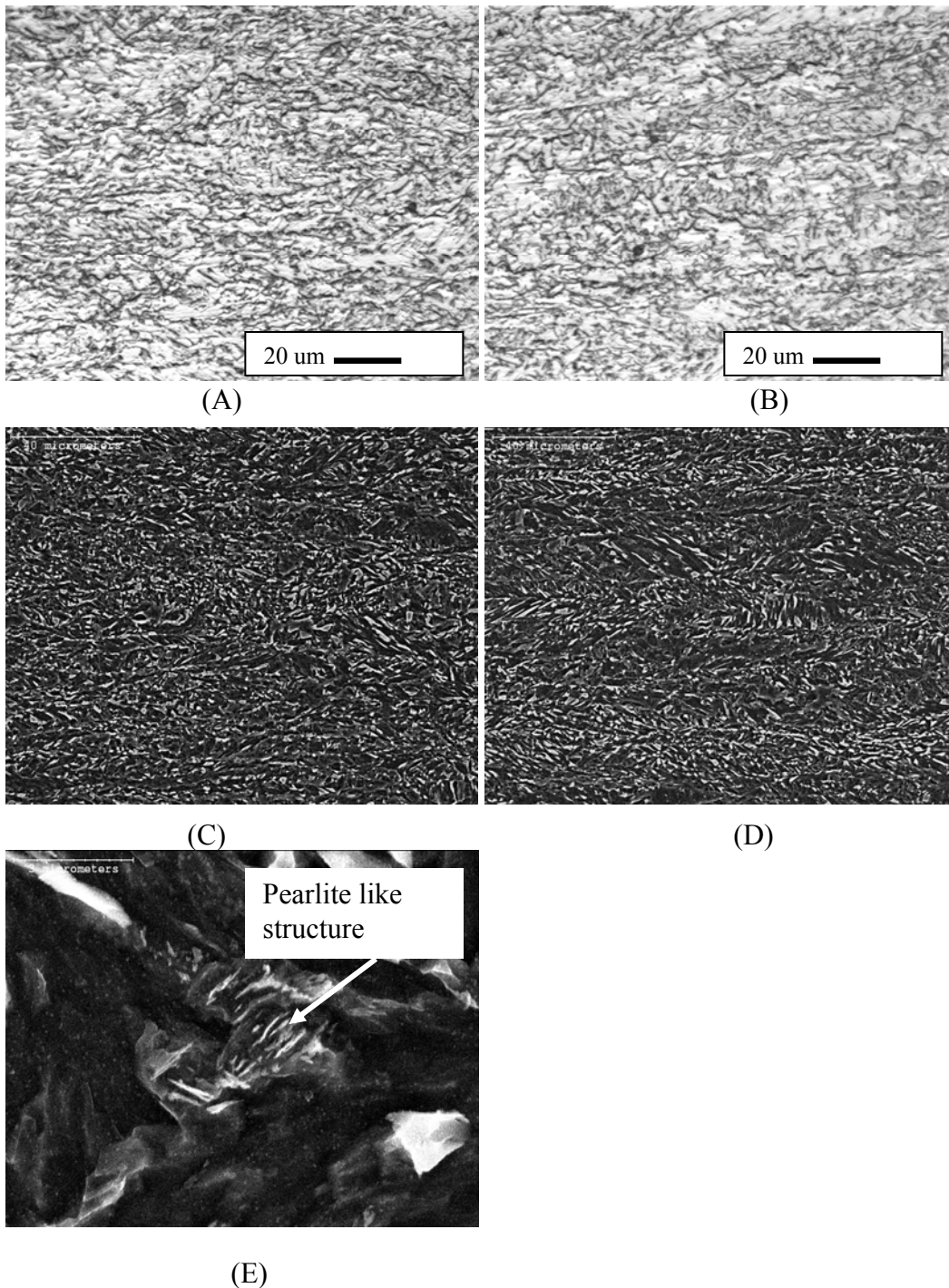
(E)

Figure B- 2 - Morphology for X80-A4F steel along rolling direction.
(A) OM image near pipe surface.   (B) OM image near center of strip.
(C) SEM image near pipe surface.   (D) SEM image near center of strip.
(E) Pearlite microstructure.

X80-B4F

(A)

(B)

(C)

(D)

Pearlite like
structure
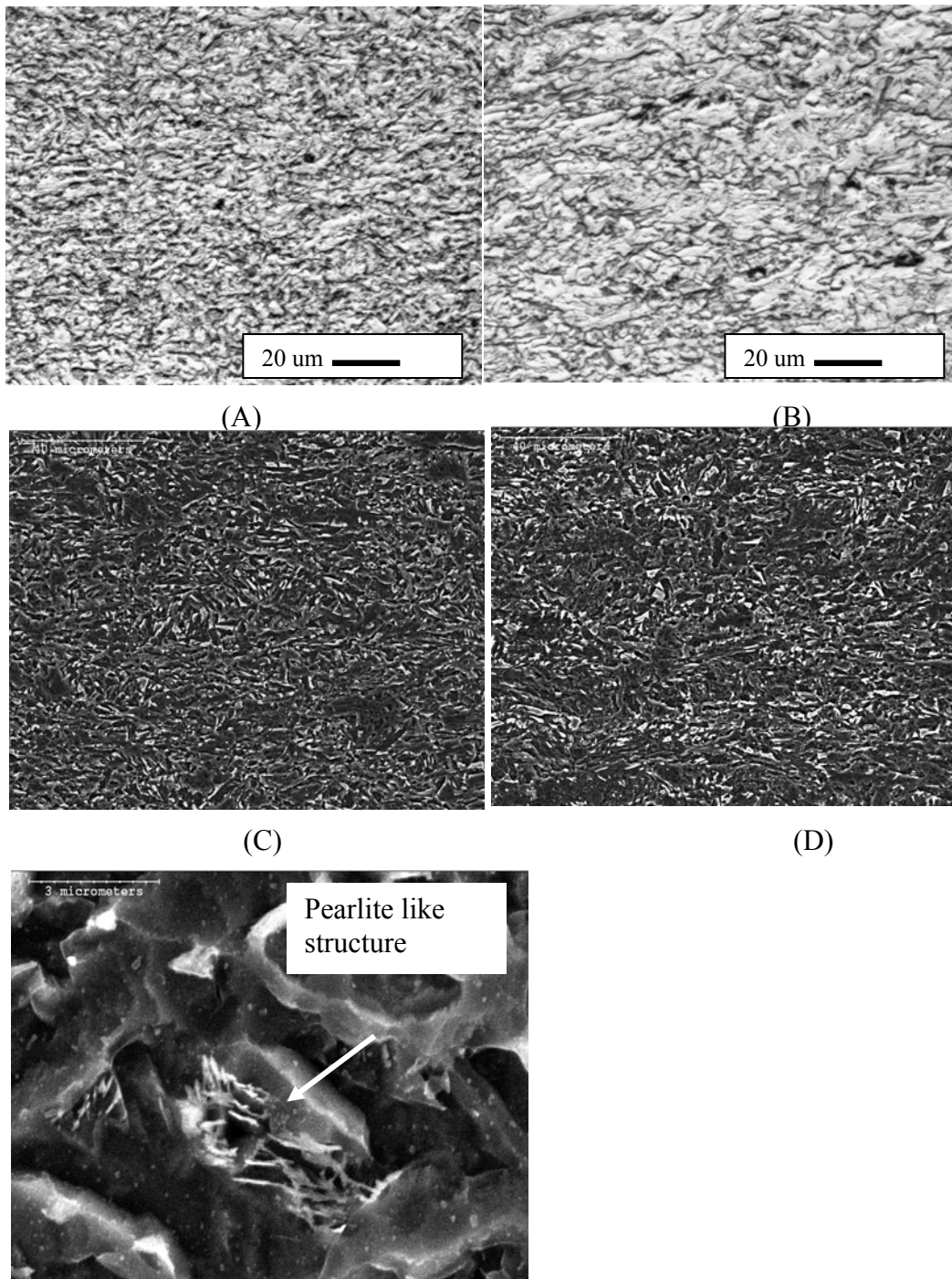
Figure B- 3 - Morphology for X80-B4F steel along rolling direction.
(A) OM image near pipe surface.   (B) OM image near center of strip.
(C) SEM image near pipe surface.   (D) SEM image near center of strip.
(E) Pearlite microstructure.

X100-2A
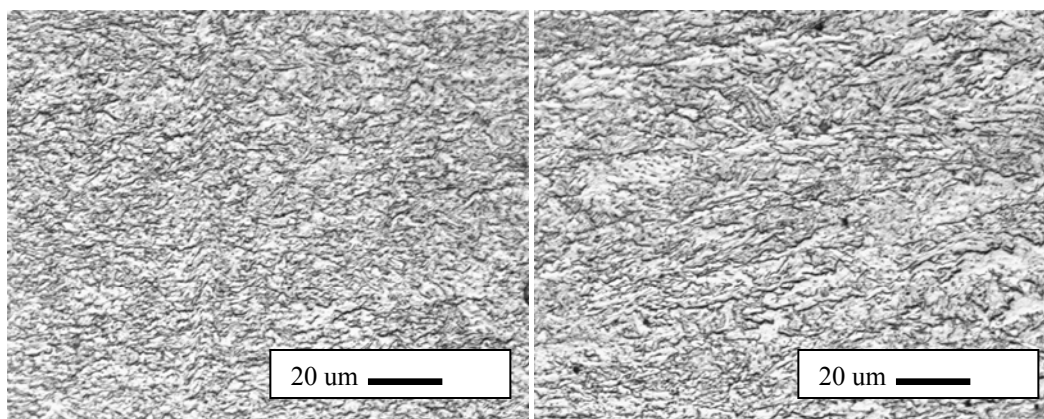
(A)   (B)
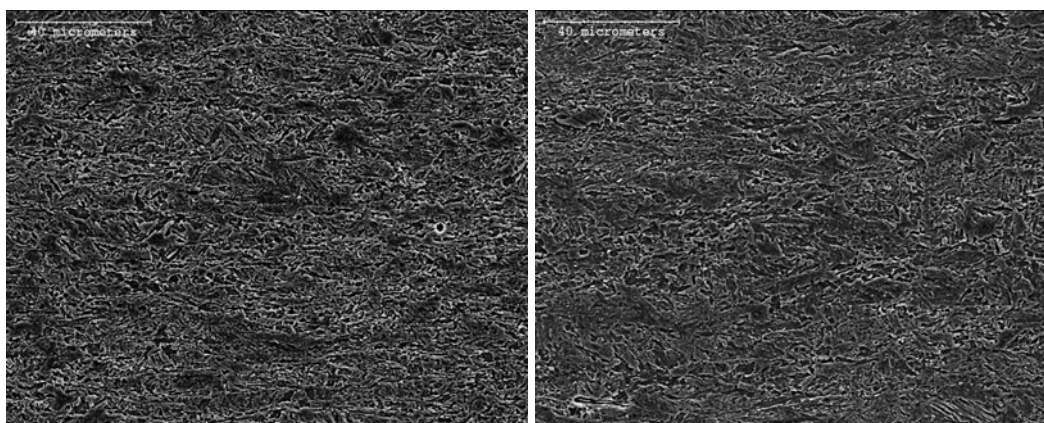
(C)   (D)

Figure B- 4 - Morphology for X100-2A steel along rolling direction.
(A) OM image near pipe surface.   (B) OM image near center of strip.
(C) SEM image near pipe surface.   (D) SEM image near center of strip.

X100-3C

(A)

(B)

(C)

(D)

Figure B- 5 - Morphology for X100-3C steel along rolling direction.
(A) OM image near pipe surface.   (B) OM image near center of strip.
(C) SEM image near pipe surface.   (D) SEM image near center of strip.
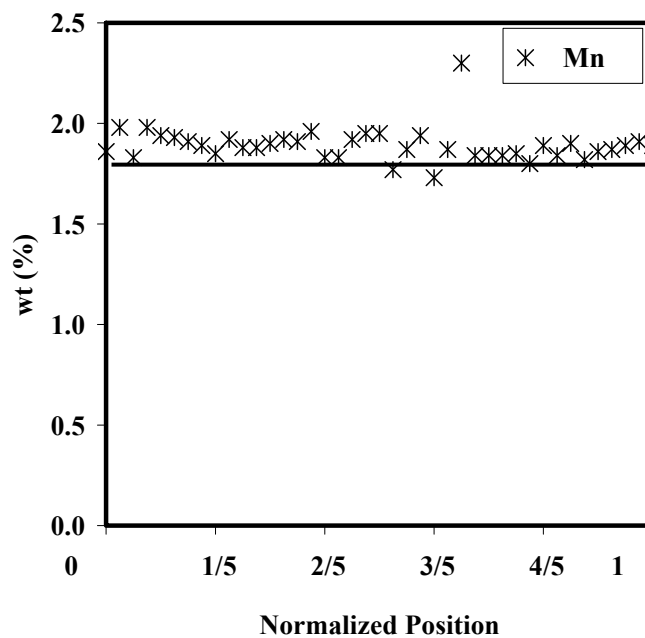
APPENDIX C - WDS ANALYSIS

X80-A4B
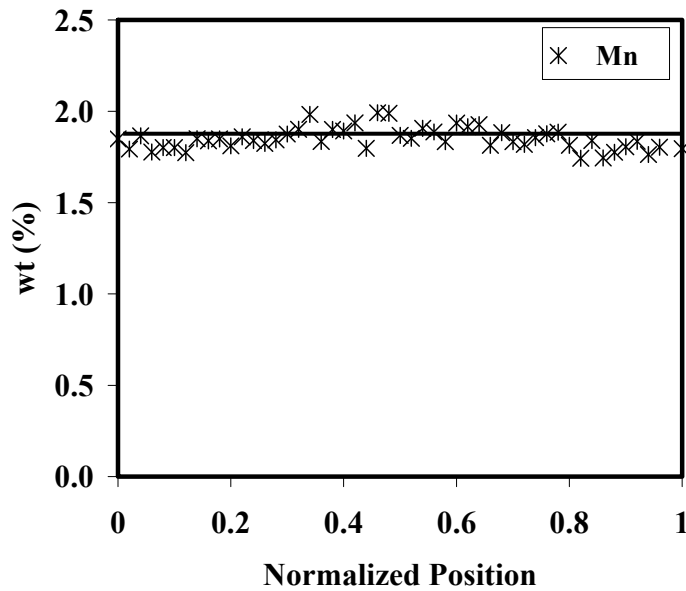
Figure C- 1 - WDS analysis for X80-A4B showing Mn wt% change through the pipe thickness. The solid line corresponds to the nominal concentration provided by Evraz Inc. NA.
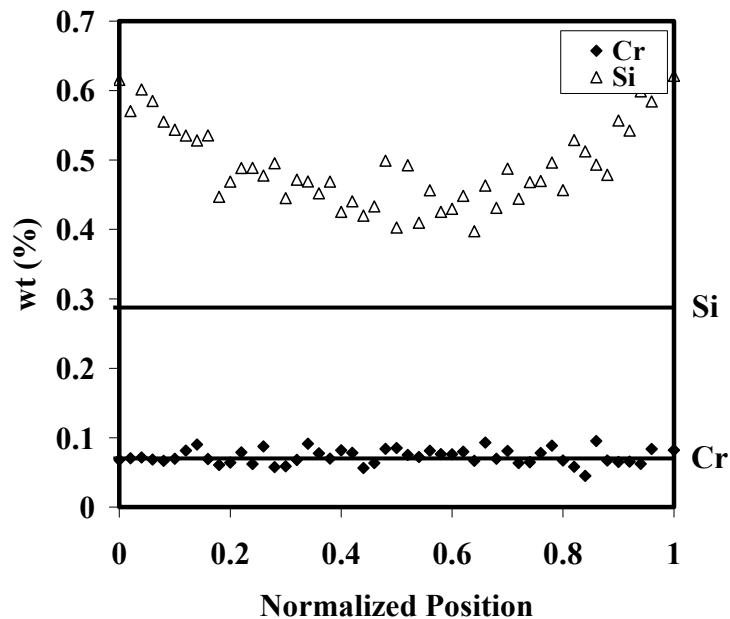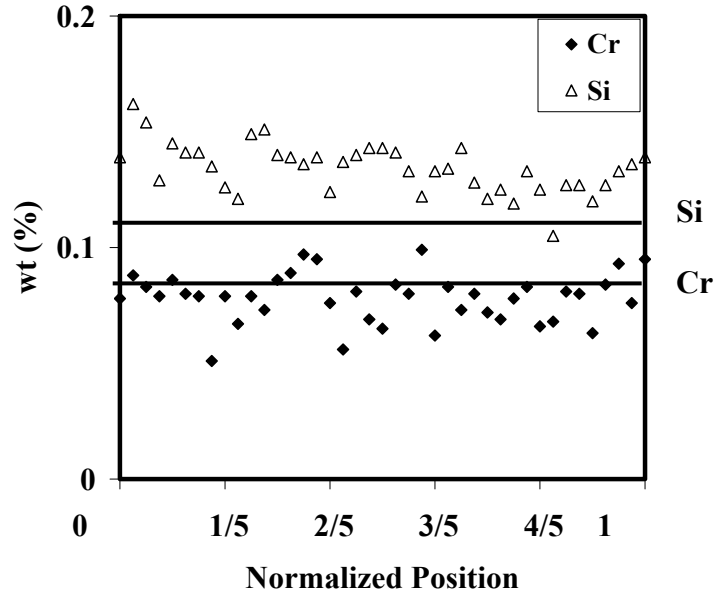

Figure C- 2 - WDS analysis for X80-A4B showing Cr wt% and Si wt% change through the pipe thickness. The solid line corresponds to the nominal concentration provided by Evraz Inc. NA.
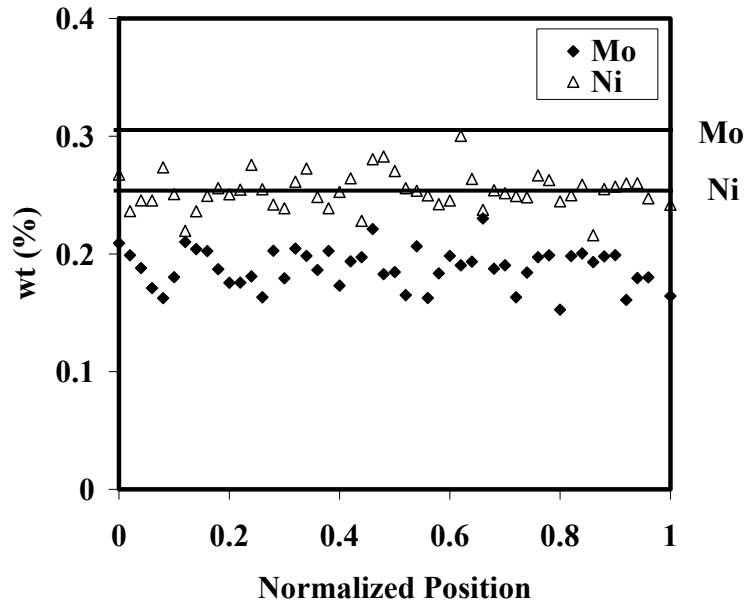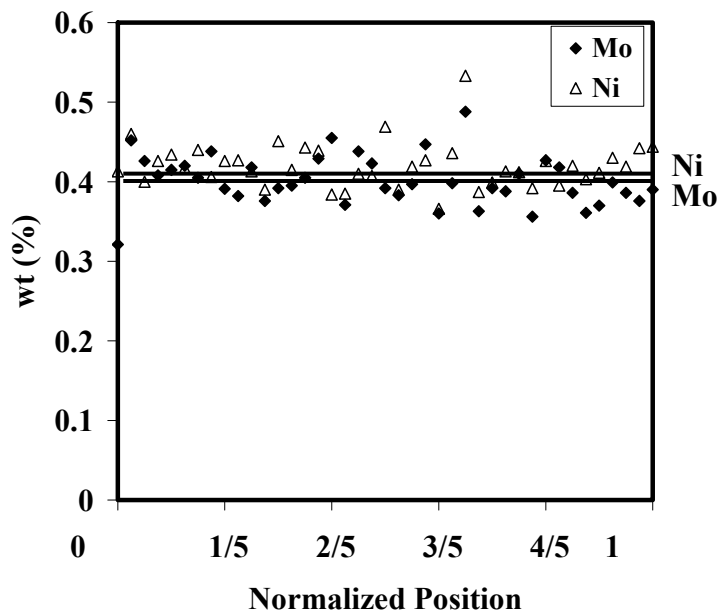
Figure C- 3 - WDS analysis for X80-A4B showing Mo wt% and Ni wt% change through the pipe thickness. The solid line corresponds to the nominal concentration provided by Evraz Inc. NA.
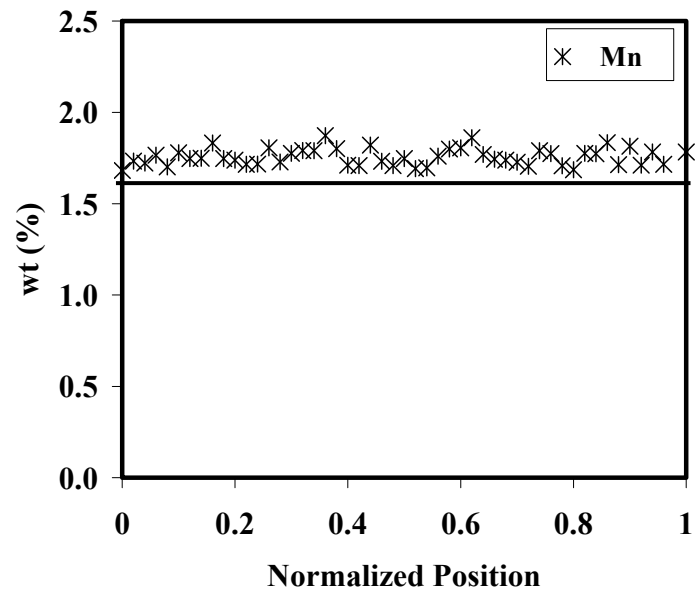
X80-A4F

Figure C- 4 - WDS analysis for X80-A4F showing Mn wt% change through the pipe thickness. The solid line corresponds to the nominal concentration provided by Evraz Inc. NA.
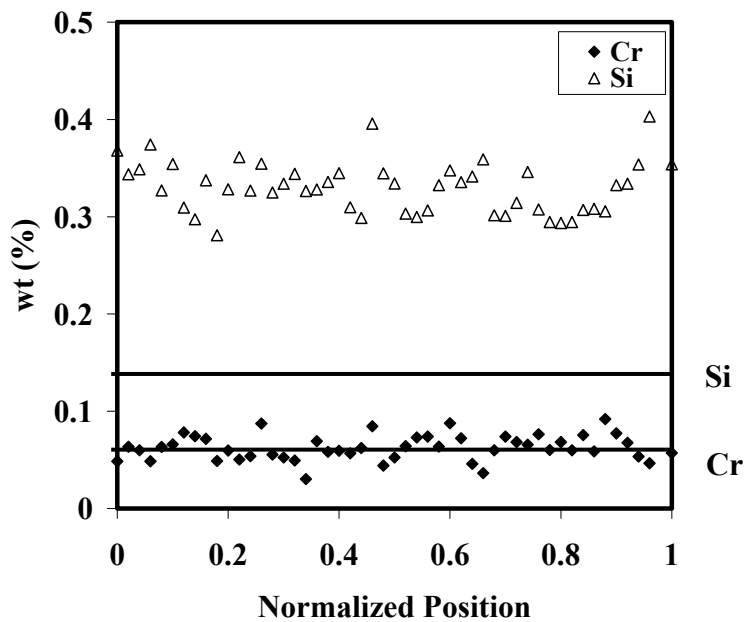
Figure C- 5 - WDS analysis for X80-A4F showing Cr wt% and Si wt% change through the pipe thickness. The solid line corresponds to the nominal concentration provided by Evraz Inc. NA.
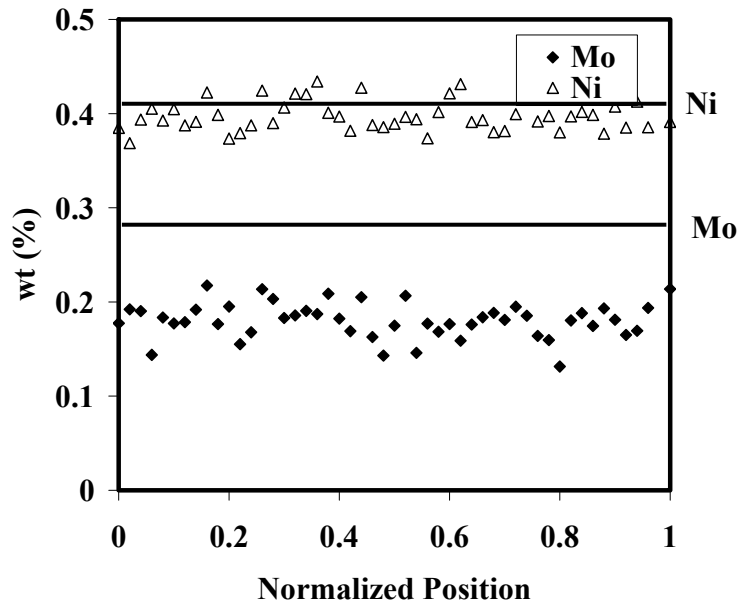

Figure C- 6 - WDS analysis for X80-A4F showing Mo wt% and Ni wt% change through the pipe thickness. The solid line corresponds to the nominal concentration provided by Evraz Inc. NA.

X80-B4F

Figure C- 7 - WDS analysis for X80-B4F showing Mn wt% change through the pipe thickness. The solid line corresponds to the nominal concentration provided by Evraz Inc. NA.

Figure C- 8 - WDS analysis for X80-B4F showing Cr wt% and Si wt% change through the pipe thickness. The solid line corresponds to the nominal concentration provided by Evraz Inc. NA.

Figure C- 9 - WDS analysis for X80-B4F showing Mo wt% and Ni wt% change through the pipe thickness. The solid line corresponds to the nominal concentration provided by Evraz Inc. NA.
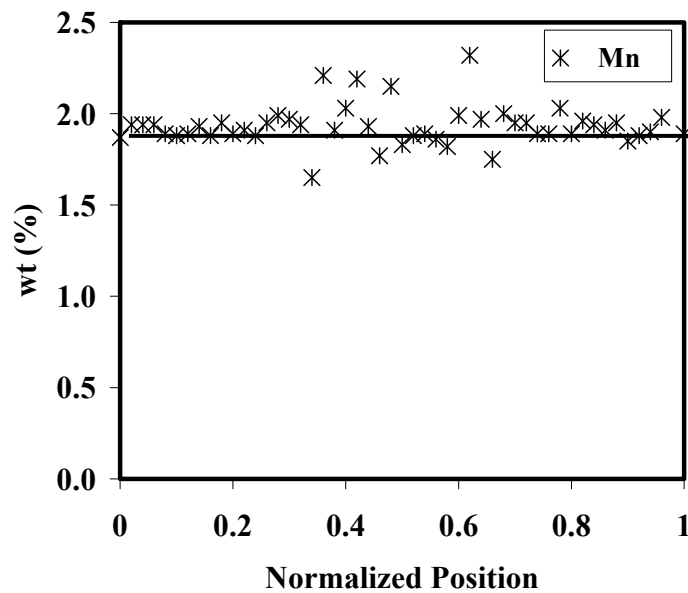
X100-2A

Figure C- 10 - WDS analysis for X100-2A showing Mn wt% change through the pipe thickness. The solid line corresponds to the nominal concentration provided by Evraz Inc. NA.
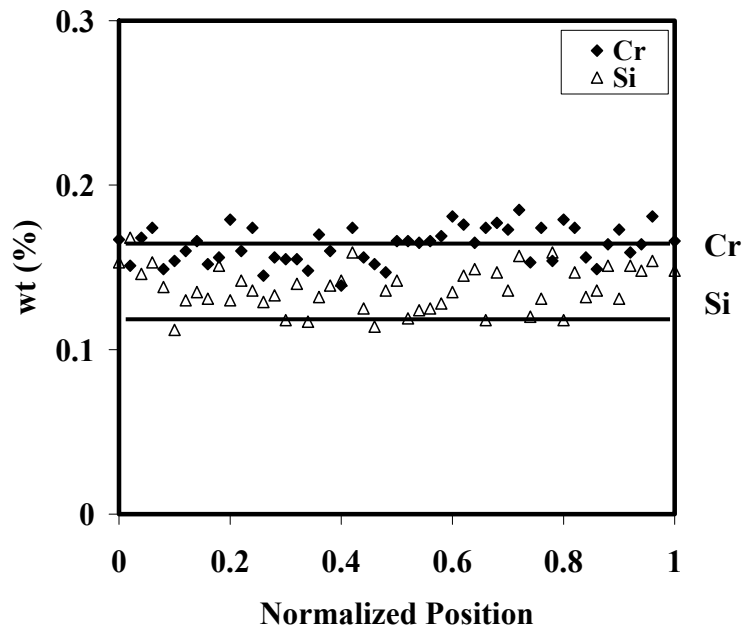
Figure C- 11 - WDS analysis for X100-2A showing Cr wt% and Si wt% change through the pipe thickness. The solid line corresponds to the nominal concentration provided by Evraz Inc. NA.
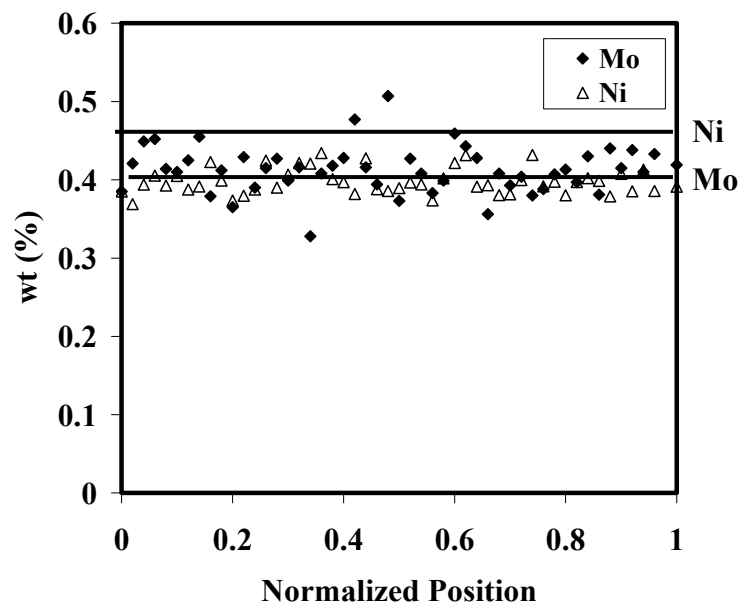

Figure C- 12 - WDS analysis for X100-2A showing Mo wt% and Ni wt% change through the pipe thickness. The solid line corresponds to the nominal concentration provided by Evraz Inc. NA.